Epithelial flow by controlled transformation of internal force-balance geometry

Fridtjof Brauns*[1], Nikolas H. Claussen*[2], Eric F. Wieschaus[3], and Boris I. Shraiman[1,2]

[1] *Kavli Institute for Theoretical Physics, University of California Santa Barbara, Santa Barbara, California 93106, USA*
[2] *Department of Physics, University of California Santa Barbara, Santa Barbara, California 93106, USA*
[3] *Department of Molecular Biology, Princeton University, Princeton, NJ, USA; The Lewis-Sigler Institute for Integrative Genomics, Princeton University, Princeton, NJ, USA*

Highlights

- Tissue flow is explained by controlled transformation of cortical tension balance
- Positive tension feedback drives active cell intercalation
- Coordination of cell intercalation requires order in local tension configurations
- Tension dynamics model predicts total tissue shape change from initial cellular order

Summary

Shape changes of epithelia during animal development, such as convergent extension, are achieved through concerted mechanical activity of individual cells. While much is known about the corresponding large scale tissue flow and its genetic drivers, the question of cell-scale coordination remains open. We propose that this coordination can be understood in terms of mechanical interactions and instantaneous force balance within the tissue. Using whole embryo imaging data for *Drosophila* gastrulation, we exploit the relation between balance of local cortical tension forces and cell geometry. This unveils how local positive feedback on active tension and passive global deformations account for coordinated cell rearrangements. We develop a model that bridges the cell and tissue scale dynamics and predicts the dependence of total tissue extension on initial anisotropy and hexagonal order of the cell packing. Our study provides general insight into the encoding of global tissue shape in local cell-scale activity.

Keywords: tissue mechanics, drosophila embryo, convergent–extension, cell intercalation, active solid

*FB and NC contributed equally to this work.

Introduction

Tissue elongation is one of the basic elements of morphogenesis. Tissues can elongate by oriented cell divisions and growth [1, 2], or via local rearrangements of cells. The latter happens during "convergent–extension" – a common motif of early development and organogenesis in many organisms [3–5] – where tissue elongates along one axis while contracting along the perpendicular direction [6]. Convergent extension also exemplifies the important role of cell and tissue mechanics in morphogenetic processes, which must be studied alongside developmental genetics and signaling. Mechanics is what directly determines physical shape, and also plays a key regulatory role further upstream by facilitating mechanical pattern formation [7], in diverse systems such as feather primordia [8] and the amniote primitive streak [9]. Convergent extension is often conceptualized on the continuum scale, where the morphogenetic process resembles a shear flow [10, 11]. The key challenge is to relate large scale flow of tissue to its behavior on the scale of cells, where the active local forces that drive the flow are generated and controlled.

Viewed on the cell scale, tissue flow involves remodelling of cell-cell interfaces which enables intercalation of cells. Without intercalation, large deformation of tissue shape in the absence of proliferation would entail equally large deformation of cell shape: intercalations allow a tissue to deform like fluid. Yet unlike hydrodynamic flows which are driven by external forces, convergent–extension is driven from within by active stresses generated by molecular motors, such as myosin. Given the spatial distribution of myosin across the embryo, one can compute the instantaneous tissue flow using a continuum active fluid model, as was demonstrated for *Drosophila* body axis elongation (germ band extension, GBE) [11]. However, while successfully describing the instantaneous flow, this continuum model [11] cannot predict the flow in the next moment of time. To predict forward in time one needs to understand the regulation of active tension, which unfolds on the scale of cells.

Intercellular adhesion effectively links the cytoskeletons of neighboring cells, making a two dimensional epithelial sheet a transcellular mechanical network put under tension by myosin motors. This internal tension is revealed by laser ablation of cell interfaces, which causes rapid recoil [12]. The capacity of epithelial tissue to support tension makes it markedly different from passive fluids [13]. How does one reconcile the solid-like capacity of an epithelial monolayer to support tension (as well as shear stress) with its ability to change shape and rearrange internally rather like a fluid? Answering this question will be key to construct a predictive model of tissue flow that bridges the cell and tissue scales.

One of the best-established models of morphogenetic mechanics is provided by the *Drosophila* embryo, which is ideal for live imaging and offers an extensive set of genetic tools [14]. Progress in live imaging and computational image analysis has produced remarkably quantitative data [15, 16]. In this work, we will take advantage of existing data [16] which we will reanalyze and use as test-bed for theory development. Figure 1 recapitulates the basic quantitative features of the GBE in the *Drosophila* embryo based on the light-sheet imaging data from [16] which, thanks to computational image processing (surface extraction, cell segmentation and tracking), provides a global picture of tissue dynamics with cellular resolution. During gastrulation of *Drosophila*, the embryonic blastoderm (an epithelial monolayer of about 6000 cells on the surface of the embryo) undergoes dramatic deformation that changes tissue topology and gives rise to the three germ layers [17]. Gastrulation starts (see Fig. 1A) with the formation of the Ventral Furrow (VF) which initiates the internalization of mesoderm, followed immediately by Germ Band Extension (GBE), which involves convergent extension of the lateral ectoderm and the flow of tissue from the ventral onto the dorsal side of the embryo [18–20] (see Movie 1). GBE has been extensively studied, leading to the identification of relevant developmental patterning genes [18–21]. Live imaging has also uncovered the pertinent cell behavior, namely intercalation of neighboring cells in the lateral ectoderm [22, 23]. The elementary process of cell rearrangement is called a T1 transition. It involves

a quartet of cells where two cells lose contact and the two other cells gain contact (see Fig. 1B, bottom). The role of intercalations becomes visible through "tissue tectonics" [24] analysis, which decomposes the tissue strain rate into cell-level contributions, distinguishing between cell-shape deformation and cell rearrangement (see Fig. 1B and Fig. S1). During VF invagination, cells in the lateral ectoderm are stretched along the DV axis with little rearrangement (Fig. S1A) Subsequently, during GBE, the lateral ectoderm (i.e. the germ band) extends (Fig. 1D) by cell rearrangements with very little cell elongation (Fig. 1C, bottom; and Fig. S1B and D). By contrast, the dorsal tissue (amnioserosa) deforms in the opposite direction as the germ band, by a combination of cell shape changes and rearrangements (Fig. 1C, top; and Fig. S1C). Overall, we find that the majority of cell rearrangements happen via T1s (Fig. 1E and E') with only a small number of "rosettes" (which involve more than 4-cells transiently sharing a vertex) being formed. This is consistent with the high degree of spatial coordination of rearrangements that is apparent in the lateral ectoderm (Fig. 1C, bottom).

Intercalations are associated with localized activity of the force generating protein non-muscle myosin II [20–22] (henceforth, "myosin"). Myosin recruitment depends on the expression of key developmental genes [19–21, 25], and, in addition, is subject to positive and negative mechanical feedback that depends on the stress [26, 27] and the rate of strain (rate of cell deformation) [28]. Despite considerable understanding of the genetic and cell-biological components involved in GBE, the relative role of the genetic pre-pattern versus mechanical feedback-driven "self-organization" of myosin activity is still not understood. Similarly, despite rich experimental data and great biological interest, no consensus has emerged regarding the cell-level mechanics of GBE [24, 26, 29–31]. Key questions remain open: How is myosin dynamics controlled on a cellular level? How are intercalations are driven mechanically [29, 32]? How is active force generation orchestrated across cells to create a coherent global morphogenetic flow? What sets the total amount of tissue elongation? These questions call for a coherent theoretical framework that allows interpreting and reconciling existing experimental findings.

The rich dataset shown in Fig. 1 exposes a wealth of information about the mechanical behavior of cells and thus allows us to address these problems. Our approach is based on the assumptions that (i) stresses are concentrated in the actomyosin cortices along cell-cell interfaces, forming a trans-cellular cytoskeletal mechanical network that (ii) maintains adiabatic force balance. We refer to the the adherens junction actomyosin cortex, located parallel to the interface of two neighboring epithelial cells [34], as the "cortex", and the tension therein as "cortical tension". This cortical force balance provides a direct link between mechanics and geometry. It allows inference of tensions from the angles at tri-cellular vertices [35–37], which we utilize to identify from data the stereotyped local geometry and tension profile associated with actively and passively driven T1 transitions. We will show that active and passive T1 transitions are distinguishable on a purely geometric basis: the former involve deformations that change local angles, while the latter involve angle preserving ("isogonal") deformations. We shall argue that active T1s can be understood in terms of positive feedback that regulates cortical tensions and thus remodels internal force-balance geometry. In contrast, passive T1s are driven by external stresses. Our analysis will then address the question of mechanical coordination of cellular behavior and the patterning of tissue flow on the scale of the embryo. We will show that coordination of T1 events among neighboring cells involves a characteristic pattern of the tensions on the interfaces which meet at a vertex, which we quantify via a "Local Tension Configuration" (LTC) parameter. Lastly, we shall use these insight to formulate a model of GBE where active T1 processes are driven by positive feedback acting on tensions that are anisotropically biased already before gastrulation starts. In our "active solid" model, the trans-cellular network of cortical tensions remodels while remaining in force balance, and thereby generates epithelial "flow". The dynamics will be explained by positive feedback of cortical tensions, generating active T1s, as well as long-range isogonal

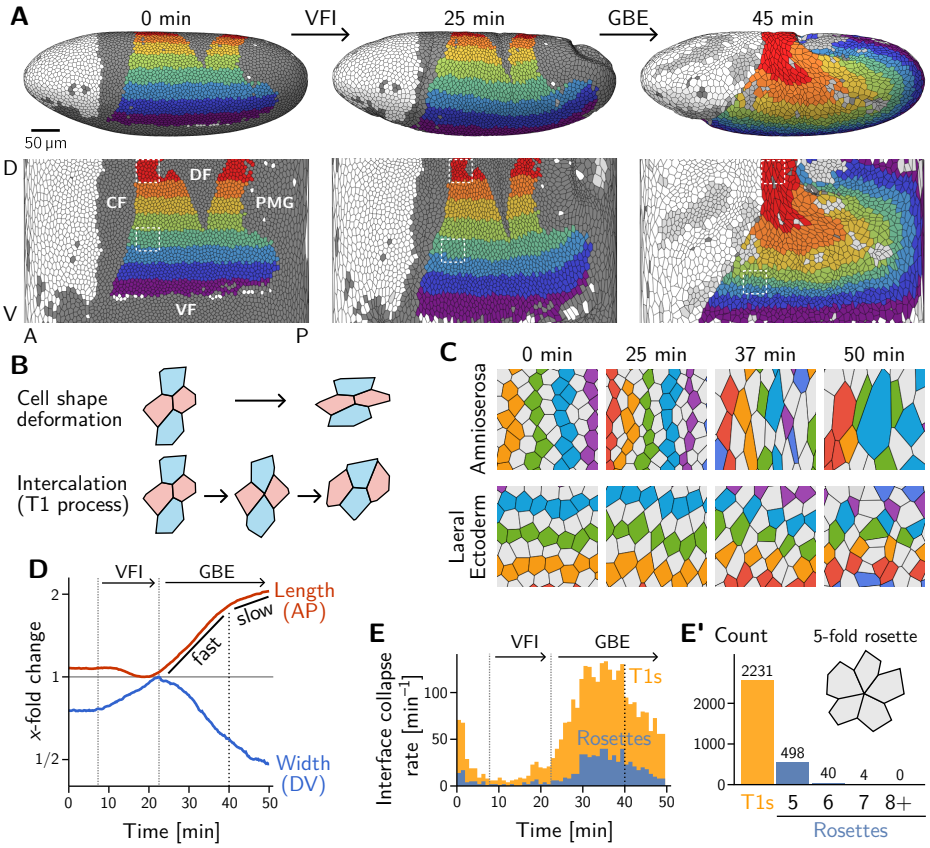

Figure 1: Light sheet imaging, segmentation, and tracking [16] provides a global picture of the cell level contributions to tissue flow ("tissue tectonics" [24]) during *Drosophila* gastrulation. A Segmented and tracked cells on the ellipsoidal surface of the early Drosophila embryo in 3D (top) and projected into the plane (bottom) using a cartographic projection [33]; imaging, segmentation and tracking data from Ref. [16]. Trunk cells are colored in bands along the DV axis to illustrate the major tissue deformations during early development of *Drosophila*: ventral furrow invagination (VFI, 25 min) and germ band extension (GBE, 45 min). The purple to green regions constitute the lateral ectoderm (germ band) which contracts along the DV axis and extends along the AP axis. The posterior part of the germ band moves over the pole as it extends. The red and orange regions constitute the amnioserosa, which contracts along the AP axis and extends along the DV axis. Cells that are internalized in folds are shaded in dark gray (CF: Cephalic furrow; DF: Dorsal folds; VF: Ventral furrow; PMG: posterior midgut). Only one side of the left-right symmetric embryo is shown but both sides were analyzed throughout the manuscript. **B** Tissue deformation is the sum of cell shape changes (top) and cell rearrangements (bottom). The elementary cell rearrangement is a T1 transition in a quartet of cells. The interface between the red cells collapses, giving rise to a transient four-fold vertex configuration (center). The four-fold vertex then resolves to form a new interface between the blue cells. **C** Colored, tracked cells illustrate the cell rearrangements and shape changes in the amnioserosa (top) and lateral ectoderm (bottom). While amnioserosa cells show large deformations and little coordination in their rearrangement, cell intercalations in the lateral ectoderm appear highly choreographed. (ROI size 40×40 µm^2.) **D** Convergence and extension of the lateral ectoderm (x-fold change defined relative to the minimum length and maximum width respectively). During VFI, the lateral ectoderm is stretched along DV axis and slightly contracts along the AP axis. GBE has an initial fast phase before slowing down at around 40 min. **E and E'** Rate of interface collapses serves as a measure for the cell intercalation rate. During VFI, the are few intercalations. During GBE, the majority of intercalations are T1 transitions, while rosettes, rearrangements involving more than four cells, contribute significantly less to tissue deformation (E'). At 40 min, there is a noticeable drop in the T1 rate, marking the transition to the slow phase of GBE. Intercalation events before $t = 12$ min where excluded from the subsequent analysis.

deformations that act to pattern the flow globally. Flow naturally slows to a creep as successive intercalations scramble LTC order and prevent coordinated T1s. Thus, initial order and anisotropy set the total amount and direction of tissue extension. This model bridges dynamics on the cellular and tissue scale and has the capacity to predict flow forward in time.

Results

Force balance and cell geometry in an epithelial monolayer

We begin by laying out the assumptions and concepts that underlie our framework. We argue that in contrast to regular fluid flow, where externally or internally generated forces are balanced by viscosity or substrate friction, tissue flow can be understood in terms of adiabatic remodelling of a quasistatic force balance network. This point of view is supported by the fact that epithelial tissues are under internally generated tension, which is revealed by recoil in response to laser ablation. Furthermore, the timescale of this recoil ($\sim 10\,\mathrm{s}$) on the scale of cells is at least 10-fold faster than the timescale of local tissue flow [38, 39]. This suggests that rapid force equilibration makes the apparent tissue flow approximately adiabatic (see also Refs. [37, 40]).

Second, we assume that mechanical stress in the epithelium is primarily carried by the adherens-junctional cytoskeleton, which resides on cell interfaces. This is supported by the observation that cell interfaces in the *Drosophila* blastoderm are mostly straight. Cells are attached to their neighbors via adherens junctions that are linked to the junctional cytoskeleton in each cell (Fig. 2A) [41]. The myosin motors exert a contractile force on the actin fibers and thereby keep the cortex under active tension (T), which we refer to as "cortical tension"[42]. Together, the adherens junctions define a tissue-wide mechanical structure, capable of (i) generating locally controlled internal tension and (ii) adaptively remodelling its architecture. The *Drosophila* blastoderm lies on top of a fluid yolk [43] which exerts negligible drag forces on tissue motion on the surface [40], suggesting that all forces are balanced within the epithelial layer.

Concentration of tension in interfaces tightly links force balance with the readily observable geometry of cell-cell interfaces. Force balance requires that the forces $\mathbf{T}_{ij}$ exerted by the cortical tensions sum to zero at each vertex where three (or more) interfaces meet. (Here, the indices i, j label the two cells that meet at a interface; see Fig. 2A.) In effect, these force-balance constraints relate the *relative* tension in cell interfaces at a vertex to the angles at which the interfaces meet [35]. This link of hard-to-observe cortical tensions to the readily observable local cell geometry enables tension inference methods which have been extensively validated by computational robustness checks [36], direct comparison with measured laser ablation recoils [44] and by correlation with local myosin abundance [37].

Crucially, the link between force balance and the geometry of the cell tessellation goes beyond inference and to the very basis of our proposed mechanism of tissue flow. Force balance implies that tension vectors meeting at a vertex form a triangle [13], as illustrated in Fig. 3B. The angles of the triangle are complementary to the corresponding angles at which the interfaces meet. (This becomes evident by rotating each triangle edge by 90°.) As adjacent vertices share an interface, the corresponding tension triangles share an edge: the tension triangles form a triangulation, i.e. fit together to form a plane surface. The triangulation is dual to the cell tessellation: For each cell, there is a corresponding vertex in the tension triangulation (Fig. 3B'). (Dual force tilings go back to Maxwell [45] and have been applied to the statics of beam assemblies [46] and granular materials [47].) This triangulation establishes a geometric structure in tension space. Force balance requires that the angles at vertices in the physical cell tessellation are complementary to those in the tension triangulation. This intimately links tension space and epithelial geometry in real space. Myosin-driven local changes in tension change the shapes of

tension-space triangles and hence modify the tension triangulation. The induced changes in the geometry of the cell tessellation drive both the local rearrangement of cells and the global tissue flow. The remainder of the Results section will provide quantitative data analysis and models that will work out the above ideas and their implications.

Part I: Cell scale analysis

By applying local tension inference to each interface – using the angles it forms with its four neighbors – we can map out the relative tensions in the tissue as shown in Fig. 2C and C'. Initially, relative tensions are close to unity throughout the embryo, since the cell tessellation is approximately a hexagonal lattice, with vertex angles close to 120°. As gastrulation progresses, the cortical tensions change and we start to see characteristic differences between different tissue regions, the amnioserosa and the lateral ectoderm. In the former, interfaces that contract remain under approximately constant tension while interfaces oriented parallel to the direction of tissue stretching (i.e. along the DV axis) extend and are under increasing tension (Fig. 2C). A very different picture emerges in the lateral ectoderm, where we observe an alternating pattern of high and low tensions before intercalations start (22 min). The high tension interfaces contract, leading to coordinated T1 transitions (30 min, cf. Fig. 2C' and Movie 2). As GBE transitions from the fast phase to the slow phase at around 40 min, the pattern of tensions becomes more disordered. We will later find that this increasing disorder plays a key role in determining the transition from the fast to the slow phase of GBE and the total amount of tissue extension.

The differences in the patterns of the inferred tension in the amnioserosa compared to the lateral ectoderm suggest very distinct mechanisms for cell intercalations in these two tissue regions, matching the fact that levels of cortical myosin are very different (high in the lateral ectoderm, low in the amnioserosa [11]). In the following, we first focus on intercalating cell quartets to quantitatively analyze these different mechanisms. A quantitative understanding of the cell scale dynamics will then form the basis for bridging to the tissue scale.

Relative tension dynamics distinguishes active and passive intercalations

We identify all quartets which undergo neighbor exchanges (T1 processes), calculate the length and relative tension of all collapsing and emerging interfaces and align the data at the time of the neighbor exchange [48]. Pooling the data for each of the bands of cells colored in Fig. 1A, we find two distinct scenarios for ventro-lateral quartets and dorsal quartets (Fig. 2D and E; for a breakdown by individual bands, see Fig. S3).

The length dynamics of collapsing and extending interfaces in the amnioserosa and the lateral ectoderm is qualitatively similar (Fig. 2D and E). In the lateral ectoderm, there is a slight increase in interface length before contracting. This transient stretching is caused by the VF invagination that precedes GBE [28]

By contrast, the tension dynamics is markedly different between the amnioserosa and the lateral ectoderm. In the lateral ectoderm, the tension on the contracting edge grows non-linearly and reaches its maximum just before the neighbor exchange. In terms of the local cell geometry, this increasing relative tension reflects the fact that the angles facing away from the interface decrease as the interface contracts (Fig. 2F). Notably, the non-linearly increasing tension, concomitant with an accelerating rate of interface contraction, is evidence that positive tension feedback plays a role in myosin recruitment [26, 27] and is in striking agreement with predictions from a recent model where such feedback is a key ingredient [49]. From the data shown in Fig. 2D we can read off the average relative tension threshold $\langle T_{\mathrm{crit}} \rangle = 1.530 \pm 0.05$ for the interface collapse. As we will see further below, this

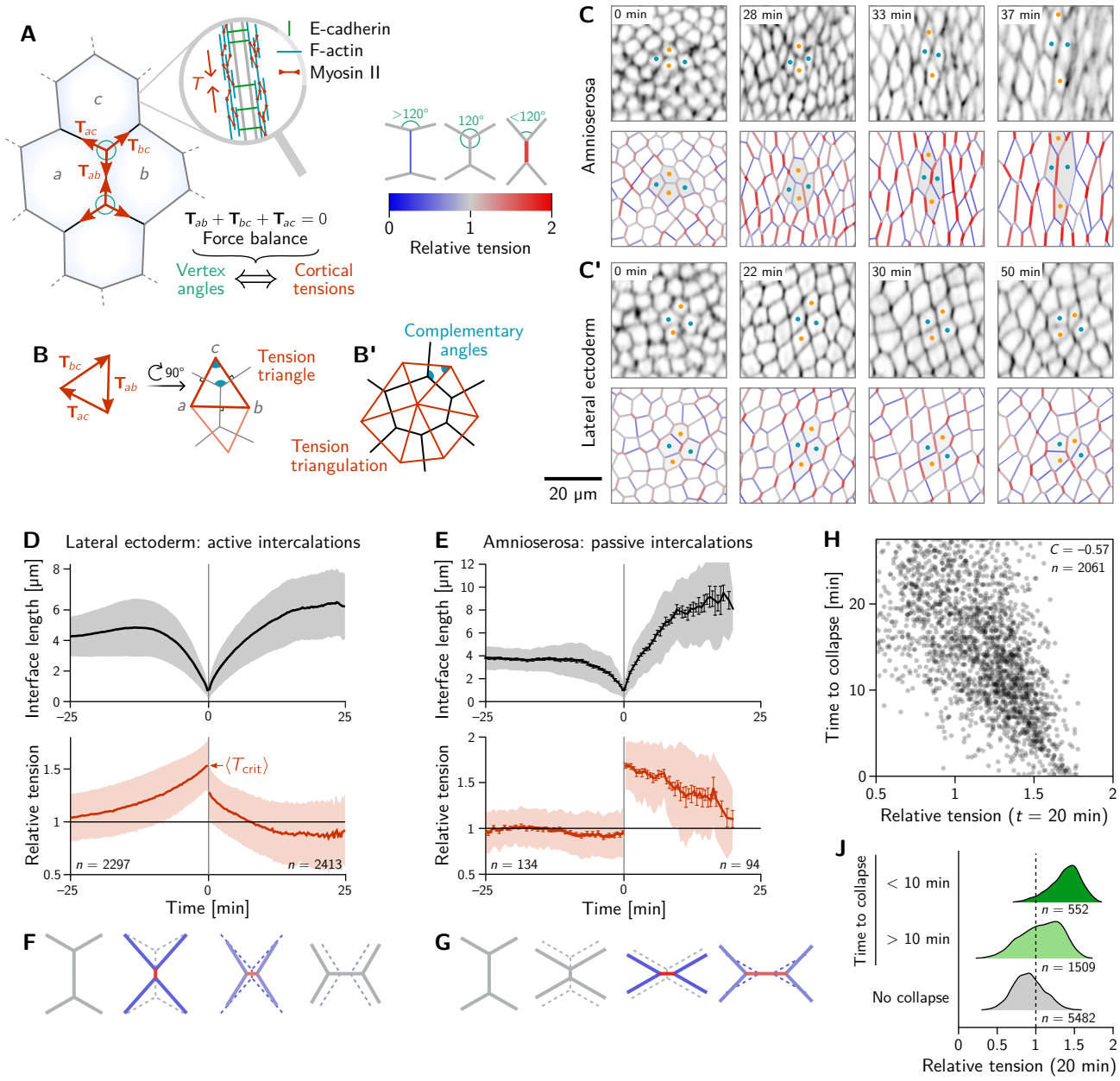

Figure 2: Inferred tension dynamics distinguishes active and passive T1s. A The adherens-junctional cytoskeleton maintains tension in the cortex at cell-cell interfaces via active motors (inset). In force balance, the forces $\mathbf{T}_{ab}$ exerted on a vertex (red arrows) must sum to zero. This allows inferring the relative cortical tensions from the angles at which the interfaces meet at a vertex (see colorbar). **B and B'** The angles in the *tension triangles* formed by the force vectors (rotated by 90°) are complementary to the interface angles at the vertex. Tension triangles corresponding to adjacent vertices share an edge and therefore fit together to form a *tension triangulation* (B'). **C and C'** Relative tensions inferred (bottom) from cell membrane images (top) in the amnioserosa (C) and in the lateral ectoderm (C'). In the lateral ectoderm, high tension interfaces contract. The regular pattern of alternating high and low tension interfaces therefore leads to coordinated T1s (cf. Fig. 1C, bottom). Blue and orange dots mark an intercalating quartet. **D and E** While active and passive T1s show similar dynamics of the length of the inner edge (top), they are markedly different in their tension dynamics (bottom). For lateral cells (D), the tension increases as the interface contracts, providing evidence that positive tension feedback actively drives the edge contraction. For dorsal cells (E), the relative tension remains constant on the contracting edge, indicating that the intercalations are passive. Tension jumps at time zero result from the relation between the angles before and after the neighbor exchange. Collapsing and emerging interfaces were tracked and analyzed separately (see SI Sec. 1.3). Bands and fences show SD and SEM respectively; the SEM in (D) is smaller than the line thickness. **F** The increasing tension of the contracting edge during an active T1 causes the angles opposite of the central interface to become increasingly acute. **G** The hallmark of passive T1s are constant cortical tensions (and thus vertex angles) before the neighbor exchange. This geometrically fixes the vertex angles after the neighbor exchange, such that the emerging edge is under high tension. **H and J** In the lateral ectoderm, relative tension predicts time until a interface collapses (H) and high relative tension predicts which interfaces collapse (J); see Fig. S4 for analogous plots for the amnioserosa

. Relative tensions were averaged from minute 20 to 21 (over four timepoints), i.e. at the end of VFI (cf. Fig. 1E).

threshold can be predicted from simple geometric considerations.

The correlation between increasing tension and interface contraction during active T1s can be used to predict active T1s. Indeed, plotting the time to interface collapse against the relative tension for quartets in the lateral ectoderm shows a clear negative correlation (Fig. 2H). Conversely, relative tensions below 1 correlate with interfaces that never collapse (Fig. 2J).

After the neighbor exchange, the relative tension on the new interface jumps to a lower value and then continues decreasing back to 1, corresponding to vertex angles of 120°. The tension jump at the neighbor exchange is a consequence of geometry: Because the angles facing away from the interface are $< 90°$ before the neighbor exchange, they are necessarily $> 90°$ afterwards. This implies a jump of the relative tension from $> \sqrt{2}$ to $< \sqrt{2}$.

Let us now turn to T1s in the amnioserosa. Here, the relative tension on the inner edge remains almost constant near 1 prior to the neighbor exchange, i.e. the vertex angles remain close to 120° (see Fig. 2G). As a consequence of this homeostatic tension on collapsing interfaces, there is no correlation between relative tension and the time until the interface collapses in the amnioserosa (see Fig. S4). On the new interface emerging after the neighbor exchange, tension is high and remains constant for an extended period. Again, the tension jump at the neighbor exchange is a consequence of geometry. Just before the neighbor exchange the vertex angles are close to 120° which implies that the angles facing away from the interface are 60° after the neighbor exchange (see Fig. 2G). This corresponds to a relative tension of $\sqrt{3} \approx 1.73$ on the central interface.

A tension–isogonal decomposition quantifies active vs passive contributions to tissue deformation

The cortical tensions dynamics inferred from cell geometry show that cell-cell interfaces behave quite counterintuitively and nothing like passive springs. Moreover, they differ significantly between distinct spatial regions of the embryo. To make sense of these observations, we will exploit the deep connection between mechanics and the geometry of the cell tessellation afforded by force balance. This connection will help us explain how cortical tension (controlled by the cells) determines cell and tissue shape. Specifically, we will identify two modes of tissue deformation, one driven by changes in cortical tensions and one driven by external forces and elasticity of the cells' interiors. These two modes can be distinguished on a purely geometric basis. Further, we will find a geometric relation for the critical relative tension at which an interface collapses giving rise to a T1 event. These findings will form the basis for a model that answers the above questions.

Recall that force balance implies that the cortical tensions form a triangulation such that the angles at vertices in the physical cell tessellation are complementary to those in the tension triangulation (Fig. 3A, left). This intimately links tension space and physical space. However, force balance does not uniquely determine the cell tessellation (i.e. the positions of the cell vertices) since interface lengths may collectively change while preserving angles via *isogonal* modes, as illustrated in Fig. 3A, right. Thanks to the relative sliding of cytoskeletal elements (e.g. due to the turnover of passive crosslinkers or walking of myosin motors), the adherens-junctional cytoskeleton can extend or contract under constant tension, behaving like a muscle rather than a spring. Therefore, the isogonal degrees of freedom allow for tissue deformations at fixed tensions (tension homeostasis). They correspond to cell shape deformations driven by external forces or cell-internal stresses (hydrostatic pressure, medial myosin [29, 32], intermediate filaments and microtubules [50, 51]). Associating isogonal deformations to non-junctional (e.g. cell-elastic or external) stresses is based on the assumption that active cortical stresses are the dominant source of stress in the tissue (separation of scales).

The above considerations motivate a decomposition of the tissue deformations into two distinct contributions: deformations of the tension triangulation reflect-

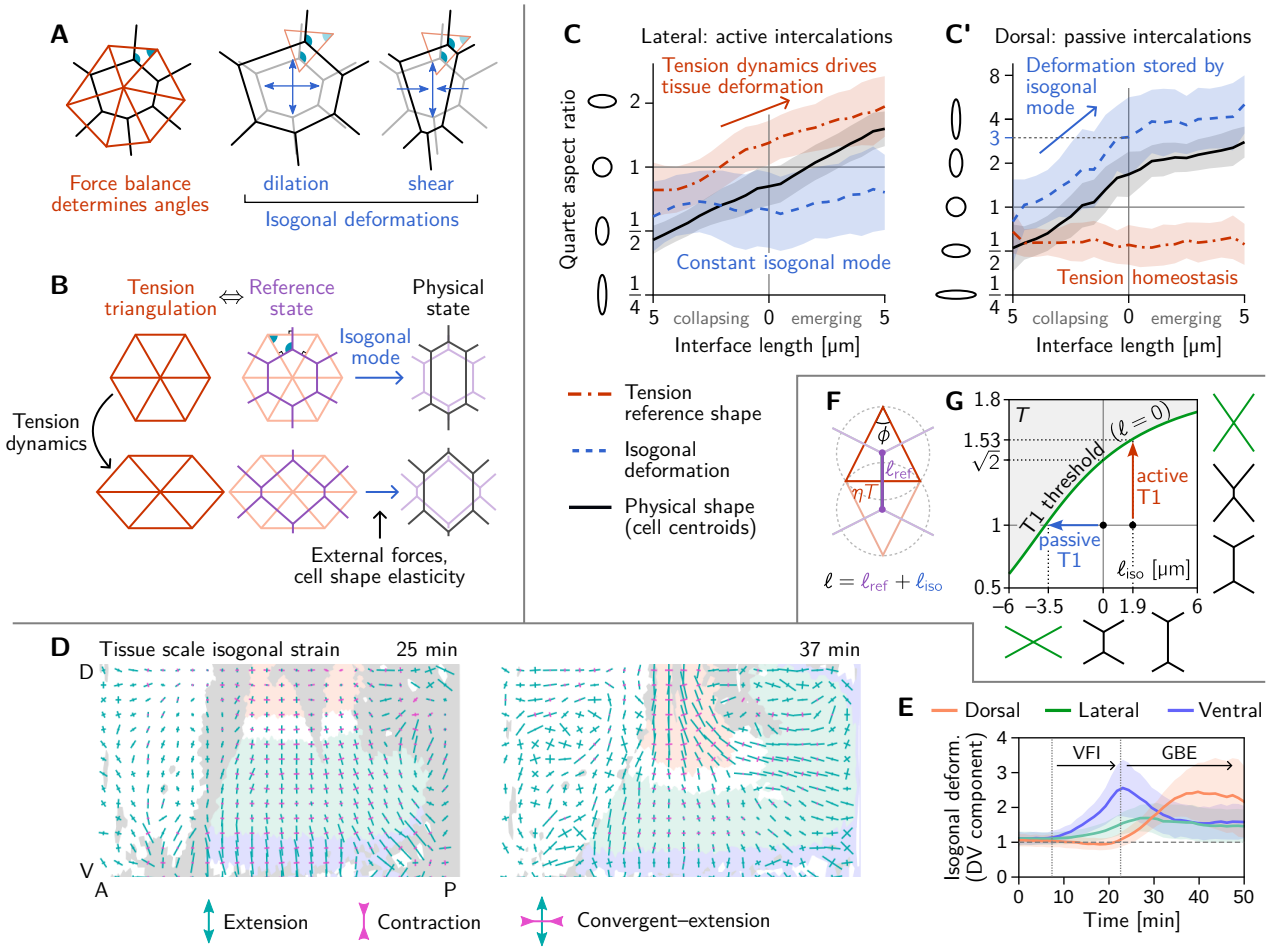

Figure 3: Tension–isogonal decomposition of epithelial geometry identifies active (tension-driven) and passive contributions to tissue deformation. A The angles in the tension triangulation (red) are complementary to those in the cell tessellation (black) (left). The triangulation acts as a scaffold which leaves freedom for isogonal (angle preserving) deformations which encompass both dilation (center) and shear (right). **B** Deformations of the physical cell tessellation (black, right) can be decomposed into deformations of the tension triangulation (red, left) and isogonal deformations (blue). The former reflect the dynamics of cortical tensions while the latter reflect the effect of external forces and cell shape elasticity. A reference cell tessellation (purple, e.g. a Voronoi tessellation) constructed from the tension triangulation serves as an intermediate relative to which the isogonal deformations are defined. **C and C'** Quartet shape (aspect ratio) and isogonal mode plotted against the length of the quartet's inner interface, which serves as a pseudo-time parametrization. An aspect ratio of 1 indicates an isotropic quartet shape and no isogonal deformation, respectively. Active T1s (left), are driven by a deformation of the tension triangulation while the isogonal mode remains constant. Passive T1s (right), are driven by isogonal deformations while the shape of the tension triangulation remains constant. Bands indicate SD; SEM is smaller than the line width. **D** Tissue scale isogonal strain at the end of VF invagination (left, 25 min) and during GBE (right, 37 min). Crosses indicate the principal axes of isogonal strain, averaged over cells in a grid with 20 μm spacing. Bar lengths indicate the magnitude of strain (green: extensile, magenta: contractile). Colored tissue regions are quantified in (E). **E** Time traces of the DV component of isogonal strain. VF invagination drives a strong and transient isogonal stretch of the tissue adjacent to the VF (purple) and a weaker, persistent stretch of the lateral ectoderm (green). The amnioserosa (red), is stretched as the lateral ectoderm contracts along the DV axis during GBE. (DV component is defined with respect to the local co-rotating frame, see SI; Shaded bands show one SD; SEM is comparable to the line width.) **F** A symmetric pair of tension triangles is characterized by a single angle ϕ. The cell quartet's central interface in the Voronoi reference configuration (purple) connects the triangles' circumcenters. **G** T1 threshold for symmetric cell quartets in the T-ℓ_{iso} plane. Along the T1 threshold, the physical interface length $\ell = \ell_{ref} + \ell_{iso}$ vanishes. The threshold can be reached by isogonal contraction under constant relative tension (blue arrow) or by active contraction under increasing relative tension (red arrow).

ing changing cortical tensions and isogonal (angle-preserving) deformations (see Fig. 3B). We will call this a *tension–isogonal decomposition*. Implicitly, this decomposition uses the fact that we can construct a reference state for the cell tessellation from the tension triangulation (e.g. using the Voronoi tessellation). Isogonal deformations then transform this reference state into the physical cell tessellation. In practice, we do not need to explicitly construct the reference cell tessellation. Instead, we utilize the fact that the physical cell tessellation can be quantified by the triangulation defined by the cells' centroids [52]. The tension triangulation directly serves as reference to which we can compare the centroidal triangulation to infer the isogonal deformations.

We first apply the tension-isogonal decomposition to intercalating quartets. For a given quartet of cells labelled $i = 1{-}4$, we quantify the physical shape in terms of the centroid positions $\mathbf{c}_i$ by calculating the moment of inertia tensor (see Fig. 3C). The tension reference shape is given by the tension vectors $\hat{\mathbf{T}}_{ij}$, which are obtained from the interface angles using tension inference and are rotated by 90° relative to the interfaces (see Fig. 2B). The ratios of eigenvalues of the moment-of-inertia tensors defines the shape aspect ratios, illustrated by ellipses in Fig. 3C–C'. The quartet's isogonal deformation tensor $\mathbf{I}_{\text{quartet}}$ transforms the cell centroids into the tension vertices $\eta\,\mathbf{I}_{\text{quartet}}.\hat{\mathbf{T}}_{ij} = \mathbf{c}_i - \mathbf{c}_j$. Given $\hat{\mathbf{T}}_{ij}$ and $\mathbf{c}_i$, $\mathbf{I}_{\text{quartet}}$ can be obtained using least squares. The constant, global scale factor $\eta \approx 6\,\mu\text{m}$ translates units from relative tensions (a.u.) to length (µm) and is fitted to minimize initial strain in the initial state.

In Fig. 3C and C', we plot the quartet shape aspect ratios and the elongation factor of the isogonal deformation against the length of the quartet's inner edge, which serves as pseudo-time parameterizing the T1 process. (Plots against real time are shown in Fig. S6B and B'.) In the lateral ectoderm (Fig. 3C), the tension-triangle deformation leads the quartet shape deformation, indicating that tension dynamics drives the intercalation. This confirms our conclusion from the relative tension analysis (Fig. 2D). In contrast, the isogonal strain is approximately constant and, in fact, slightly counteracts the deformation. This is a consequence of the ventral furrow invagination which pulls on the lateral ectoderm cells and passively stretches them along the DV axis. A very different picture emerges in the passively deforming amnioserosa (Fig. 3C'). Here, the tension triangles do not change shape, indicating tension homeostasis, while the cell quartet deformation is entirely stored in the isogonal mode. While the behaviors observed in the lateral ectoderm and in the amnioserosa represent the extreme cases, being purely tension driven (active) in the former and purely isogonal (passive) in the latter, there is continuous spectrum in between. Intermediate scenarios where both cortical tensions and external stresses contribute to tissue deformation are conceivable.

So far, we have focused our analysis on intercalating cell quartets. However, the tension–isogonal decomposition can be applied anywhere in the tissue without the need to track cells and identify T1 events. To that end, we adapt the procedure introduced above for cell quartets (Fig. 3C) to any triplet of cells that meet at a vertex (see SI Sec. 1.5 for details). This yields the isogonal deformation tensor for that vertex. Locally averaging over nearby vertices yields the tissue-scale isogonal deformation (see Fig. 3D). At the end of VF invagination (25 min), significant isogonal strain has built up near the VF as the tissue is passively stretched along the DV axis there (see purple shaded region in Fig. 3D). The large isogonal strain in this region reduces the number of intercalations during GBE (see Fig. S1D). The lateral ectoderm further away from the VF also accumulates some isogonal extension along the DV axis (green shaded region, see time traces in Fig. 3E). This causes an increase in the tension threshold for active T1s in the lateral ectoderm, as discussed in the previous section.

During GBE (Fig. 3D, 37 min), the isogonal strain near the ventral furrow relaxes back to nearly isotropic, suggesting that the deformation stored in the isogonal mode is elastic rather than plastic (Fig. 3E). At the same time, the actively contracting lateral ectoderm stretches the dorsal tissue along the DV axis. There is

also significant isogonal strain along the advancing front of the posterior midgut. Taken together, isogonal strain identifies regions where passive tissue deformation is caused by mechanical coupling across the tissue.

Taken together, the tension–isogonal decomposition quantitatively distinguishes between active and passive intercalations. Tensions are controlled locally, while the isogonal modes accommodate external, non-local forces, such as pulling by adjacent tissue. We associate isogonal deformations with passive deformations because active stresses in the lateral ectoderm are generated at interfaces. In systems where active stresses are generated in the cell's interior, e.g. due to nuclear migration [53] or due to intracellular actin cables [54], the isogonal mode is actively driven. Another example for this is apical constriction during VF invagination which is driven by medial myosin pulses that drive isogonal cell contractions [13].

Tension space geometry sets the threshold for interface collapse

A puzzle that has remained open in our analysis so far is the threshold for interface collapse and cell neighbor exchange. In the lateral ectoderm, where the isogonal strain is approximately constant (Fig. 3C), the neighbor exchange takes place at a critical relative tension of 1.530 ± 0.005 on average (cf. Fig. 2D). By contrast, in the amnioserosa, where T1s take place under constant tension (Fig. 2E), there is an average critical aspect ratio ~ 3 of the isogonal deformation at the point of neighbor exchange (see Fig. 3C').

As we will see, one can explain these numbers in terms of the geometric tension–isogonal decomposition introduced above. We start by decomposing the length ℓ of a cell quartet's central interface into a reference length $\ell_{\mathrm{ref}}(\{T_i\})$, determined purely in terms of the local relative tensions, and an isogonal length ℓ_{iso}:

$$\ell = \ell_{\mathrm{ref}}(\{T_i\}) + \ell_{\mathrm{iso}}. \tag{1}$$

A neighbor exchange takes place when ℓ shrinks to zero. From the decomposition Eq. (1) it is apparent that the interface collapse can be driven by the isogonal mode, by changes in tensions, or by a mixture of both.

Let us start with the passive T1s observed near the dorsal pole. In this case, the relative tensions are homeostatic (cf. Fig. 2E), so $\ell_{\mathrm{ref}} \approx \langle \ell(0) \rangle \approx 3.5\,\mu\mathrm{m}$ remains constant. The neighbor exchange therefore happens when $\ell_{\mathrm{iso}} = -\langle \ell(0) \rangle$ (see blue arrow in Fig. 3G). By a geometric construction (Fig. S6D) one finds that the corresponding isogonal deformation has an aspect ratio of 3, in good agreement with observations (Fig. 3C').

To find the tension threshold for active T1s, we calculate ℓ_{ref} using the Voronoi construction based on the vertices of the tension triangulation (see SI Sec. 1.6 for details). The length of a quartet's central interface in the Voronoi reference state is determined by the pair of tension triangles corresponding to the cell quartet (see Fig. 3F). For simplicity, we consider the case of two identical, isosceles triangles which is fully characterized by the relative tension $T = 2\sin(\phi/2)$ on the central interface, with ϕ the angle in the tension triangle. (The general case of asymmetric tensions is discussed in the SI.) The Voronoi construction for the reference length then yields $\ell_{\mathrm{ref}} = \eta T \cot(\phi)$. The condition $\ell_{\mathrm{ref}}(T) \stackrel{!}{=} -\ell_{\mathrm{iso}}$ for the neighbor exchange now defines the "T1 threshold" in the ℓ_{iso}-T plane (see Fig. 3G).

In this diagram, (active) tension dynamics and (passive) isogonal strain appear as orthogonal ways to drive T1s, as illustrated by the red and blue arrows. In the absence of isogonal deformations ($\ell_{\mathrm{iso}} = 0$), the interface length vanishes when $\phi = \pi/2$, implying the critical relative tension $T_{\mathrm{crit}}(\ell_{\mathrm{iso}} = 0) = \sqrt{2} \approx 1.41$. In the lateral ectoderm, in particular near the VF (purple region in Fig. 3D), DV oriented interfaces are stretched due to VF invagination. The average isogonal contribution to interface length $\langle \ell_{\mathrm{iso}} \rangle \approx 1.9\,\mu\mathrm{m}$ of DV oriented interfaces in the lateral ectoderm can be estimated from the tissue-scale isogonal strain there (cf. Fig. 3D). One can

read off the predicted relative tension threshold $T_{\text{crit}} \approx 1.53$ in Fig. 3G. This is in excellent agreement with the value found by tension inference (Fig. 2D). For *twist* and *snail* mutants where the VF is abolished such that there is no isogonal stretching of the lateral ectoderm, we predict a T1 threshold $T_{\text{crit}} \approx \sqrt{2}$ for active T1s. This implies that there will be no tension jump between the contracting and the extending interface for active T1s.

Minimal local model based on tension feedback reproduces length- and tension-dynamics of T1s

We conclude our quartet-level analysis by condensing the insights gained into a parsimonious model that combines tension dynamics with a constitutive relation for the isogonal modes. Importantly, we model the dynamics in adiabatic force balance. That means that the positions of the vertices do not follow some explicit dynamical equation (like the overdamped energy relaxation dynamics in a classical vertex model) but are instead implicitly determined from a tension triangulation and the isogonal modes.

To keep the number of parameters and variables (degrees of freedom) in the model to a minimum, we consider a quartet of cells with identical shapes. This describes a representative quartet in a regular (periodic) cell array. Such a cell array is characterized by the three angles at each vertex, ϕ_i, and the three interface lengths ℓ_i, with $i \in \{0, 1, 2\}$ (see Fig. 4A). The vertex angles are determined by the relative cortical tensions T_i via the force balance condition (see Fig. 3A). Motivated by the nonlinearly increasing tension observed on contracting interfaces (cf. Fig. 2D), we equip each interface with self-reinforcing tension dynamics

$$\tau_{\text{T}} \partial_t T_i = T_i^n - \frac{1}{3} \sum_k T_k^n, \tag{2}$$

which models tension-induced myosin recruitment [26] (with excitability exponent n being set to $n = 4$ in our simulation). The dynamics conserves the total active tension $\sum_i T_i$, corresponding to a finite myosin pool in each cell. (Other choices for fixing the overall scale of tension, e.g. via the triangle area, as well as well as other values of n do not change the results qualitatively; see SI.) The timescale of tension dynamics τ_{T} is fitted to the experimental data. The positive tension feedback drives the relative tension on the quartet's central interface towards the tension threshold discussed above (see Fig. 4B) and thus drives active T1s. The interface that collapses is the one that starts with the highest initial tension, which we label with $i = 0$ by convention.

To find the physical cell shape, we need to fix both the angles and the isogonal mode that determines the interface lengths ℓ_i (Fig. 4C). To this end, we introduce a cell elastic energy which is minimized by the isogonal mode. This elastic energy accounts for rigid elements of the cell that do not reside on interfaces, such as intermediate filaments and the nucleus, and we assume its scale to be much smaller than the elastic energy due to cortical tensions. Because of this separation of scales, the angles at vertices are fixed by tensions, and the relaxation of the cell elastic energy only affects isogonal modes. We posit the cell elastic energy

$$E_{\mathcal{C}} = \lambda \left[\text{Tr}(\mathbf{S}_{\mathcal{C}} - \mathbf{S}_0)\right]^2 + \mu \, \text{Tr}[(\mathbf{S}_{\mathcal{C}} - \mathbf{S}_0)^2] \tag{3}$$

which measures the difference between the cell "shape tensor" $\mathbf{S}_{\text{C}} = \sum_i (\mathbf{e}_i \otimes \mathbf{e}_i)/\ell_i$ and a target shape tensor $\mathbf{S}_0$. Here, $\mathbf{e}_i$ are the interface vectors with lengths $|\mathbf{e}_i| = \ell_i$ (see Fig. 4A) and $\otimes$ denotes the tensor product. We choose this energy because it does not change if a vertex is artificially added or subtracted to a cell since it is linear in interface length (for a comparison with other choices, see SI). The coefficients λ and μ control the cell's resistance to isotropic compression/dilation and shear deformations, respectively (see SI for details). Notably, this elastic energy does not engender an "energy barrier" for T1 transitions as is found in vertex models with

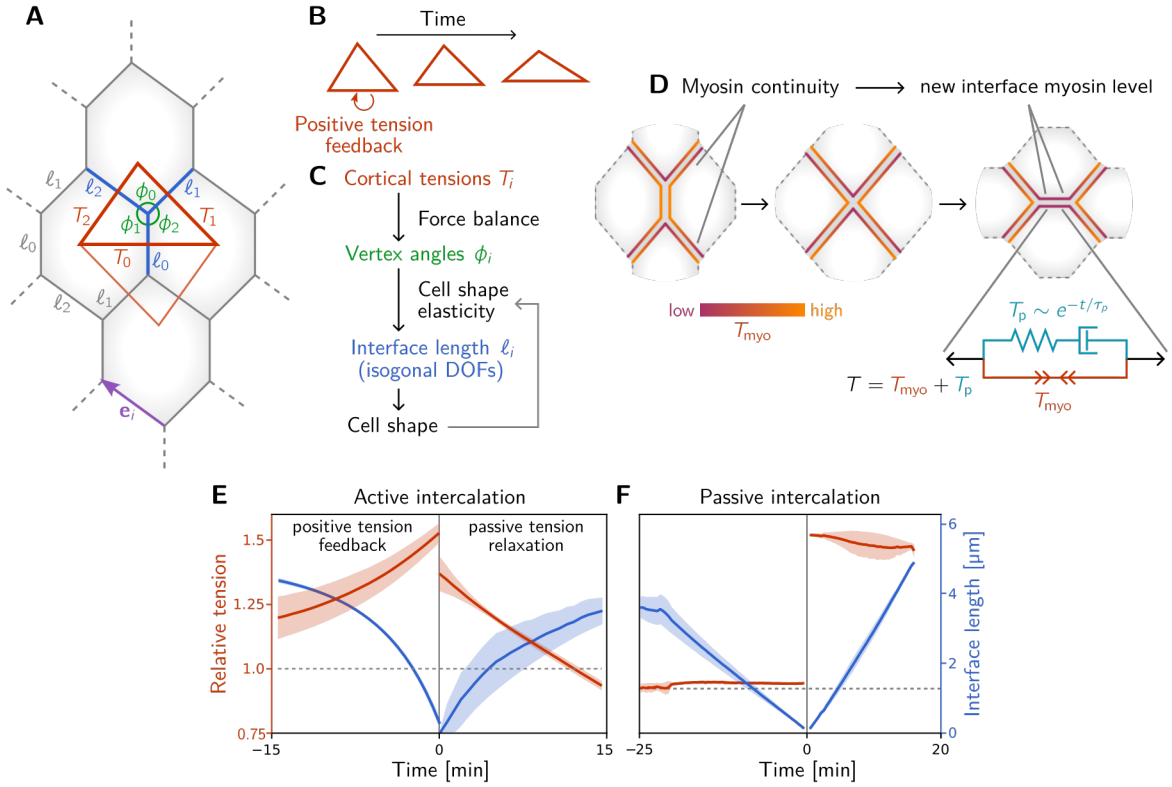

Figure 4: A minimal model for positive tension feedback reproduces the signatures of active T1s, and creates passive T1s when feedback is deactivated. **A** Single cell quartet of identical cells forms the elementary setting for modelling T1s. This geometry is characterized by two vertex angles (ϕ_0, ϕ_1, and $\phi_2 = 2\pi - \phi_0 - \phi_1$) and three interface lengths (ℓ_i). The interface angles are determined by the pair of identical tension triangles corresponding to the cell quartet. To avoid boundary effects, the cell quartet and tension triangles are set up to tile the plane periodically as a regular lattice. **B** Positive tension feedback causes the longest edge in a tension triangle to grow fastest, deforming the triangle to become increasingly obtuse. (We fix the total tension scale. In real cells, the overall tension scale is set by the available myosin pool. Relative tensions change as myosin is redistributed between the cortex at different interfaces.) **C** The tension triangle shape determines the vertex angles, ϕ_i. To fix the interface lengths ℓ_i, we constrain the cell shape by minimizing an elastic energy (see SI for details). **D** Two-sided architecture of junctional cortex determines myosin level on newly formed interface. Sketch of intercalating quartet with myosin in each cell's cortex color-coded coded. After a neighbor exchange, the active tension (i.e. myosin level) on the new edge is determined by a "handover" mechanism that assumes continuity of myosin concentration at vertices within each cell. As consequence, the active tension on the new edge right after the neighbor exchange is below the total tension that is determined by geometry. This tension imbalance causes the new edge to extend by remodeling. To capture the remodeling, we introduce a passive viscoelastic tension T_{passive}. due to passive cortical crosslinkers. T_{passive} decays exponentially with a characteristic remodeling time τ_p. Notably, no additional active ingredients (like medial myosin contractility) are required to drive extension of the new edge. **E and F** The model reproduces the signatures of active and passive T1s observed in the *Drosophila* embryo. The tension feedback rate and passive relaxation rate are fitted to match the observed timescales. (Bands show the standard deviation from an ensemble of simulations with initial angles drawn from the experimental vertex angle distribution at 0 min.)

area–perimeter elasticity [55]. Therefore, our simulations do not require stochastic fluctuations to drive T1s.

The model described thus far models the dynamics up to the neighbor exchange (time < 0 in Fig. 4E and F) and qualitatively reproduces the dynamics of interface length and tension observed in the experimental data (cf. Fig. 2D). Interface contraction during an active T1 is driven by active remodeling of the force balance geometry: Myosin recruitment increases the cortical tension and thus drives it out of force balance with the external tension from adjacent interfaces. As a result, the interface remodels – changing the interface angles until force balance is reestablished. Positive tension feedback continually causes further myosin recruitment, which in turn drives further contraction until the interface has fully collapsed.

How does the subsequent resolution and interface elongation work? On the emerging interface, there is typically little myosin [23, 56]. Therefore, active contractility cannot balance the external tension exerted on the interface by its neighbors – the new interface is thrown out of active force balance. This force imbalance naturally leads to the extension of the new edge. As the interface extends, passive tension bearing elements of the cytoskeleton, such as crosslinkers, get loaded until force balance is reestablished. To account for this, we split the total cortical tension T into the myosin-borne, active tension T_{myo} and the passive tension T_{p}. Cortical remodeling due to turnover of crosslinkers will gradually relax this passive tension. We account for this by an exponential decay $T_{\mathrm{p}} \propto e^{-t/\tau_{\mathrm{p}}}$ with a characteristic remodeling rate τ_{p}. This passive tension effectively represents Maxwell-type viscoelasticity of the extending interface, illustrated by the spring and dashpot in Fig. 4D.

Completing the model requires to understand what sets the the initial motor protein level on an emerging interface, which will set the initial condition for the tension dynamics on that interface. We propose a myosin "handover" mechanism that is based on the assumption that the myosin level along the cortex within each cell changes continuously at vertices [57] (see Fig. 4D). (Force balance requires that the total tension, the sum of the tensions in the two abutting cortices, is uniform along an interface. However, the individual tensions on either side can be non-uniform, as the resulting traction forces are exchanged via E-cadherin molecules linking the cells along the interface [35].) Importantly, this handover model predicts that the myosin level on the newly formed interface is generically lower than that on the collapsing interface, in agreement with experimental observations [23, 56].

Simulating this model, we find good qualitative agreement between the single-quartet model and experimental data, both for the tension dynamics (compare Fig. 4E,F and Fig. 2D,E) and for the tension–isogonal decomposition (compare Fig. S17A.A' and Fig. 3C,C'). Movie 3 shows the simulation of an active T1 transition for a symmetric quartet. Without positive tension feedback, prescribing instead the displacement cell centroids to mimic external stresses, the model successfully describes passive intercalations (Fig. 4F; see SI Sec. 4.3 for details).

Notably, in our model the mechanism of interface extension is identical for active and passive T1s. Interface extension is a consequence of the fundamental temporal asymmetry of T1 processes: high myosin levels on the collapsing interface versus low myosin levels on the elongating interface. No additional active ingredients are required. Note that we have ignored myosin fluctuations in the above arguments. If these fluctuations are strong compared to the average myosin levels, they may cause the collapse of the emerging interface, thereby reversing a T1, as observed in some genetic mutants [48].

Part II: Tissue scale

Initial anisotropy and local order of tension sets up tissue scale flow

Tissue scale anisotropy of active tension is central to drive and orient convergent–extension flow [11, 56, 58, 59]. If cortical tensions are regulated by positive feedback, tissue anisotropy sets the orientation the interfaces which will collapse, and hence, the direction of tissue flow. Moreover, we have observed that the active T1s driving the flow happen in a highly coordinated fashion, namely "in parallel" (see Fig. 1C, bottom). This requires spatial coordination of the tension dynamics that drives active T1s. Because the tension dynamics in our model is purely autonomous, we hypothesize that anisotropy and coordination need to be encoded in the initial condition.

We asses tension anisotropy by locally averaging the anisotropy of inferred tensions $\mathbf{T}_{ij}$ at a given individual vertices as illustrated in Fig. 5A (see SI for details). The inferred tension anisotropy (Fig. 5B) and its time course (Fig. 5C) are consistent with earlier experimental observations: During VF invagination, DV oriented interfaces in the lateral ectoderm are stretched causing myosin recruitment [28]. Remarkably, we find strong DV alignment of tension anisotropy in the trunk already before VF invagination (Fig. 5D, 0 min). This confirms our hypothesis that tension anisotropy is set up in the initial condition. As GBE progresses, the DV alignment of tension anisotropy decreases (Fig. 5C and Fig. 5D, 37 min). Because the tension anisotropy orients active T1s, this increasing disorder may be responsible for the slowdown of GBE. Indeed, we will confirm this hypothesis in numerical simulations discussed further below.

Tissue scale tension anisotropy is not enough to drive choreographed "parallel" T1s. Such coordination requires an alternating pattern of high and low tensions as seen in Fig. 5E (center; cf. Fig. 2C'). In contrast, when several connected interfaces are under high tension, they form a tension cable which leads to rosette formation [26, 60].

Because the tissue is inherently disordered, the above patterns of tension do not appear globally, but rather as local motifs that can be distinguished based on the tension configuration at individual vertices. These configurations correspond to characteristic triangle shapes in the tension triangulation (see Fig. 5F): The elementary motif of the alternating tension pattern is a "tension bridge" where a high tension interface is surrounded by low tension interfaces (see Fig. 5E, right), corresponding to an obtuse triangle (Fig. 5F, top right). In contrast, an acute tension triangle correspond to the local motif of a tension cable, where neighboring interfaces along the cable are under high tension while those transverse to the cable are under low tension (see Fig. 5E, left; and Fig. 5F, bottom right). We can therefore use the tension triangle shape to define a *local tension configuration* (LTC) parameter that informs about the coordination of tension on the interfaces that meet at a vertex. The LTC-parameter space (i.e. the space of triangle shapes), shown in Fig. 5F, is spanned by two axes, quantifying the magnitude of anisotropy and how acute or obtuse the triangle is. The geometric condition for neighbor exchanges discussed above (and in SI Sec. 1.6) defines a threshold in the LTC-parameter space (dashed line in Fig. 5F). When the shapes of a pair of adjacent tension triangles crosses this threshold, an edge flip in the triangulation occurs – corresponding to a cell neighbor exchange (T1 transition). It is immediately apparent that for tension cables (acute tension triangles) the tension anisotropy required to cross the T1 threshold is higher compared to tension bridges. Tension cables are therefore less efficient at driving T1s: they require stronger anisotropy of tension to cause an interface collapse.

Histograms of the LTC parameter distribution in the lateral ectoderm from different timepoints during *Drosophila* gastrulation show that the fraction tension bridges (obtuse tension triangles) increases before the onset of GBE (see Fig. 5G).

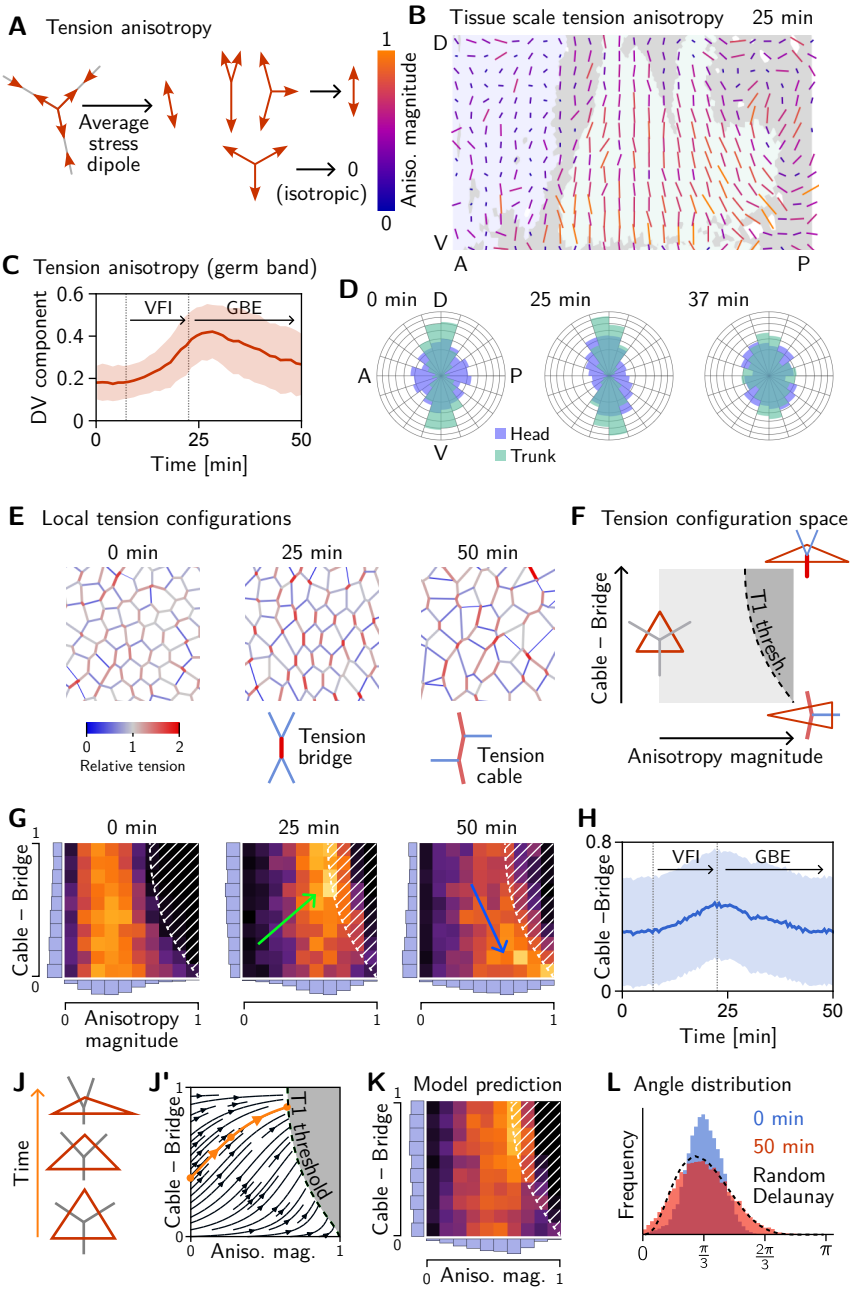

Figure 5: Tension anisotropy and LTC order orient and coordinate active T1s. A Local anisotropy of tension (double-ended arrow) at a single vertex. Different tension configurations correspond to the same net tension anisotropy. **B** Line segments indicating the local orientation and magnitude (length and color of the line segments) of tension anisotropy at the end of VF invagination/onset of GBE (25 min). Tension anisotropy was locally averaged on a grid with $20\,\mu m^2$ spacing. **C** Mean DV component of locally averaged anisotropic tension in the trunk (green region in **B**). (DV component measured along a fixed axis orthogonal to the long axis of the embryo; Shading shows SD.) **D** Significant DV alignment of the tension orientation in the trunk precedes any tissue flow, while the tension in the head shows no orientation bias (0 min). The DV alignment of tension decreases during GBE (37 min). **E** Distinct configurations of tension on the cell scale. Tension bridges are the elementary motif of an alternating pattern of high and low tension (center) that coordinates T1s to proceed "in parallel" (cf. Fig. 1C, bottom). In contrast, tension cables correspond to configurations where several subsequent interfaces are under high tension, which is incompatible with active T1s and leads to rosettes. **F** Space of local tension configurations at a single vertex (quantified by the tension triangle shape, see SI Sec. 1.8 for details). The dashed line indicates the "T1 threshold" calculated for the average isogonal strain in the germ band (cf. Fig. 3G). **G** Distribution of tension triangle shapes in the lateral ectoderm. Arrows highlight the increasing fraction of tension bridges during VF invagination (0–25 min) and its decrease during GBE (25–50 min). **H** Median of the obtuse-acute triangle shape parameter in the lateral ectoderm. (Shading shows SD; SEM is smaller than the line width.) **J and J'** Positive tension feedback drives tension triangles towards more anisotropic and obtuse shapes, corresponding to increasingly bridge-like tension configurations. **K** Starting from the initial tension triangle shape distribution observed in the lateral ectoderm (0 min in **G**), positive tension feedback transports the distribution to close agreement with the one observed at the onset of GBE (cf. 25 min in **G**). **L** Initial and final angle distributions in the lateral ectoderm compared to a random Delaunay triangulation. The initial distribution matches a perturbed equilateral triangular lattice.

The bridge fraction reaches its maximum around 25 min, just at the onset of GBE (see Fig. 5H). The corresponding alternating pattern of tensions is clearly visible in Fig. 5E (center). This suggests that the pattern of tensions on the (sub-)cellular scale is biologically relevant to choreograph parallel T1s.

What drives this emerging pattern of LTC? Consider a single tension triangle. Starting from a configuration with nearly equal tensions, i.e. a nearly equilateral triangle, positive tension feedback causes the highest tension (longest edge in the triangle) to grow fastest. The triangle is thus driven towards an increasingly obtuse shape as illustrated in Fig. 5J and J' and Fig. S16B. Indeed, starting from the experimentally observed distribution of tension configurations (tension triangle shapes) at time 0 min, this simple "single-triangle" model reproduces the tension configuration distribution at 25 min (see Fig. 5K and marginal distributions in Fig. S16C and C').

As the triangle shape becomes more elongated, it eventually hits the "T1 threshold" where a cell neighbor exchange happens. In the single-triangle simulation, we remove triangles that have reached the T1 threshold to account for the corresponding triangulation edge flips. The shape space beyond the T1 threshold is not accessible as is also apparent from the experimental data.

In the experimental data, we observe that the fraction of tension bridges decreases and the fraction of tension cables increases as T1s happen (see Fig. 5G, 50 min and see Fig. 5H). In fact, the distribution of tension triangle shapes appears to approach that of a random Delaunay triangulation (Fig. 5L), which is the maximally disordered distribution. This suggests that the triangle edge flips can be statistically understood as a random "mixing" process that generically causes a loss of LTC order and global alignment of tension anisotropy. In turn, the loss of LTC order causes active T1s to become incoherent and incompatible between adjacent cells, leading to a slow down of tissue extension. Indeed, these hypotheses will be confirmed by tissue scale simulations presented in the next section.

Tension-triangulation based model bridges tissue and cell scale dynamics

Above, we have shown that positive tension feedback explains the dynamics of a single intercalating cell quartet (see Fig. 4) and the statistics of local tension configurations (see Fig. 5J and K). We now ask whether we can also understand the tissue scale dynamics within the scope of this framework. To that end, we generalize the model of tissue dynamics in adiabatic force balance from a quartet of cells in a periodic cell array to a general cell tessellation (see SI for details). All parameters are set identical to the single-quartet simulations. Again, the model is based on adiabatic force balance: cell geometries are computed by minimizing an elastic energy with angles constrained by a tension triangulation, whose positive-feedback dynamics drives tissue flow.

To mimic the cylindrical geometry of the embryo with fixed circumference, we simulated a rectangular tissue patch with "slip walls" at the top and bottom boundary, corresponding to the dorsal pole (Fig. 6A, note that only the top half of the simulation domain is shown). The centroids of cells along the slip walls, marked by black disks, are restricted to move parallel to the wall. In the embryo, the dorsal amnioserosa and the lateral ectoderm cells behave differently. We incorporate this mechanical patterning into our model by dividing the tissue patch into active and passive regions. Cortical tensions are governed by positive feedback in the active region and by tension homeostasis in the passive region. Further, passive cells are taken to be softer and can relax their reference shape viscoelastically [61]. We initialize the simulation with the experimentally observed tension anisotropy aligned along the DV axis (cf. Fig. 5C). The tension triangulation is therefore slightly elongated along the AP axis (recall that the tension triangles are rotated by 90° so that a higher DV tension appears as a tension triangle elongation along AP, cf. Fig. 3A).

Starting from this initial condition, the simulation reproduces salient features

of the tissue-scale dynamics in the embryo (see Movie 4). The lateral ectoderm extends along the AP axis while the amnioserosa is stretched along DV (see Fig. 6B). On the tissue level, the coupling of active and passive regions gives rise to the tissue flow pattern characteristic of GBE [11] (Fig. 6C and K). On the cell scale, the simulations reproduce the coordinated active T1s in the lateral ectoderm (see magnified snapshots in Fig. 6D; cf. Fig. 1C) and the passive intercalations in the amnioserosa.

Strikingly, we find that tissue flow stalls after a finite amount of convergent extension as the tissue becomes increasingly disordered. To quantitatively investigate the effect of disorder on the flow speed, we performed simulations using a rectangular patch of active cells with free boundaries. The x-fold change in the length and height of the patch over time revealed an initial fast phase followed by a continued slower phase. To quantify disorder, we measured the cell shape index ($s = [\text{cell perimeter}]/\sqrt{[\text{cell area}]}$), which rapidly approached the distribution for a random Voronoi tessellation (see Fig. 6F). This finding is consistent with the tension triangulation approaching a random Delaunay distribution (Fig. 5L). The disorder in the cell shapes is driven by disorder in the pattern of cortical tensions that determine the tri-cellular vertex angles. The tension triangles in the simulation also approach a random Delaunay distribution (Fig. S9D), in agreement with experimental observations (Fig. 5L and Fig. S9C). In real space, this manifests in tension cables and a loss of large-scale tension anisotropy (see Fig. S13B), causing T1s to become incoherent. Together, these findings provide an elegant explanation for the transition from the fast phase to the slow phase of GBE.

To further investigate the role of disorder, we performed simulations initialized with highly disordered cell packings (based on a random Voronoi tessellation, see Fig. S14A and Movie 5) that had the same degree of tension anisotropy as the above simulations (see SI Sec. 4.4 for details). We find that the lack of hexagonal order in the initial cell packing prevents the emergence of LTC order and thus results in much slower tissue extension (Fig. 6E), matching the late stages of simulations that started with an ordered tissue. Interestingly, merely adding more noise to the vertex position in a hexagonal lattice does not impede tissue extension (see Fig. S14C). We conclude that hexagonal order of the initial cell packing is required for positive tension feedback to generate LTC order, which in turn is required to drive fast tissue flow by coherent T1s. Since T1s convert hexagonal cells into pentagons and heptagons, tissue flow naturally slows down after the first rounds of T1s. In the *Drosophila* embryo, the initial hexagonal packing of cells is created through physical interactions of the spindle apparatuses prior to cellularization [62, 63]. We predict that disrupting this packing order will cause GBE to become slower. More broadly, our results suggest that convergence extension via positive tension feedback may generally be self-limiting, as also observed in a recent model [49]. Further studying the role of cell scale order for active tissue flow is a promising avenue for future research.

Tissue extension by active T1s requires cell shape rigidity

The tissue–scale model allows us to investigate how tissue extension depends on tissue material properties, such as the cell elastic energy and the positive tension feedback. In the following, we investigate the role of these properties and their spatial modulation, which is determined by genetic patterning.

In simulations where the cells' shear modulus μ is set to zero, we find no tissue elongation (see Fig. S11 and Movie 6). Instead, the deformation of the tension triangulation – driven by positive tension feedback – and the resulting active T1s, are fully compensated by isogonal deformations which causes the cells to elongate along the DV axis. This can be understood by considering a single intercalating quartet, as shown in Fig. 1B, bottom. A neighbor exchange results in net tissue extension (i.e. a change in quartet's aspect ratio) only if the shape of the cells remains round (isotropic). Cell shape rigidity is required to suppress the isogonal deformations by

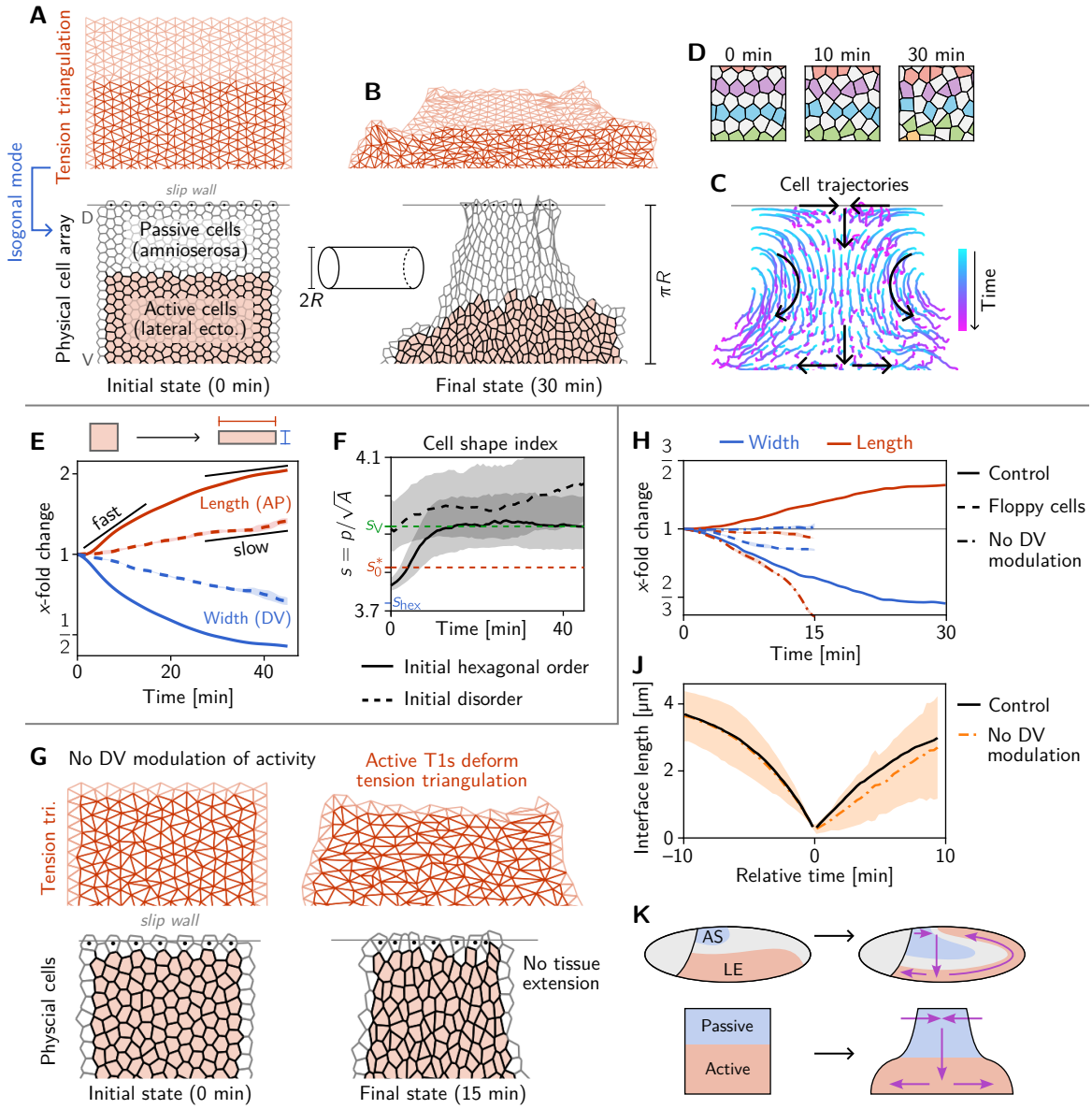

Figure 6: Tissue scale model reproduces observations and predicts dependence of tissue flow on cell-level order. A and B Tension triangulation (top) and the corresponding cell tessellation (bottom) from a numerical simulation combining active (shaded red) and passive cells. The simulation is performed on an unrolled cylinder geometry, with slip walls at the top and bottom boundary of the cell tessellation representing the cylinder's fixed circumference $2\pi R$. (Only half of the simulation domain, corresponding to one side of the embryo, is shown.) Tensions are initialized with a slight DV anisotropy (A). Positive tension feedback drives elongation via active T1s in the active tissue region, while the passive tissue yields passively (B); cf. Movie 4. **C** Trajectories of cell centroids showing the resulting tissue scale flow, resembling the characteristic flow pattern of GBE. **D** Magnified region showing coordinated active T1s (cf. Fig. 1C). **E** Net deformation of an active tissue patch with free boundaries, showing a significant slowdown after approximately two-fold elongation. **F** Starting from an initially ordered configuration with hexagonal cells, the cell-shape index calculated from cell area A and perimeter p rapidly converges to the value for a random Voronoi tessellation s_V. $s_0^* \approx 3.81$ is the critical shape index for the rigidity transition in the "classical" vertex model [55]. Lines show the median, shading indicates quartiles. **G** In a uniform active tissue with fixed "circumference" (via slip walls), convergent–extension of the tension triangulation by active T1s is compensated by isogonal cell elongation such that there is no net tissue elongation. **H** Lack of cell rigidity and lack of DV modulation of activity both completely abolish elongation of the active tissue region. (Simulations were stopped after 15 min because of numerical instability; see SI Sec. 2 for details). Control curves corresponds to the simulation shown in A and B. **J** The dynamics of interface length are nearly identical between simulations with and without DV modulation of activity. **K** Illustration of tissue flow on the ellipsoidal embryo (top) and in our simulation geometry on an unrolled cylinder (bottom). (AS: Amnioserosa; LE: Lateral Ectoderm.)

maintaining isotropic cell shapes. Notably, the cells acquire irregular shapes even though they are rigid (see Fig. 6E). Moreover, because isogonal modes are non-local as they always couple neighboring cells, cell rigidity implies tissue rigidity (see Fig. S15).

From the perspective of the so called "vertex model" [64, 65], a popular model for epithelial mechanics, irregular cell shapes despite cell shape rigidity might appear surprising. In the vertex model, cells have a preferred area A_0 and perimeter P_0. Depending on the ratio $s_0 = P_0/\sqrt{A_0}$, cells are either rigid ($s_0 < s_0^*$) or floppy ($s_0 > s_0^*$), where the critical value $s_0^* \approx 3.81$. Rigid cells assume regular (hexagonal) shapes, while floppy cells can assume a range of irregular shapes. In the rigid case, cells have to overcome an energy barrier to undergo T1 transitions [55]. The energy barrier vanishes in the fluid regime, where cell shapes are disordered ($s > s_0^*$). The observation of intercalations and disordered cell shapes in the lateral ectoderm has lead to the notion that the lateral ectoderm is undergoing a solid-to-fluid transition in order to extend [66]. However, as we showed above, active T1s can only drive tissue extension when the cell shapes are rigid, thus making the lateral ectoderm an active solid. The cell shape index above s_0^* does not indicate a vanishing shear modulus (i.e. "floppy cells") in this case. Instead, the irregular cell shapes we observe in experimental data and simulations are a consequence of disorder in the cortical tensions, which, in turn, results from active intercalations effectively "scrambling" the tension triangulation. In fact, the tension triangle distribution approaches a maximally disordered state, namely a random Delaunay distribution (cf. Fig. 5L and Fig. S9). Accordingly, a random Voronoi distribution reproduces the distribution of the shape index (see Fig. 6F and Fig. S13A').

New interfaces extend without additional active mechanisms

Next, we probed the importance of dorso-ventral (DV) patterning, i.e. the division of the tissue into active and passive regions. To that end, we simulated a tissue without DV modulation of activity, where all cells are active (Fig. 6G and Movie 6). Because the embryo circumference is fixed, the tissue cannot contract along the DV axis and, as a result of incompressibility, cannot extend along the AP axis (Fig. 6G, bottom). However, positive tension feedback still drives active T1s which manifest in the elongation of the tension triangulation (Fig. 6G, top). Because the tissue as a whole cannot deform, the intercalations are compensated by the isogonal mode. This forces cells into elongated shapes, which we predict to occur in a *toll[RM9]* mutant embryo, in which all cells adopt a ventro-lateral fate due to a mutation in the DV patterning pathway. The stretching of cells leads to a buildup of elastic energy (see Fig. S13C) In the actual embryo, some of this elastic energy is released by the formation of folds (buckling) [21] which our 2D simulations cannot describe.

Strikingly, we find that new interfaces still significantly elongate after neighbor exchanges in the simulation without DV modulation of activity (Fig. 6J), even tough there is no tissue extension. Interface elongation in the absence of tissue elongation has previously been observed in experiments where germ band extension has been blocked by cauterization near the posterior pole [29, 67]. We mimic the experiments of Ref. [29] by adding slip walls to the anterior and posterior boundary of the simulated tissue (Fig. S12) to block tissue extension. In this scenario, we also observe that newly formed interfaces extend, but at slightly slower rate than in WT. In agreement with experimental observations, we find that the orientation of extending interfaces is no longer biased along the AP axis when tissue extension is blocked (Fig. S12C). Since interface extension in our model is a purely passive process, we conclude that no active mechanisms – such as medial myosin pulses [29] – are necessary for the elongation of new interfaces. Instead, it results from the fundamental temporal asymmetry of the intercalation process, i.e. the low level of active tension on the new interface (cf. Fig. 4D).

In summary, our tissue scale model describes a tension triangulation driven by positive tension feedback and isogonal deformations governed by cell shape elas-

ticity. We reproduced key experimental observations, including the characteristic tissue scale flow pattern, the transition from fast to slow phase of GBE, generation of disordered cell shapes, and intercalations compensated by cell deformation in conditions where GBE is blocked. Thus, the model successfully bridges cell scale and tissue scale dynamics. Our model generated three main insights: (i) Cell rigidity is essential for active tissue elongation. (ii) Elongation of new interfaces can arise without the need of additional active mechanisms. (iii) Hexagonal order of the initial cell packing and tension anisotropy set up flow, and coherent, oriented T1s, which stops as order is lost through T1s, which destroy hexagons. Thus, the initial order determines total tissue extension.

Discussion

We have developed a novel perspective on tissue dynamics based on the underlying principle of force balance. Central to our approach is the balanced network of active forces generated and transmitted by cells. In epithelia, where contractility in the adherens-junctional cortex is the strongest source of stress, the force network takes the form of a triangulation in tension space [13] which fixes the angles at vertices in the tissue. Tissue deformations are driven by the adiabatic transformation of this force-balance geometry, allowing the epithelium to internally rearrange like a fluid, while supporting internal tension like a solid. Degrees of freedom that are unconstrained by the force-balance geometry account for passive tissue deformations that are controlled by external (non-local) forces and cell shape elasticity. Analysis of experimental data and mathematical modeling based on the this conceptual framework have allowed us develop a comprehensive understanding of epithelial tissue dynamics that bridges the cell and tissue scale and reveals how the final tissue shape is encoded in initial cell scale order and anisotropy. In the following, we discuss the implications of our findings.

Cortical tensions drive and constrain tissue deformations on the cellular scale

We have identified two mechanically distinct modes of tissue deformation: a cortical tension-driven mode and an isogonal (angle preserving) mode. The former represents active remodeling of interfaces, e.g. by myosin recruitment, and the latter cell deformations under the constraint of cortical force balance. When cortical tension is the strongest source of stresses in a tissue, the remaining stresses will mainly affect the isogonal mode. It therefore represents "bulk mechanics" (cell shape rigidity) and external stresses. The *tension–isogonal decomposition* quantifies the contributions of these two modes in experimental data based on cell geometry alone. This allows us to disentangle whether deformations are due to locally or non-locally generated forces, i.e. whether they are active or passive. The tension-isogonal decomposition is based on the same assumptions as tension inference which has been validated extensively [36, 37, 40, 44].

In the early *Drosophila* embryo, we observe both active and passive T1s. Generally, both modes – tension-driven and isogonal – contribute to tissue deformations at the same time. We have found that ventral furrow invagination isogonally stretches the lateral ectoderm which increases the tension threshold for active T1s there. We predict that the local relative tension threshold will be lower (namely $\sqrt{2}$) in mutants which lack a ventral furrow (*twist* and *snail*).

Our simulations also shed light on the long-standing puzzle of how interfaces extend after a neighbor exchange even though cortical myosin can only exert contractile forces. We show that no additional active mechanism is necessary. Our minimal model captures interface extension as a purely passive process and reproduces experimental observations (interface extension even if tissue extension is blocked, generation of irregular cell shapes) that were previously taken as evidence for ac-

tively driven interface extension [29, 68]. In our model, interface extension during both active and passive intercalations is driven by the tension on adjacent interfaces which exceeds the low active contractility of the new edge. The low myosin level on the emerging interface is predicted by a simple model for the myosin "handover" during a neighbor exchange.

The lateral ectoderm is an *active solid*

While tissue flow is often described as a viscoelastic fluid, we stress that internal tension balance and the capacity of an epithelium to sustain external stress distinguishes it from a fluid. Instead, we propose to view epithelia as "active solids" [13], which can support stress like regular solids, but have the capacity to internally remodel their structure on small (cellular) scales, while maintaining approximate force balance. Internal remodeling is then responsible for effective plasticity – i.e. the capacity to flow. Because the cortical tensions do not fix isogonal degrees of freedom, tissue rigidity requires cell-shape rigidity. When the cells are floppy (i.e. they do not resist shear forces), active intercalations are compensated by isogonal cell elongation such that there is no net tissue deformation. The *active solid* view of the tissue contrasts previous work suggesting that germ band is undergoing a solid-to-fluid transition in order to elongate [66]. This conclusion was based on the observation of irregular cell shapes. However, on our model, we find increasingly irregular cell shapes despite cell and tissue rigidity [68]. The increasing disorder is caused by active intercalations. We thus conclude that irregular cell shapes are not an indicator of tissue fluidization (in the sense of a vanishing shear modulus) in the presence of active T1s. In fact, as we discuss below, tissue flow slows dramatically as cell-scale order decreases.

Cells orchestrate tissue flow by navigating in tension space

Cells exert active stresses on each other and, at the same time, constantly sense the mechanical properties of their surroundings [69–71]. Thus, cells can communicate mechanically and we can think of cells as navigating not just in physical space but also in a more abstract "mechanical space". In an epithelium dominated by cortical tensions, this mechanical space is a tension space, linked to physical space via force balance. The angles in the cell tessellation are fixed by tensions which form a triangulation [13]). The tensions – and hence angles – are the geometric dials cells can directly sense and control.

We found that cells navigate tension space either via homeostasis (in the amnioserosa) or via positive tension feedback (lateral ectoderm). Mechanical homeostasis is found in various systems [72–74]. We hypothesize that tension homeostasis allows the amnioserosa to undergo large cell deformations while maintaining tissue integrity [73, 75]. Tension feedback, on the other hand, offers a clear avenue for cells to actively control shape. We have shown that T1 events are governed by a simple geometric criterion based on interface angles (i.e. the local tension configuration) and the local isogonal strain. Positive tension feedback drives the tensions towards this T1 threshold and thus drives active T1s. In contrast, passive T1s result when external forces drive the isogonal modes until a cell neighbor exchange occurs while tensions (and thus interface angles) remain constant.

T1s in the cell tessellation correspond to edge flips in the tension triangulation and are therefore a mechanism by which the dynamics in physical space feed back into the tension triangulation. Future work will address further such feedback mechanisms, for instance strain rate feedback [28]. They are essential to maintain the tissue in a quasi-stationary force balance [37].

Self-organization of active T1s through positive tension feedback

We have shown that self-organization by positive tension feedback provides a simple mechanism for active intercalations in the lateral ectoderm. Evidence for positive feedback is provided by the nonlinearly increasing inferred tension on contracting interfaces (Fig. 2D) and by laser ablation experiments in earlier work [26]. The underlying molecular mechanisms are yet to be identified and might rely on the catch-bond behavior of myosin [76, 77] or mechano-sensitive binding of α-catenin [78, 79].

Positive tension feedback amplifies a weak initial anisotropy of tension and turns initial hexagonal order into an alternating pattern of high and low tensions, manifested as LTC order, that is responsible for orchestrating T1 events across cells. This coordination is required during the fast phase of GBE where intercalations happen coherently (or "in parallel"). Our simulations have shown that a loss of LTC order causes T1s to become incoherent and therefore ineffective at driving tissue flow. This naturally explains the transition from the initial fast phase to the slow phase of GBE (see Fig. 1D and Fig. 6G), as intercalations create defects in the hexagonal cell packing (Fig. S10). The total tissue extension can be predicted from the initial degree hexagonal order and tension anisotropy. We predict that disrupting the hexagonal packing of nuclei prior to cellularization will cause slower GBE.

In other morphogenetic systems, e.g. the amniote primitive streak [10], flow is sustained for much longer, raising the question how coherent tissue flow is maintained. Long range gradients encoded by planar cell polarity could provide persistent anisotropy [80]. Positive tension feedback would then translate a weak large-scale anisotropy into the alternating tension pattern (bridges) required for T1s.

Our findings on the dynamics of interface length and tension during active T1s (Fig. 2D) are similar to another recently proposed model [49]. This model extends the classical "vertex model" with perimeter–area elasticity by active cortical contractility. Like in our model, active T1s are driven by a positive feedback loop of cortical tension. However, in contrast to our model, the model of Ref. [49] exhibits only a limited range of tissue deformation.

Genetic patterning and initial anisotropy

Because the Drosophila embryo is a closed surface, convergent–extension of the germ band must be compensated by an orthogonal deformation of the dorsal tissue, the amnioserosa (see Fig. 6K). In other words, the mechanical properties of the tissue must be modulated along the dorso-ventral axis: Positive tension feedback driving active rearrangements in the lateral ectoderm, and tension homeostasis in amnioserosa allowing it to yield to external forces while maintaining tissue integrity. When the genetic patterning responsible for this modulation is disrupted (as in a *toll[RM9]* mutant, where all cells take on a lateral, active fate), the germ band cannot converge and extend. Instead our model predicts that active T1s happen everywhere and are compensated by (isogonal) cell elongation along the DV axis. This highlights the importance of the DV-axis patterning. Recent work [28] has shown that mechanical feedback loops in the embryo are patterned along the DV axis. Notably, the DV patterning system is conserved across species [81]. Our work also highlights a second interaction between tissue flow and DV patterning: because the coherent T1s we observe and model do not scramble tissue stripes along the DV axis (Fig. 1A), distinct DV fates (e.g. neural and surface ectoderm) do not mix, a clear biological necessity.

In addition to the DV gradient, tension anisotropy along the DV axis is required to orient the GBE flow along the AP axis. This anisotropy might be due to mechanics (pulling of the ventral furrow [28] and hoop stresses resulting from ellipsoidal embryo geometry [82], since we observe anisotropy already prior to VF

formation), or indeed due to AP-striped genetic patterning [80, 83]. Thanks to the positive tension feedback, a weak initial anisotropy is sufficient to bias the direction of tissue elongation. This explains why *twist* and *snail* mutants, which have significantly reduced initial myosin anisotropy, still fully extend their germ band, albeit at a slower rate [28].

Our findings show how genetic patterning and self-organization are interconnected during GBE. Genetic patterning provides tissue scale input by demarcating distinct tissue regions with different mechanical properties. Self-organization via positive tension feedback orchestrates myosin contractility on the cellular scale and allows cells to coordinate their behaviors (such as active T1s) with their neighbors. As of yet, no mechanism has been found that produces cell scale coordination – as manifested, for instance, in the alternating pattern of high and low tensions (Fig. 2C) – from predetermined genetic patterns alone. Instead, the emerging overarching picture is that of morphogenesis driven by an interplay of bottom-up self-organization and top-down genetic patterning [9, 30].

Outlook

Going forward, we expect that geometric insight into tension space will provide a new perspective on many different systems [4], for example amniote primitive streak formation [10, 84], wing disk elongation [85, 86], the sea urchin archenteron [87], or kidney tubule elongation [88]. Further, it will be interesting to study intercalations driven by actin "protrusions" [89]: they too are governed by cortical force balance on the cellular level, making tension inference and the tension–isogonal decomposition applicable.

In future work, it might be also interesting to extend our minimal model to account for short-time scale phenomena, such as ratcheting, myosin pulses [29, 32, 68], and random myosin fluctuations [90], that transiently throw cells out of force balance and thus facilitate interface remodeling. Further, cells can also drive isogonal deformations actively, e.g. by apical myosin contractions [13, 19, 20]) and by and supracellular actin fibers [54, 91], which could be fruitfully incorporated into the tension–isogonal framework.

From a theoretical perspective, the tension–isogonal decomposition provides a new avenue to develop models for epithelial dynamics. For example, it will be interesting to ask how adiabatic force balance can be reconciled with existing models based on viscous dissipation [11, 92]. In this work, we have presented a "discrete" model that operates on a tension triangulation as its central entity. Going forward, we expect that this will inspire new continuum models which coarse grain cell-level details but explicitly account for the geometry of tension space and isogonal degrees of freedom.

Acknowledgements. We thank Matthew Lefebvre, Noah Mitchell, Sebastian Streichan, and Arthur Hernandez for stimulating discussions and careful reading of the manuscript. FB acknowledges support of the GBMF post-doctoral fellowship (GBMF award #2919). NHC was supported by NIGMS R35-GM138203 and NSF PHY:1707973. BIS acknowledges support via NSF PHY:1707973 and NSF PHY:2210612.

References

[1] Mao, Y. *et al.* Planar polarization of the atypical myosin Dachs orients cell divisions in *Drosophila*. *Genes & Development* **25**, 131–136 (2011). URL http://genesdev.cshlp.org/lookup/doi/10.1101/gad.610511.

[2] Gillies, T. E. & Cabernard, C. Cell Division Orientation in Animals. *Current Biology* **21**, R599–R609 (2011). URL https://linkinghub.elsevier.com/retrieve/pii/S0960982211007287.

[3] Tada, M. & Heisenberg, C.-P. Convergent extension: Using collective cell migration and cell intercalation to shape embryos. *Development* **139**, 3897–3904 (2012). URL https://journals.biologists.com/dev/article/139/21/3897/45339/Convergent-extension-using-collective-cell.

[4] Shindo, A. Models of convergent extension during morphogenesis. *WIREs Developmental Biology* **7** (2018). URL https://onlinelibrary.wiley.com/doi/10.1002/wdev.293.

[5] Sutherland, A., Keller, R. & Lesko, A. Convergent extension in mammalian morphogenesis. *Seminars in Cell & Developmental Biology* **100**, 199–211 (2020). URL https://linkinghub.elsevier.com/retrieve/pii/S1084952119300503.

[6] Huebner, R. J. & Wallingford, J. B. Coming to Consensus: A Unifying Model Emerges for Convergent Extension. *Developmental Cell* **46**, 389–396 (2018). URL https://linkinghub.elsevier.com/retrieve/pii/S1534580718306397.

[7] Oster, G. F., Murray, J. D. & Harris, A. K. Mechanical aspects of mesenchymal morphogenesis. *Development* **78**, 83–125 (1983). URL https://journals.biologists.com/dev/article/78/1/83/51263/Mechanical-aspects-of-mesenchymal-morphogenesis.

[8] Shyer, A. E. *et al.* Emergent cellular self-organization and mechanosensation initiate follicle pattern in the avian skin. *Science* **357**, 811–815 (2017). URL https://www.science.org/doi/10.1126/science.aai7868.

[9] Caldarelli, P., Chamolly, A., Alegria-Prévot, O., Gros, J. & Corson, F. Self-organized tissue mechanics underlie embryonic regulation (2021). URL http://biorxiv.org/lookup/doi/10.1101/2021.10.08.463661.

[10] Saadaoui, M., Rocancourt, D., Roussel, J., Corson, F. & Gros, J. A tensile ring drives tissue flows to shape the gastrulating amniote embryo. *Science* **367**, 453–458 (2020). URL https://www.science.org/doi/10.1126/science.aaw1965.

[11] Streichan, S. J., Lefebvre, M. F., Noll, N., Wieschaus, E. F. & Shraiman, B. I. Global morphogenetic flow is accurately predicted by the spatial distribution of myosin motors. *eLife* **7**, e27454 (2018). URL https://elifesciences.org/articles/27454.

[12] Ma, X., Lynch, H. E., Scully, P. C. & Hutson, M. S. Probing embryonic tissue mechanics with laser hole drilling. *Physical Biology* **6**, 036004 (2009). URL https://iopscience.iop.org/article/10.1088/1478-3975/6/3/036004.

[13] Noll, N., Mani, M., Heemskerk, I., Streichan, S. J. & Shraiman, B. I. Active tension network model suggests an exotic mechanical state realized in epithelial tissues. *Nature Physics* **13**, 1221–1226 (2017). URL https://www.nature.com/articles/nphys4219.

[14] Hales, K. G., Korey, C. A., Larracuente, A. M. & Roberts, D. M. Genetics on the Fly: A Primer on the *Drosophila* Model System. *Genetics* **201**, 815–842 (2015). URL https://academic.oup.com/genetics/article/201/3/815/5930114.

[15] Krzic, U., Gunther, S., Saunders, T. E., Streichan, S. J. & Hufnagel, L. Multiview light-sheet microscope for rapid in toto imaging. *Nature Methods* **9**, 730–733 (2012). URL http://www.nature.com/articles/nmeth.2064.

[16] Stern, T., Shvartsman, S. Y. & Wieschaus, E. F. Deconstructing gastrulation at single-cell resolution. *Current Biology* **32**, 1861–1868.e7 (2022). URL https://linkinghub.elsevier.com/retrieve/pii/S0960982222003293.

[17] Gilbert, S. F. & Barresi, M. J. F. *Developmental Biology* (Sinauer Associates, Sunderland, Massachusetts, 2016).

[18] Leptin, M. Drosophila Gastrulation: From Pattern Formation to Morphogenesis. *Annual Review of Cell and Developmental Biology* **11**, 189–212 (1995). URL https://www.annualreviews.org/doi/10.1146/annurev.cb.11.110195.001201.

[19] Martin, A. C., Kaschube, M. & Wieschaus, E. F. Pulsed contractions of an actin–myosin network drive apical constriction. *Nature* **457**, 495–499 (2009). URL http://dx.doi.org/10.1038/nature07522.

[20] Martin, A. C. The Physical Mechanisms of Drosophila Gastrulation: Mesoderm and Endoderm Invagination. *Genetics* **214**, 543–560 (2020). URL http://www.genetics.org/lookup/doi/10.1534/genetics.119.301292.

[21] Irvine, K. & Wieschaus, E. Cell intercalation during Drosophila germband extension and its regulation by pair-rule segmentation genes. *Development* **120**, 827–841 (1994). URL https://journals.biologists.com/dev/article/120/4/827/38309/Cell-intercalation-during-Drosophila-germband.

[22] Zallen, J. A. & Wieschaus, E. F. Patterned Gene Expression Directs Bipolar Planar Polarity in Drosophila. *Developmental Cell* **6**, 343–355 (2004).

[23] Bertet, C., Sulak, L. & Lecuit, T. Myosin-dependent junction remodelling controls planar cell intercalation and axis elongation. *Nature* **429**, 667–671 (2004). URL http://www.nature.com/articles/nature02581.

[24] Blanchard, G. B. *et al.* Tissue tectonics: Morphogenetic strain rates, cell shape change and intercalation. *Nature Methods* **6**, 458–464 (2009). URL http://www.nature.com/articles/nmeth.1327.

[25] Lecuit, T., Lenne, P.-F. & Munro, E. Force Generation, Transmission, and Integration during Cell and Tissue Morphogenesis. *Annual Review of Cell and Developmental Biology* **27**, 157–184 (2011). URL https://www.annualreviews.org/doi/10.1146/annurev-cellbio-100109-104027.

[26] Blankenship, J. T., Backovic, S. T., Sanny, J. S., Weitz, O. & Zallen, J. A. Multicellular Rosette Formation Links Planar Cell Polarity to Tissue Morphogenesis. *Developmental Cell* **11**, 459–470 (2006). URL https://linkinghub.elsevier.com/retrieve/pii/S153458070600400X.

[27] Fernandez-Gonzalez, R., Simoes, S. d. M., Röper, J.-C., Eaton, S. & Zallen, J. A. Myosin II Dynamics Are Regulated by Tension in Intercalating Cells. *Developmental Cell* **17**, 736–743 (2009). URL http://www.nature.com/articles/s41556-020-0524-x.

[28] Gustafson, H. J., Claussen, N., De Renzis, S. & Streichan, S. J. Patterned mechanical feedback establishes a global myosin gradient. *bioRxiv* doi:10.1101/2021.12.06.471321 (2021). URL http://biorxiv.org/lookup/doi/10.1101/2021.12.06.471321.

[29] Collinet, C., Rauzi, M., Lenne, P.-F. & Lecuit, T. Local and tissue-scale forces drive oriented junction growth during tissue extension. *Nature Cell Biology* **17**, 1247–1258 (2015). URL http://www.nature.com/articles/ncb3226.

[30] Bailles, A. *et al.* Genetic induction and mechanochemical propagation of a morphogenetic wave. *Nature* **572**, 467–473 (2019). URL http://www.nature.com/articles/s41586-019-1492-9.

[31] Rauzi, M. Cell intercalation in a simple epithelium. *Philosophical Transactions of the Royal Society B: Biological Sciences* **375**, 20190552 (2020). URL https://royalsocietypublishing.org/doi/10.1098/rstb.2019.0552.

[32] Vanderleest, T. E. *et al.* Vertex sliding drives intercalation by radial coupling of adhesion and actomyosin networks during Drosophila germband extension. *eLife* **7**, e34586 (2018). URL https://elifesciences.org/articles/34586.

[33] Heemskerk, I. & Streichan, S. J. Tissue cartography: Compressing bio-image data by dimensional reduction. *Nature Methods* **12**, 1139–1142 (2015). URL http://www.nature.com/articles/nmeth.3648.

[34] Baum, B. & Georgiou, M. Dynamics of adherens junctions in epithelial establishment, maintenance, and remodeling. *Journal of Cell Biology* **192**, 907–917 (2011). URL https://rupress.org/jcb/article/192/6/907/36223/Dynamics-of-adherens-junctions-in-epithelial.

[35] Chiou, K. K., Hufnagel, L. & Shraiman, B. I. Mechanical Stress Inference for Two Dimensional Cell Arrays. *PLoS Computational Biology* **8**, e1002512 (2012). URL https://dx.plos.org/10.1371/journal.pcbi.1002512.

[36] Ishihara, S. *et al.* Comparative study of non-invasive force and stress inference methods in tissue. *The European Physical Journal E* **36**, 45 (2013). URL http://link.springer.com/10.1140/epje/i2013-13045-8.

[37] Noll, N., Streichan, S. J. & Shraiman, B. I. Variational Method for Image-Based Inference of Internal Stress in Epithelial Tissues. *Physical Review X* **10**, 011072 (2020). URL https://link.aps.org/doi/10.1103/PhysRevX.10.011072.

[38] Bambardekar, K., Clément, R., Blanc, O., Chardès, C. & Lenne, P.-F. Direct laser manipulation reveals the mechanics of cell contacts in vivo. *Proceedings of the National Academy of Sciences* **112**, 1416–1421 (2015). URL https://pnas.org/doi/full/10.1073/pnas.1418732112.

[39] Munjal, A., Philippe, J.-M., Munro, E. & Lecuit, T. A self-organized biomechanical network drives shape changes during tissue morphogenesis. *Nature* **524**, 351–355 (2015). URL https://elifesciences.org/articles/10757.

[40] Cheikh, M. I. *et al.* A comprehensive model of Drosophila epithelium reveals the role of embryo geometry and cell topology in mechanical responses (2022). URL http://biorxiv.org/lookup/doi/10.1101/2022.08.12.503803.

[41] Lecuit, T. & Yap, A. S. E-cadherin junctions as active mechanical integrators in tissue dynamics. *Nature Publishing Group* **17**, 533–539 (2015). URL http://dx.doi.org/10.1038/ncb3136.

[42] Prost, J., Jülicher, F. & Joanny, J.-F. Active gel physics. *Nature Physics* **11**, 111–117 (2015). URL http://www.nature.com/articles/nphys3224.

[43] Doubrovinski, K., Swan, M., Polyakov, O. & Wieschaus, E. F. Measurement of cortical elasticity in *Drosophila melanogaster* embryos using ferrofluids. *Proceedings of the National Academy of Sciences* **114**, 1051–1056 (2017). URL https://pnas.org/doi/full/10.1073/pnas.1616659114.

[44] Kong, W. *et al.* Experimental validation of force inference in epithelia from cell to tissue scale. *Scientific Reports* **9**, 14647 (2019). URL https://www.nature.com/articles/s41598-019-50690-3.

[45] Maxwell, J. C. On reciprocal figures and diagrams of forces. *The London, Edinburgh, and Dublin Philosophical Magazine and Journal of Science* **27**, 250–261 (1864). URL https://www.tandfonline.com/doi/full/10.1080/14786446408643663.

[46] Varignon, P. *Nouvelle Mécanique Ou Statique, Dont Le Projet Fut Donné En 1687: Ouvrage Posthume* (chez Claude Jombert, 1725). URL https://books.google.com/books?id=o-lWAAAAcAAJ.

[47] Tighe, B. P., van Eerd, A. R. T. & Vlugt, T. J. H. Entropy Maximization in the Force Network Ensemble for Granular Solids. *Physical Review Letters* **100**, 238001 (2008). URL https://link.aps.org/doi/10.1103/PhysRevLett.100.238001.

[48] Stern, T., Shvartsman, S. Y. & Wieschaus, E. F. Template-based mapping of dynamic motifs in tissue morphogenesis. *PLOS Computational Biology* **16**, e1008049 (2020). URL https://dx.plos.org/10.1371/journal.pcbi.1008049.

[49] Sknepnek, R., Djafer-Cherif, I., Chuai, M., Weijer, C. & Henkes, S. Generating active T1 transitions through mechanochemical feedback. *eLife* **12**, e79862 (2023). URL https://elifesciences.org/articles/79862.

[50] Ramms, L. *et al.* Keratins as the main component for the mechanical integrity of keratinocytes. *Proceedings of the National Academy of Sciences* **110**, 18513–18518 (2013). URL https://pnas.org/doi/full/10.1073/pnas.1313491110.

[51] Charrier, E. E. *et al.* The desmin network is a determinant of the cytoplasmic stiffness of myoblasts: Desmin network: A determinant of the cytoplasmic stiffness of myoblasts. *Biology of the Cell* **110**, 77–90 (2018). URL https://onlinelibrary.wiley.com/doi/10.1111/boc.201700040.

[52] Merkel, M. *et al.* Triangles bridge the scales: Quantifying cellular contributions to tissue deformation. *Physical Review E* **95**, 032401 (2017). URL https://link.aps.org/doi/10.1103/PhysRevE.95.032401.

[53] Bocanegra-Moreno, L., Singh, A., Hannezo, E., Zagorski, M. & Kicheva, A. Cell cycle dynamics control fluidity of the developing mouse neuroepithelium. *Nature Physics* (2023). URL https://www.nature.com/articles/s41567-023-01977-w.

[54] Priess, J. R. & Hirsh, D. I. Caenorhabditis elegans morphogenesis: The role of the cytoskeleton in elongation of the embryo. *Developmental Biology* **117**, 156–173 (1986). URL https://linkinghub.elsevier.com/retrieve/pii/0012160686903581.

[55] Bi, D., Lopez, J. H., Schwarz, J. M. & Manning, M. L. A density-independent rigidity transition in biological tissues. *Nature Physics* **11**, 1074–1079 (2015). URL http://www.nature.com/articles/nphys3471.

[56] Rauzi, M., Verant, P., Lecuit, T. & Lenne, P.-F. Nature and anisotropy of cortical forces orienting Drosophila tissue morphogenesis. *Nature Cell Biology* **10**, 1401–1410 (2008). URL http://www.nature.com/articles/ncb1798.

[57] Kale, G. R. *et al.* Distinct contributions of tensile and shear stress on E-cadherin levels during morphogenesis. *Nature Communications* **9**, 5021 (2018). URL https://www.nature.com/articles/s41467-018-07448-8.

[58] Etournay, R. *et al.* Interplay of cell dynamics and epithelial tension during morphogenesis of the Drosophila pupal wing. *eLife* **4**, e07090 (2015). URL https://elifesciences.org/articles/07090.

[59] Lau, K. *et al.* Anisotropic stress orients remodelling of mammalian limb bud ectoderm. *Nature Cell Biology* **17**, 569–579 (2015). URL https://www.nature.com/articles/ncb3156.

[60] Harding, M. J., McGraw, H. F. & Nechiporuk, A. The roles and regulation of multicellular rosette structures during morphogenesis. *Development* **141**, 2549–2558 (2014). URL https://journals.biologists.com/dev/article/141/13/2549/46279/The-roles-and-regulation-of-multicellular-rosette.

[61] Rauzi, M. *et al.* Embryo-scale tissue mechanics during Drosophila gastrulation movements. *Nature Communications* **6**, 8677 (2015). URL https://www.nature.com/articles/ncomms9677.

[62] He, B., Martin, A. & Wieschaus, E. Flow-dependent myosin recruitment during *Drosophila* cellularization requires zygotic *dunk* activity. *Development* dev.131334 (2016). URL https://journals.biologists.com/dev/article/doi/10.1242/dev.131334/264083/Flow-dependent-myosin-recruitment-during.

[63] Dutta, S., Djabrayan, N. J.-V., Torquato, S., Shvartsman, S. Y. & Krajnc, M. Self-Similar Dynamics of Nuclear Packing in the Early Drosophila Embryo. *Biophysical Journal* **117**, 743–750 (2019). URL https://linkinghub.elsevier.com/retrieve/pii/S000634951930565X.

[64] Nagai, T. & Honda, H. A dynamic cell model for the formation of epithelial tissues. *Philosophical Magazine B* **81**, 699–719 (2001). URL https://www.tandfonline.com/doi/full/10.1080/13642810108205772.

[65] Alt, S., Ganguly, P. & Salbreux, G. Vertex models: From cell mechanics to tissue morphogenesis. *Philosophical Transactions of the Royal Society B: Biological Sciences* **372**, 20150520 (2017). URL https://royalsocietypublishing.org/doi/10.1098/rstb.2015.0520.

[66] Wang, X. *et al.* Anisotropy links cell shapes to tissue flow during convergent extension. *Proceedings of the National Academy of Sciences* **117**, 13541–13551 (2020). URL https://pnas.org/doi/full/10.1073/pnas.1916418117.

[67] Rauzi, M. Probing tissue interaction with laser-based cauterization in the early developing Drosophila embryo. In *Methods in Cell Biology*, vol. 139, 153–165 (Elsevier, 2017). URL https://linkinghub.elsevier.com/retrieve/pii/S0091679X16301558.

[68] Vanderleest, T. E., Xie, Y., Smits, C., Blankenship, J. T. & Loerke, D. Interface extension is a continuum property suggesting a linkage between AP contractile and DV lengthening processes. *Molecular Biology of the Cell* **33**, ar142 (2022). URL https://www.molbiolcell.org/doi/10.1091/mbc.E21-07-0352.

[69] Heisenberg, C.-P. & Bellaïche, Y. Forces in Tissue Morphogenesis and Patterning. *Cell* **153**, 948–962 (2013). URL https://linkinghub.elsevier.com/retrieve/pii/S0092867413005734.

[70] Collinet, C. & Lecuit, T. Programmed and self-organized flow of information during morphogenesis. *Nature Reviews Molecular Cell Biology* **22**, 245–265 (2021). URL http://www.nature.com/articles/s41580-020-00318-6.

[71] Pinheiro, D. & Bellaïche, Y. Mechanical Force-Driven Adherens Junction Remodeling and Epithelial Dynamics. *Developmental Cell* **47**, 3–19 (2018). URL https://linkinghub.elsevier.com/retrieve/pii/S1534580718307433.

[72] Humphrey, J. D. Vascular Adaptation and Mechanical Homeostasis at Tissue, Cellular, and Sub-cellular Levels. *Cell Biochemistry and Biophysics* **50**, 53–78 (2008). URL http://link.springer.com/10.1007/s12013-007-9002-3.

[73] Latorre, E. *et al.* Active superelasticity in three-dimensional epithelia of controlled shape. *Nature* **563**, 203–208 (2018). URL http://www.nature.com/articles/s41586-018-0671-4.

[74] Stamenović, D. & Smith, M. L. Tensional homeostasis at different length scales. *Soft Matter* **16**, 6946–6963 (2020). URL http://xlink.rsc.org/?DOI=D0SM00763C.

[75] Jodoin, J. N. *et al.* Stable Force Balance between Epithelial Cells Arises from F-Actin Turnover. *Developmental Cell* **35**, 685–697 (2015). URL https://linkinghub.elsevier.com/retrieve/pii/S1534580715007534.

[76] Veigel, C., Molloy, J. E., Schmitz, S. & Kendrick-Jones, J. Load-dependent kinetics of force production by smooth muscle myosin measured with optical tweezers. *Nature Cell Biology* **5**, 980–986 (2003). URL http://www.nature.com/articles/ncb1060.

[77] Laakso, J. M., Lewis, J. H., Shuman, H. & Ostap, E. M. Myosin I Can Act As a Molecular Force Sensor. *Science* **321**, 133–136 (2008). URL https://www.science.org/doi/10.1126/science.1159419.

[78] Barry, A. K. *et al.* α-Catenin cytomechanics – role in cadherin-dependent adhesion and mechanotransduction. *Journal of Cell Science* **127**, 1779–1791 (2014). URL https://journals.biologists.com/jcs/article/127/8/1779/54962/Catenin-cytomechanics-role-in-cadherin-dependent.

[79] Mei, L. *et al.* Molecular mechanism for direct actin force-sensing by α-catenin. *eLife* **9**, e62514 (2020). URL https://elifesciences.org/articles/62514.

[80] Butler, M. T. & Wallingford, J. B. Planar cell polarity in development and disease. *Nature Reviews Molecular Cell Biology* **18**, 375–388 (2017). URL http://www.nature.com/articles/nrm.2017.11.

[81] Holley, S. A. & Ferguson, E. L. Fish are like flies are like frogs: Conservation of dorsal-ventral patterning mechanisms. *BioEssays* **19**, 281–284 (1997). URL https://onlinelibrary.wiley.com/doi/10.1002/bies.950190404.

[82] Lefebvre, M. F., Claussen, N. H., Mitchell, N. P., Gustafson, H. J. & Streichan, S. J. Geometric control of myosin II orientation during axis elongation. *eLife* **12**, e78787 (2023). URL https://elifesciences.org/articles/78787.

[83] Lavalou, J. *et al.* Formation of polarized contractile interfaces by self-organized Toll-8/Cirl GPCR asymmetry. *Developmental Cell* **56**, 1574–1588.e7 (2021). URL https://linkinghub.elsevier.com/retrieve/pii/S1534580721002707.

[84] Rozbicki, E. *et al.* Myosin-II-mediated cell shape changes and cell intercalation contribute to primitive streak formation. *Nature Cell Biology* **17**, 397–408 (2015). URL http://www.nature.com/articles/ncb3138.

[85] Dye, N. A. *et al.* Cell dynamics underlying oriented growth of the *Drosophila* wing imaginal disc. *Development* dev.155069 (2017). URL https://journals.biologists.com/dev/article/doi/10.1242/dev.155069/264392/Cell-dynamics-underlying-oriented-growth-of-the.

[86] Dye, N. A. *et al.* Self-organized patterning of cell morphology via mechanosensitive feedback. *eLife* **10**, e57964 (2021). URL https://elifesciences.org/articles/57964.

[87] Hardin, J. & Weliky, M. Cell rearrangement induced by filopodial tension accounts for the late phase of convergent extension in the sea urchin archenteron. *Molecular Biology of the Cell* **30**, 1911–1919 (2019). URL https://www.molbiolcell.org/doi/10.1091/mbc.E19-03-0143.

[88] Lienkamp, S. S. *et al.* Vertebrate kidney tubules elongate using a planar cell polarity–dependent, rosette-based mechanism of convergent extension. *Nature Genetics* **44**, 1382–1387 (2012). URL http://www.nature.com/articles/ng.2452.

[89] Weng, S., Huebner, R. J. & Wallingford, J. B. Convergent extension requires adhesion-dependent biomechanical integration of cell crawling and junction contraction. *Cell Reports* **39**, 110666 (2022). URL https://linkinghub.elsevier.com/retrieve/pii/S2211124722004181.

[90] Curran, S. *et al.* Myosin II Controls Junction Fluctuations to Guide Epithelial Tissue Ordering. *Developmental Cell* **43**, 480–492.e6 (2017). URL https://linkinghub.elsevier.com/retrieve/pii/S1534580717307712.

[91] Aufschnaiter, R., Wedlich-Söldner, R., Zhang, X. & Hobmayer, B. Apical and basal epitheliomuscular F-actin dynamics during *Hydra* bud evagination. *Biology Open* **8**, bio.022723 (2017). URL https://journals.biologists.com/bio/article/doi/10.1242/bio.022723/256616/Apical-and-basal-epitheliomuscular-F-actin.

[92] Serra, M. *et al.* A mechanochemical model recapitulates distinct vertebrate gastrulation modes (2021). URL http://biorxiv.org/lookup/doi/10.1101/2021.10.03.462928. 10.1101/2021.10.03.462928.

[93] Guirao, B. *et al.* Unified quantitative characterization of epithelial tissue development. *eLife* **4**, e08519 (2015). URL https://elifesciences.org/articles/08519.

[94] Efrati, E., Sharon, E. & Kupferman, R. Elastic theory of unconstrained non-Euclidean plates. *Journal of the Mechanics and Physics of Solids* **57**, 762–775 (2009). URL https://linkinghub.elsevier.com/retrieve/pii/S0022509608002160.

[95] Ginibre, J. Statistical Ensembles of Complex, Quaternion, and Real Matrices. *Journal of Mathematical Physics* **6**, 440–449 (1965). URL http://aip.scitation.org/doi/10.1063/1.1704292.

[96] Feder, J. Random sequential adsorption. *Journal of Theoretical Biology* **87**, 237–254 (1980). URL https://linkinghub.elsevier.com/retrieve/pii/0022519380903586.

[97] Halperin, B. I. & Nelson, D. R. Theory of Two-Dimensional Melting. *Physical Review Letters* **41**, 121–124 (1978). URL https://link.aps.org/doi/10.1103/PhysRevLett.41.121.

[98] Armengol-Collado, J.-M., Carenza, L. N., Eckert, J., Krommydas, D. & Giomi, L. Epithelia are multiscale active liquid crystals (2022). URL http://arxiv.org/abs/2202.00668. 2202.00668.

[99] Virtanen et al., P. SciPy 1.0: Fundamental algorithms for scientific computing in Python. *Nature Methods* **17**, 261–272 (2020). URL http://www.nature.com/articles/s41592-019-0686-2.

[100] Marschner, S. & Shirley, P. *Fundamentals of Computer Graphics* (A K Peters/CRC Press, 2018), 4th edition edn.

[101] Bradbury, J. *et al.* JAX: Composable transformations of Python+NumPy programs (2018). URL http://github.com/google/jax.

Supplementary Material

1 Analysis of experimental data

1.1 Data source

Whole embryo cell segmentation and tracking data was obtained from the repository DOI:10.6084/m9.figshare.18551420.v3 deposited with Ref. [16]. We analyzed the dataset with id number 1620 since it had the highest time resolution (15 s) and covered the longest time period (50 min), starting ca. 7 min before the onset of ventral furrow invagination.

1.2 Tissue tectonics analysis

Based on segmented and tracked cells, the tissue strain rate and cell deformation rate can be calculated via the methods described in Ref. [24]; see also [93] and [52]. In brief, the local tissue strain rate is calculated from the centroid positions $\mathbf{c}_i$ of the cells in a small neighborhood N of a cell (we use nearest neighbors). One looks for a linear transformation that maps the positions of the cell centroids at one timepoint to those at the next one. Because the resulting equations are overdetermined, an approximate solution minimizing the error is obtained using the least-squares algorithm. The linear transformation is then further decomposed into a symmetric part, describing local shear and area changes, and an antisymmetric part, describing the tissue rotation. Because the Drosophila ectoderm is a surface in three dimensional space, we need to calculate these quantities in the local tangent plane. The cell deformation rate is calculated from the rate of change of the cell's moment of inertia tensor in the frame that co-rotates with the tissue.

Figure S1A–B' show the tissue and cell deformation rates during VF invagination (A and A') and during GBE (B and B'). Figure S1C shows the cell elongation as measured by the Beltrami coefficient $\mu = |a - b|/(a + b)$, where a and b are the half-axes of a best-fit ellipse to the cell.

Local tangent plane and coordinate frames. The analysis of local tissue geometry (including tissue tectonics, tension inference, and tension–isogonal decomposition) is performed in the local tangent plane. The local tangent plane is determined by the local normal vector $\mathbf{n}$ which we find by a singular value decomposition of the point set of interest (vertex coordinates for a single cell, cell centroids for a patch of cells). The normal vector is read-off as the basis vector corresponding to the smallest singular value.

Depending on the context, we use three different coordinate bases within the tangent plane: (i) The "Eulerian" (or "lab frame") basis formed by the azimuthal vector $\mathbf{e}^{\mathrm{E}}_{\mathrm{DV}}$ along the DV axis and its orthogonal complement $\mathbf{e}^{\mathrm{E}}_{\mathrm{AP}} = \mathbf{n} \times \mathbf{e}^{\mathrm{E}}_{\mathrm{DV}}$, along the AP axis. The Eulerian frame is used to plot orientation and strain fields in the flat map projections ("pullbacks") of the tissue (e.g. Fig. 3D and Fig. 5B). (ii) A "Lagrangian" (or "tissue frame") basis which co-rotates with the tissue is used to quantify the DV component of the isogonal deformation tensor (Fig. 3E). This co-rotating frame is defined by tracking a patch of cells and fitting a linear transformation $A(t)$ to the displacement of cell centroids relative to the patch's center of mass. The linear transformation is constrained to transform the initial into the final normal vector $A.\mathbf{n}(0) = \mathbf{n}(t)$. A polar decomposition $A(t) = S(t).R(t)$ then yields the local rotation matrix $R(t)$ for the tissue patch. The co-rotated basis vectors are obtained by applying R to the Eulerian basis vectors at time zero: $\mathbf{e}^{\mathrm{L}}_{\mathrm{i}}(t) = R(t).\mathbf{e}^{\mathrm{E}}_{i}(0)$. (iii) For the tension–isogonal decomposition of intercalating cell quartets (Fig. 3C and C' and Fig. S6), we define a co-moving orthogonal basis based on the cell centroids: The basis vectors are defined as the pair of orthogonal vectors that best fit the displacement vectors that connect opposite cells in the quartet. Before the neighbor exchange, the first basis vector is aligned with the

two cells that touch and the second basis vector is aligned with the cells that don't touch. After the neighbor exchange, the roles are flipped. This ensures that the basis vectors vary smoothly through the neighbor exchange.

1.3 Identification and classification of intercalation events

Cell interface collapse and emergence events can be identified by tracking cell contacts. We start by identifying all pairs of cells that share a interface at some timepoint. For each pair, one can then identify the time periods where the cells are in contact. This allows one to identify interface collapse and emergence events. We exclude cases where a cell pair loses contact because one of the cells invaginates or divides and cases where cells come into contact because cells in between them invaginate.

Some cell pairs transiently lose or gain contact. For the interface collapse rate shown in Fig. 1E, we only account for the first collapse event for cell pairs that are not in contact at the last frame, i.e. for those that *permanently* lose contact. Similarly, for interface emergence events, we only account for the last event where a pair of cells not in contact at the first frame comes into contact.

Spatial distribution of interface collapses. From the tracked interface collapses, we can count the number of interface collapses that each cell is involved in, giving us a spatially resolved map of intercalations (Fig. S1D). In the lateral ectoderm (regions 4–8 in Fig. S3A), we find 2.58 interface collapses per cell. From this, we can estimate the total tissue extension by cell rearrangements. In a hexagonal lattice, synchronous T1s cause two interface collapses per cell and elongate the tissue by a factor $\sqrt{3}$, assuming that the cells do not elongate. (The tissue also contracts by a factor $1/\sqrt{3}$ along the orthogonal axis.) For 2.58 interface collapses per cell, therefore cause tissue elongation by a factor $(2.58/2) \times \sqrt{3} \approx 2.23$, in good agreement with the total elongation of the germ band (cf. Fig. 1D).

In contrast to the lateral ectoderm where cells don't elongate coherently, cell elongation contributes significantly to tissue deformation near the dorsal pole (see Fig. S1C). This is a generic feature of passive T1s driven by isogonal deformations (see Fig. S6D).

Orientation of collapsing interfaces. The convergent–extension flows in the lateral ectoderm and near the dorsal pole (amnioserosa) are oriented perpendicular to each other (see Fig. S1). We therefore also expect perpendicular orientation of the collapsing interfaces in these two regions. We quantify interface orientation of collapsing edges at the blastoderm stage (i.e. before the onset of tissue flow, $t = 0\,\mathrm{min}$) as shown in Fig. S2A and C. In the ectoderm, interfaces that collapse before $t = 42\,\mathrm{min}$, i.e. within the first ca. 15 min of GBE are predominantly DV oriented at $t = 0\,\mathrm{min}$ (see Fig. S2B). By contrast, interfaces near the dorsal pole predominantly oriented along AP. The orientation of interfaces in the lateral ectoderm that collapse after $t = 42\,\mathrm{min}$ is initially not strongly biased along the DV axis Fig. S2C and D. However, during GBE, these interfaces progressively align with the DV co-rotated DV axis before they eventually start contracting (see Fig. S2C' and D; the coordinate frame co-rotating with the tissue is described in Sec. 1.2).

Tracking quartets and identifying rosettes. The above procedure for identifying intercalation events is very fast and easy to implement. However, it does not distinguish between T1s and higher order intercalation events (rosettes). Moreover, it cannot easily be determined which interface collapse corresponds to which interface emergence.

We therefore implemented an alternative algorithm to identify intercalations, by tracking quartets of cells. This is possible by identifying cycles of length four in the neighborhood graph of the cell tessellation at each time point. We exclude cases where the four cells surround one or more cells that are not part of the cycle and

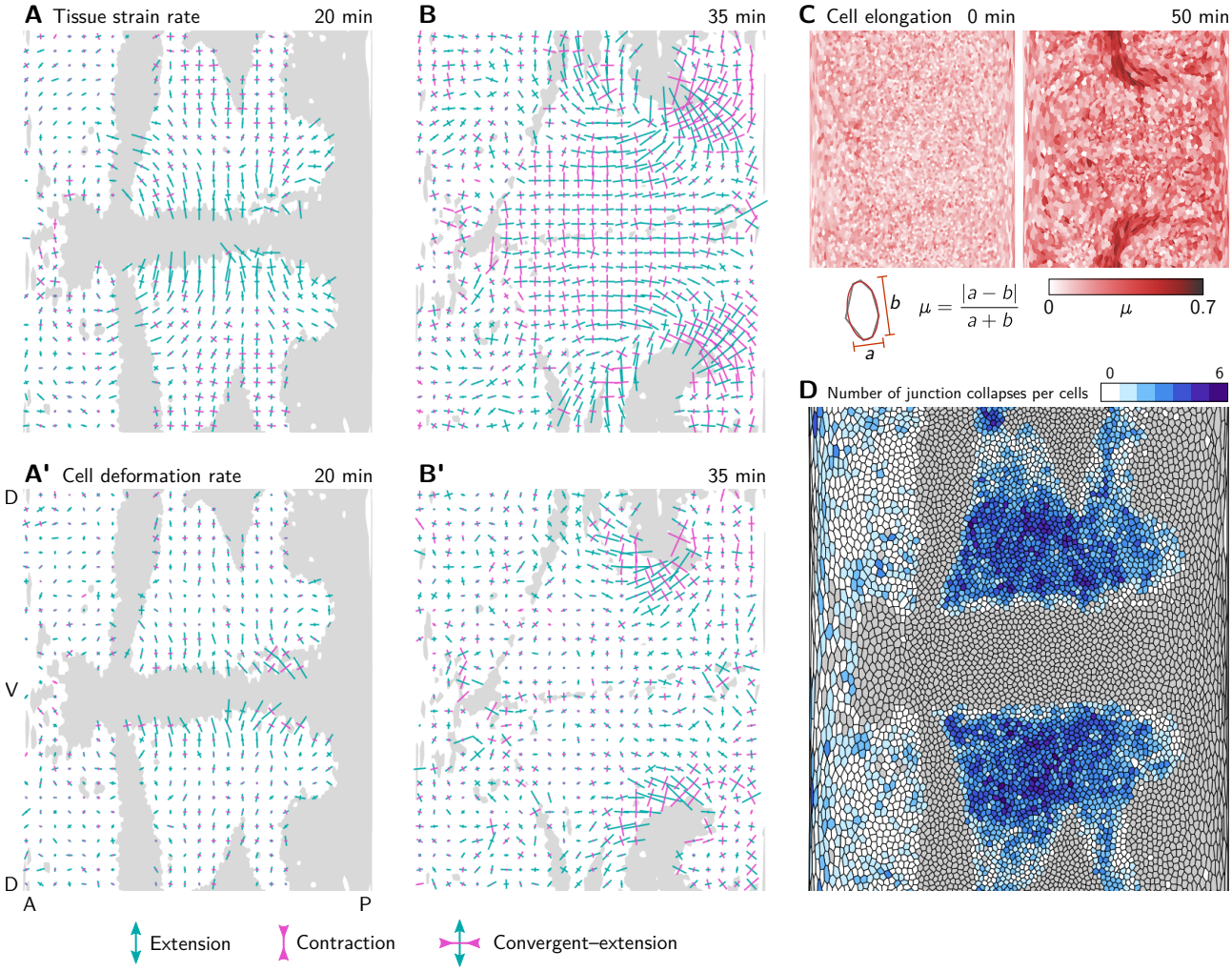

Figure S1: Tissue tectonics analysis. **A and A'** During VF invagination, the tissue strain rate (A) and cell deformation rate (A') are high in the lateral ectoderm adjacent to the ventral furrow, where cells get stretched along the DV axis. Crosses show the principal axis of strain averaged in a grid with 20 µm spacing. Bar length is proportional to the strain rate and color indicates extension (green) and convergence (magenta). **B and B'** During GBE, the tissue strain rate (B) is high in the lateral ectoderm which undergoes convergent extension. The cell deformation rate (B') there is low, and incoherent implying that the tissue deforms via cell rearrangements. In contrast, near the dorsal pole, both cell deformation and cell rearrangements contribute to tissue strain rate. **C** Cell elongation measured by the Beltrami coefficient μ from the best-fit ellipse. Cells near the dorsal pole become highly elongated. **D** Total number of interface collapses per cell. Note that in Ref. [16] (the source of the segmentation data), the number of intercalations per cell is instead calculated as the sum of collapsed interfaces and new interfaces per cell, leading to numbers higher by a factor of 2. (Invaginating cells are shown in gray. Strain rates are only shown for cells that do not invaginate.)

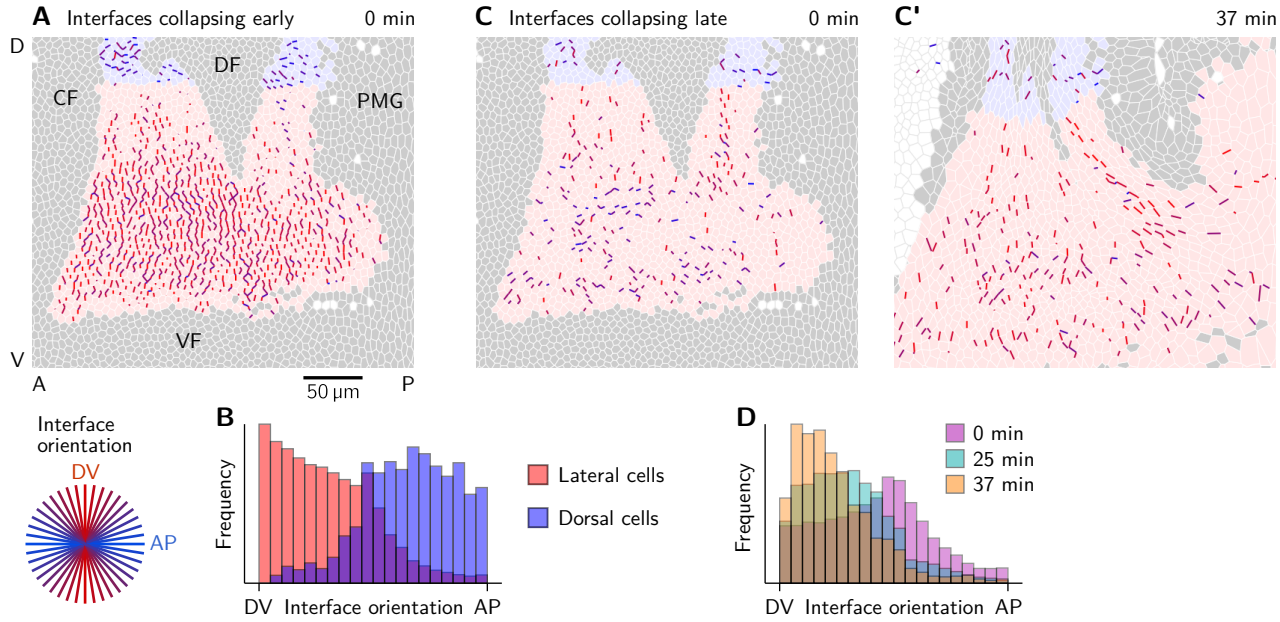

Figure S2: Orientation of collapsing interfaces. **A and B** interfaces collapsing early (before 42 min) colored by their orientation at time 0 min (A) and histograms showing the interface orientation (B). Collapsing interfaces near the dorsal pole (shaded blue) are predominantly oriented along the AP axis. In the lateral ectoderm, the orientation is predominantly along the DV axis. **C–D** Interfaces collapsing late (after 42 min) have low initial orientational bias (C) but progressively align with the co-rotated DV axis before they start contracting (C').

cases where one of the cells is surrounded by the three others. Notably, the quartets don't necessarily exist for the entire time series. Namely, when one of the "inner" interfaces in the quartet, other than the central interface, collapses, the quartet is destroyed.

A T1 event happens when the opposite pairs of cells in the quartet exchange neighbors (i.e. one pair loses contact and the other one gains it). In some cases, the neighbor exchange is not instantaneous, but instead there is a fourfold vertex in the center of the quartet for an extended period. Cases where the central interface and one of its neighbors are simultaneously shorter than a threshold length (0.5 µm) are classified as rosettes and not counted as T1s. The threshold value 0.5 µm corresponds to the average vertex-positions fluctuations on the timescale of 1 min. Higher order rosettes can be "decomposed" into overlapping 5-fold rosettes and therefore can be identified by finding such overlaps.

Using this procedure, we identified 2231 T1 events, 498 five-fold rosettes, 40 six-fold rosettes, 4 seven-fold rosettes and no higher order rosettes (see Fig. 1E'). Because the number of rosettes is small compared to the number of T1s, we have focused on T1 events for the subsequent analysis.

1.4 Local tension inference

Consider the triplet of cells that meet at a tri-cellular vertex and label them $i = 1, 2, 3$. Denote the unit vectors pointing along the three interfaces that meet at the vertex by $\mathbf{e}_{ij}$, where i, j are the labels of the pair of cells that share the respective interface. Force balance implies that

$$T_{12}\mathbf{e}_{12} + T_{23}\mathbf{e}_{23} + T_{31}\mathbf{e}_{31} = 0, \tag{4}$$

where T_{ij} are the cortical tensions. Multiplying the above equation with $\hat{\mathbf{e}}_{12}$ and $\hat{\mathbf{e}}_{23}$ (where $\hat{\mathbf{e}}$ denotes the vector orthogonal to $\mathbf{e}$ and with the same magnitude)

yields two equations

$$\begin{aligned} T_{23}\sin\alpha_{123} - T_{31}\sin\alpha_{312} &= 0, \\ T_{12}\sin\alpha_{123} - T_{31}\sin\alpha_{231} &= 0. \end{aligned} \tag{5}$$

Here, α_{ijk} denotes the angle subtended by the interfaces (ij) and (jk). These equations do not constrain the overall level of tension. We fix this by setting the average tension to 1 which gives the solution These equations are solved by

$$T_{12} = \mathcal{N}\sin\alpha_{231}, \quad T_{23} = \mathcal{N}\sin\alpha_{312}, \quad T_{31} = \mathcal{N}\sin\alpha_{123}, \tag{6}$$

with the normalization factor $a = \sum_{(ijk)} \sin\alpha_{ijk}$.

The above calculation can be generalized to an arbitrary number of vertices. Notably, the equations become overconstrained once the set of vertices contains entire cells [13]. This is because force balance implies that the tension vectors $\mathbf{T}_{ij} = T_{ij}\mathbf{e}_{ij}$ form a triangulation (see below).

Here, we limit ourselves to local tension inference for the central interface in a cell quartet (see Fig. 2A). In this case, the equations are not overconstrained. Labelling the cells 1–4, the equations read

$$\begin{aligned} T_{23}\sin\alpha_{123} - T_{13}\sin\alpha_{312} &= 0, \\ T_{12}\sin\alpha_{123} - T_{13}\sin\alpha_{231} &= 0, \\ T_{34}\sin\alpha_{143} - T_{13}\sin\alpha_{314} &= 0, \\ T_{14}\sin\alpha_{143} - T_{13}\sin\alpha_{431} &= 0. \end{aligned} \tag{7}$$

We solve these equations with the additional constraint that the average of the T_{12}, T_{23}, T_{34} and T_{14} is 1. The solution for "inner" cortical tension T_{13} then is that relative to the average tension of its neighbors. We call this the *relative tension* of a interface in the following.

Analysis of collapsing and emerging interfaces. For the analysis presented in Fig. 2D and E, collapsing and emerging interfaces were identified separately as described in Sec. 1.3. All events before 12 min were excluded from the analysis.

When a interface is short, the interface angles become highly susceptible to fluctuations of the vertex positions. We therefore excluded all timepoints where the central interface or one of its neighbors is shorter than a threshold length (0.75 µm). This value was chosen because the vertex positions fluctuate about 0.5 µm between timepoints. These fluctuations are partially due to intrinsic fluctuations in cortical tension and partially result from limitations in vertex localization during segmentation because of limited optical resolution.

Time series of interface length and relative tension are then aligned such that the interface collapse (respectively emergence) is at $t = 0$. Figure S3 shows the pooled data resolved by the position of the quartet along the DV axis.

1.5 Tension-isogonal decomposition

Because the angles in the tension triangulation are complementary to the interfacial angles in the cell tessellation, one can find a unique tension triangulation (up to a global scale factor) for a given physical cell tessellation in force balance (see dashed gray arrow in Fig. S6A). However, the reverse is not true. For a given tension triangulation, there is a continuous family of cell tessellations that share the same tension triangulation and that are related by *isogonal* deformations which change the interface lengths collectively while preserving the angles. (Mathematically, there are fewer triangulation vertices than cell vertices, so that the triangulation leaves one isogonal mode degree of freedom per cell undetermined. We will use this in Sec. 3 to define an "isogonal potential" that parametrizes the isogonal modes.)

The isogonal degrees of freedom reflect tissue deformations that are not constrained by force balance of cortical tensions. This means that weaker contributions

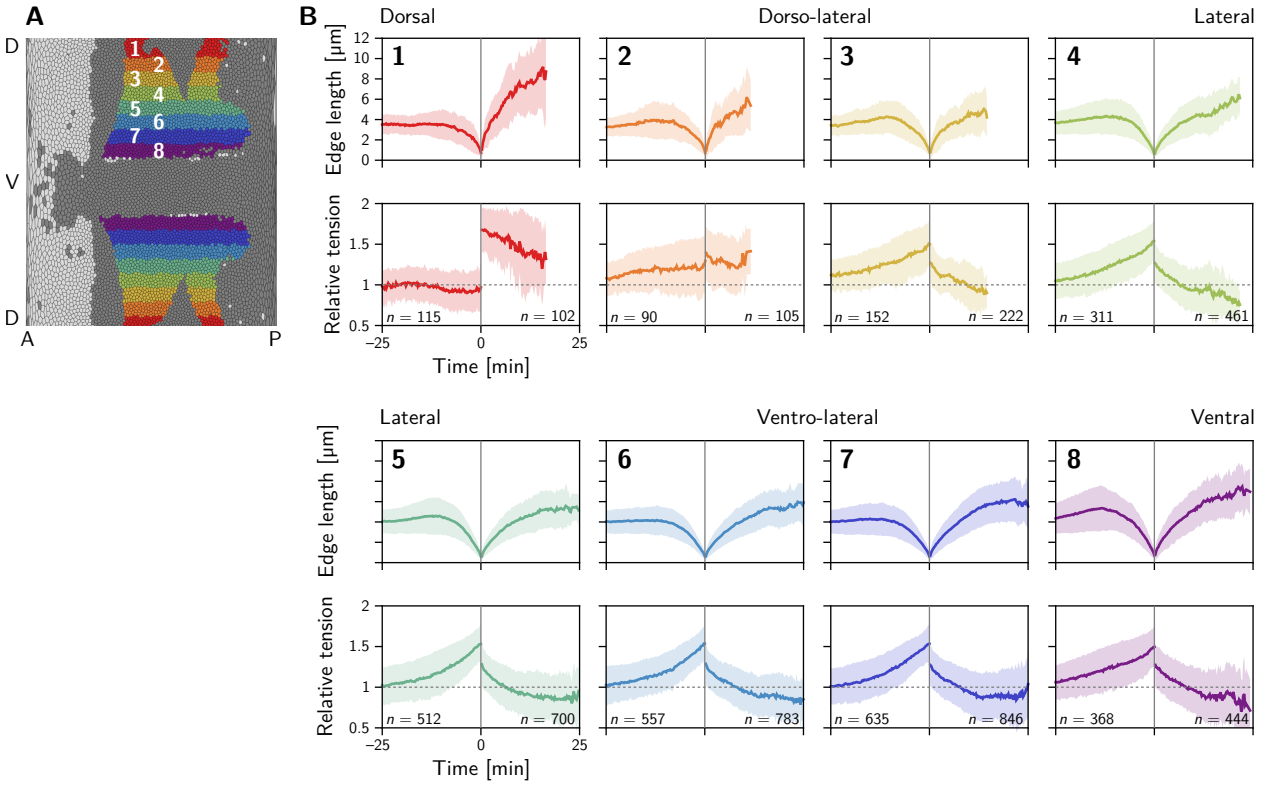

Figure S3: Length and relative tension of the central interface in intercalating cell quartets resolved by DV position. Two distinct classes of behavior are found: in the dorsal-most region (1), the relative tension remains constant at one on the contracting interface and jumps to a high value ($\approx \sqrt{3}$) on the collapsing interface where it slowly relaxes back towards one. In contrast in the lateral ectoderm (regions 3–8), relative tension increases nonlinearly during interface contraction while the tension on the emerging interface starts at a lower value and rapidly relaxes to a value below one. Region 2 is an exception and appears to fall between the two above cases. Collapsing and emerging interfaces were analyzed separately, such that the numbers of events do not match exactly between them. Events are counted as part of a stripe when at least one of the two cells that come into contact comes from that stripe. Because cells converge along the DV axis in the lateral ectoderm, this implies that many interface emergence events are double counted there which inflates the number of emergence events relative to the collapse events.

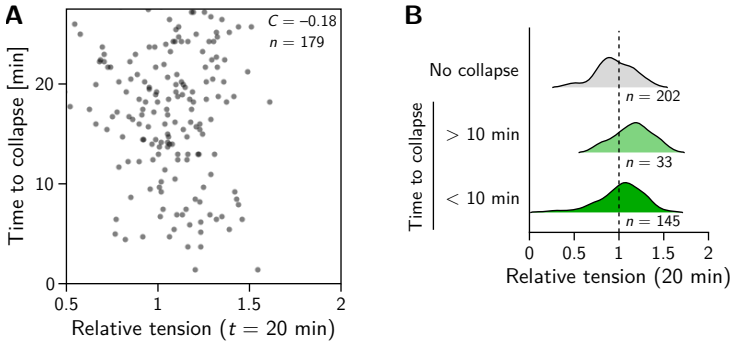

Figure S4: **A** In the amnioserosa relative tension is not correlated with the time until a interface collapses. **B** The distribution of relative tensions on interfaces that collapse is similar to those that persist. Compare to Fig. 2H and J for the quantification of interface collapses in the lateral ectoderm.

to stress, e.g. from intermediate filaments, microtubules and the nucleus in the cell interior, as well as externally applied stresses will drive the isogonal modes. This has two important consequences: (i) For the analysis of experimental data, it implies that we can decompose the tissue deformations into active, tension-driven and passive, isogonal contributions. (ii) For modeling, it implies that we need to specify a cell shape elasticity to fix the isogonal modes (see Sec. 4.2 and Sec. 4.3 below).

In the following, we discuss the details of the *tension–isogonal decomposition*. To achieve a well-defined decomposition of tissue deformation, we need to specify a reference tessellation that is uniquely determined by the tension triangulation. There will then be a unique isogonal deformation that deforms the reference configuration into the physical cell tessellation. Fortunately, we do not need to explicitly construct the reference configuration. Rather, we use the triangulation formed by the cell centroids to quantify the physical tissue shape [52]. (This implies to some degree of coarse-graining, as information about the non-affine displacements of individual vertices is lost.) We can then obtain the isogonal deformation by comparing the tension triangulation to the centroidal triangulation.

Single-vertex level. To make this construction concrete, we first consider a single tri-cellular vertex, with the associated tension triangle $\hat{\mathbf{T}}_{ij}$ and the centroids $\mathbf{c}_i$. The indices $i, j = 1, 2, 3$ label the three cells that meet at the vertex (see Fig. S5A'). The tension triangle vectors $\hat{\mathbf{T}}_{ij}$ are obtained by local tension inference based on the interface unit vectors $\mathbf{e}_{ij}$ (see Sec. 1.4) and a subsequent rotation of the tension vectors by $\pi/2$. To fix the tension scale, we normalize the area of the tension triangle to one. Fixing the tension triangle area is justified because it maintains the total area of the tension triangulation such that cell dilation/contraction are purely isogonal.[1]

We define the local isogonal deformation tensor $\mathbf{I}_{\text{vertex}}$ such that it transforms the tension triangle into the centroidal triangle. Mathematically, this definition is written as the equations $\eta\, \mathbf{I}_{\text{vertex}}.\hat{\mathbf{T}}_{ij} = \mathbf{c}_j - \mathbf{c}_i$, $i \neq j \in \{1, 2, 3\}$. The scale factor η converts units of tension (a.u.) into units of length. How we fix η is described below.

Because the isogonal modes must preserve angles, they cannot include rotations. In other words, $\mathbf{I}_{\text{vertex}}$ must be a symmetric tensor, and therefore has only 3 degrees of freedom. However, the above equations impose 4 constraints. We therefore determine $\mathbf{I}_{\text{vertex}}$ using least squares, i.e. by solving the minimization problem

$$\min_{\mathbf{I}_{\text{vertex}} \in \text{Sym}_2} \sum_{(ij)} ||\eta \mathbf{I}.\hat{\mathbf{T}}_{ij} - \mathbf{d}_{ij}||^2 \tag{8}$$

where Sym_2 is the set of symmetric 2×2 matrices.

Fixing the scale factor η. To fix η we use that the tension triangles are initially close to equilateral (as evidenced by the angle distribution peaked around $\pi/3$, see Fig. 5L). For an equilateral triangle, the edge length is determined by the area, which we have normalized to one, giving an edge length $2/3^{1/4} \approx 1.52$. The average edge length of the centroidal triangles is given by the average centroid distance between adjacent cells, which we find to be 6.38 µm. The ratio of these two numbers gives a scale factor $\eta \approx 4.2\,\mu\text{m}$. This scale factor minimizes the isogonal strain at $t = 0$ (see Fig. S5B). Indeed, minimizing $\langle ||\mathbf{I}|| \rangle$ at a reference time is provides a more general way to determine η in cases where the initial triangulation is not as uniform and regular as in the *Drosolphila* blastoderm.

Coarse-grained isogonal strain. To find the tissue scale isogonal strain, we coarse grain the isogonal deformation tensor on a square grid in the flat map projection ("pullback"). The grid spacing is set to 20 µm, such that each grid facet

[1] The numerical value of the tension triangle area is immaterial, since it can be absorbed in the scale factor η.

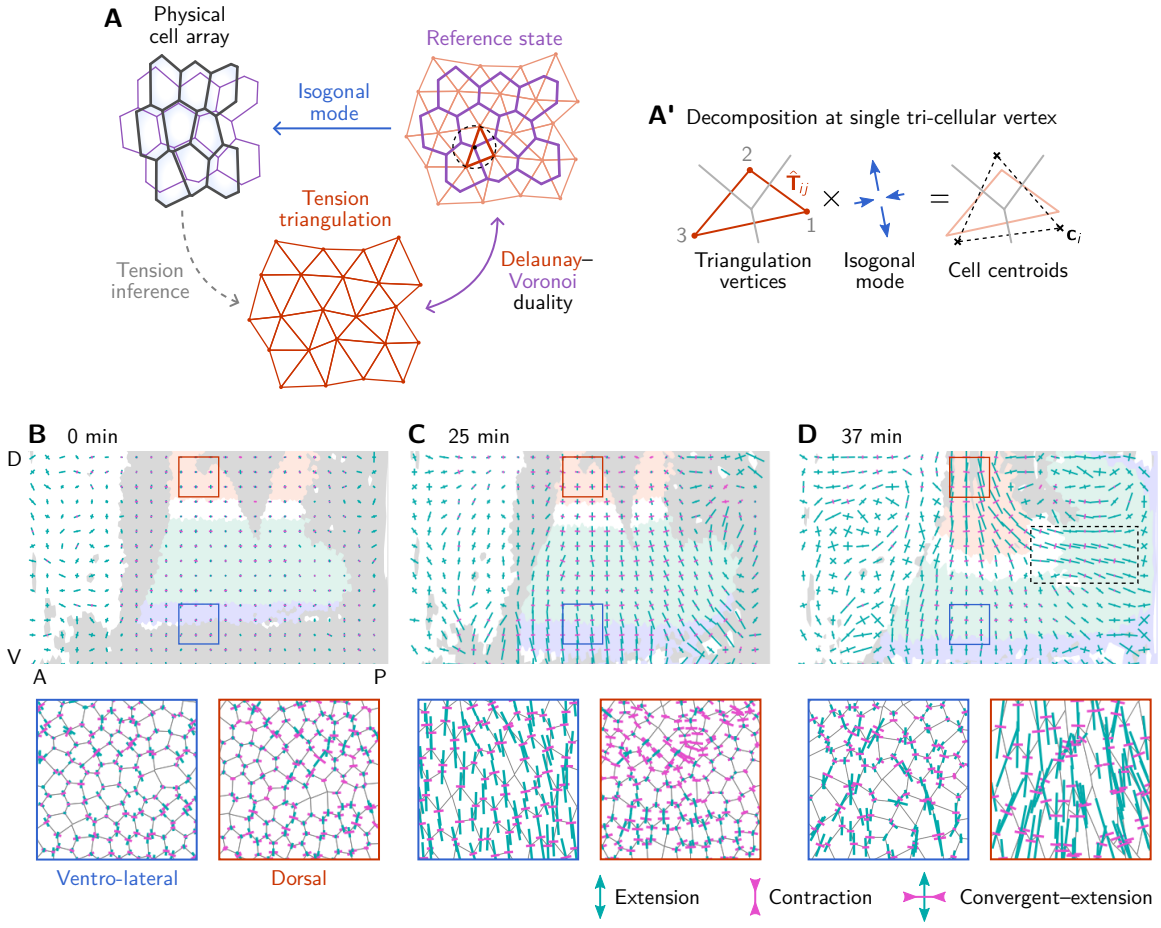

Figure S5: Tension–isogonal decomposition: Single-vertex analysis and coarse graining. **A** To a given tension triangulation (red), a corresponding dual cell tessellation is obtained via the Voronoi construction (purple), which is based on the circumcircles of the triangles. Because the tension triangulation fixes only the angles, it leaves freedom for *isogonal* (angle-preserving) modes that collectively change the interface lengths. Deformations of the tissue can be decomposed into deformations of the tension triangulation and isogonal deformations. **A'** The tension–isogonal decomposition at a single vertex based on the tension triangulation vectors $\hat{\mathbf{T}}_{ij}$ and the cell centroids $\mathbf{c}_i$. The indices i, j label the three cells that meet at the vertex. **B–D** Coarse-grained isogonal strain (top) and isogonal strain at individual vertices (insets) for different timepoints. The initial isogonal strain (B) is minimized to fix the scale factor η. During VF invagination, the lateral ectoderm close to the ventral furrow is stretched (C). During GBE, the isogonal strain in the lateral ectoderm remains approximately constant while the amnioserosa gets stretched. Crosses show the principal axes of the local isogonal strain tensor. Bar length indicates the amount of strain (green = extension, magenta = contraction). Coarse-grained strain tensors were averaged on a grid with spacing 20 µm. Insets show regions with size 50×50 µm^2.

contains ca 10–15 cells (grid facets near the poles contain less cells because of the distortion caused by the pullback projection). We calculate $\mathbf{I}_{\text{vertex}}$ for all tri-cellular vertices in a grid facet and take the average to find $\mathbf{I}_{\text{facet}}$.

Figures 3D and S5B–D (top panels) show the isogonal strain tensor $\mathbf{I}_{\text{facet}} - \mathbb{I}$, where $\mathbb{I}$ is the identity matrix. The bottom panels in Fig. S5B–D show the individual, single-vertex strain tensors $\mathbf{I}_{\text{facet}} - \mathbb{I}$ at each vertex. Crosses indicate the principal eigenvectors of the strain tensors. The bar length is proportional to the eigenvalue. Green (magenta) indicates a positive (negative) eigenvalue, i.e. contraction (elongation).

To calculate the average isogonal deformation in different tissue regions (Fig. 3E), we first transform the single-vertex isogonal deformation tensor to the local co-rotating ("Lagrangian") frame (see Sec. 1.2). This is important because the germ band rotates as it moves over the posterior pole during elongation.

To estimate the critical tension for T1s in the lateral ectoderm, we need the average isogonal contribution to the length of DV-oriented interfaces, $\langle \ell_{\text{iso}} \rangle$ (see Sec. 1.6). At the end of VF invagination ($t = 25\,\text{min}$), we find $\langle (\mathbf{I}_{\text{vertex}})22 \rangle \approx 1.538 \pm 0.006$, where the index 2 denotes the DV component and the average is taken over cells in the lateral ectoderm (region shaded in blue in Fig. S5C). We thus have $\langle \ell_{\text{iso}} \rangle = (\mathbf{I}_{22} - 1)\langle \ell(0) \rangle \approx 1.9\,\mu\text{m}$ for DV-oriented interfaces, where $\langle \ell(0) \rangle \approx 3.5\,\mu\text{m}$ is the average initial interface length.

Filtering of degenerate tension triangles. When one of the angles at a vertex is close to π, the tension triangle becomes highly elongated. In fact, sometimes one of the angles at a vertex exceeds π due to fluctuations and inaccuracies in detection. In the tension inference, this leads to negative tensions. The (nearly) degenerate tension triangles, in turn lead to extreme apparent local isogonal deformations. We therefore exclude nearly degenerate tension triangles whose perimeter is larger than 8 after normalizing the area to 1 (ca. 2% of the tension triangles are filtered out this way).

Quartet shape tensors. The tension–isogonal decomposition for cell quartets is calculated analogously to the procedure for single vertices. The two tension triangles associated to the inner vertices of the cell quartet form a "kite" (see Fig. S6A). We normalize tension such that the average area of the tension triangles is one. The quartet's isogonal deformation tensor $\mathbf{I}_{\text{quartet}}$ is defined such that it transforms the vectors $\mathbf{T}_{ij}$ into the corresponding centroidal displacement vectors $\mathbf{c}_j - \mathbf{c}_i$. Here, we only use the vectors around the perimeter of the tension and centroidal kite. This ensures that the isogonal deformation tensor varies continuously through the cell neighbor exchange where the inner edge in the kite is flipped. As in the single-vertex case, we find $\mathbf{I}_{\text{quartet}}$ using least squares.

To quantify the deformations of the tension kite and the physical cell quartet, we define the shape tensors

$$\mathbb{G}_{\text{T}} = \eta^2 \sum_{(ij)} \hat{\mathbf{T}}_{ij} \otimes \hat{\mathbf{T}}_{ij}, \tag{9}$$

$$\mathbb{G}_{\text{C}} = \sum_{(ij)} (\mathbf{c}_i - \mathbf{c}_j) \otimes (\mathbf{c}_i - \mathbf{c}_j), \tag{10}$$

where the index pairs (ij) run over cell pairs going around the quartet, i.e. $(ij) = (12), (23), (34), (41)$. Notably, with these definitions, one has the relation

$$\mathbf{I}_{\text{quartet}}.\mathbb{G}_{\text{T}}.\mathbf{I}_{\text{quartet}} \approx \mathbb{G}_{\text{C}}. \tag{11}$$

Remarks on the Voronoi construction for the reference cell tessellation. For the tension–isogonal decomposition, we have circumvented the explicit construction of a reference cell tessellation by directly comparing the tension triangulation

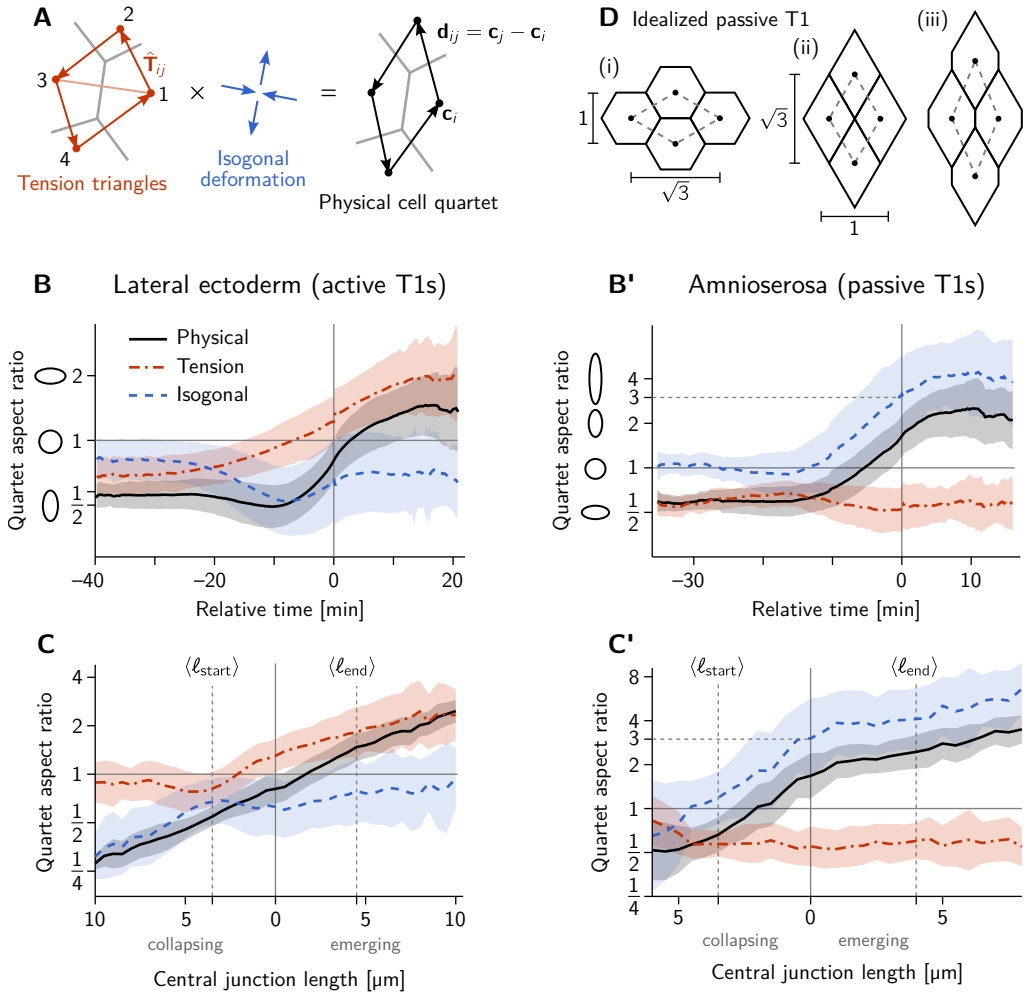

Figure S6: **A** Tension–isogonal decomposition for a cell quartet. The isogonal deformation is defined as the tensor that deforms the "kite" formed by the tension vectors $\mathbf{T}_{ij}$ into the corresponding centroidal kite, formed from the cell centroids $\mathbf{c}_i$. The indices (ij) label the four cell pairs going around the kite: (12), (23), (34), (41). **B–C'** Quartet aspect ratio and eigenvalue ratio of the isogonal deformation tensor as a function of time relative to the T1 event (B and B') and as a function of the central interface's length (C and C'). The isogonal deformation seen in B from -20 to -10 min and in C for collapsing edge lengths $> 4\,\mu$m is driven by the VF invagination which stretches the germ band.) **D** Passive intercalation of an idealized cell quartet composed of regular hexagons: (i) initial configuration; (ii) four-fold vertex configuration after area-preserving isogonal shear changing the aspect ratio by a factor 3; (iii) further isogonal deformation after the neighbor exchange. Black disks mark the cell centroids used to define the quartet shape (see A).

to the centroidal triangulation of the physical cells. This approach is particularly useful because a local isogonal deformation tensor can be obtained on the level of a single tri-cellular vertex.

The explicit construction of the reference cell tessellation will help us understand the geometry of cell-neighbor exchanges and find a criterion for when they occur (see Sec. 1.6 below). We define the reference tesselation using a generalized Voronoi construction based on the tension triangulation. The vertices of this generalized Voronoi tessellation are given by the circumcircle centers of the triangles in the triangulation. The generalized Voronoi tessellation is only free of self-interesections when the triangulation fulfills the Delaunay criterion that opposite angles in adjacent triangles must sum to a value smaller than π. As we will see, in the following section, this provides a purely geometric criterion for neighbor exchanges in the absence of isogonal strain. In the presence of isogonal strain, the reference can have self intersections (i.e. negative interface lengths). This is similar to how the reference state encoding plastic deformations in finite strain theory isn't necessarily geometrically compatible [94].

In general, the centroids of the generalized Voronoi cells will not coincide with the vertices of the tension triangulation. This means that the definition of the isogonal deformation tensor based on the tension triangulation vertices is not exactly identical to that based on an explicit Voronoi construction. However, the two agree for a periodic lattice of identical tension triangles. In this case, the vertices of the tension triangulation coincide exactly with the centroids of the generalized Voronoi tessellation. In other words, using the tension triangulation vertices to define isogonal deformations amounts to approximating tissue as locally lattice-like, which is valid when spatial gradients are small on the cell scale.

In passing, we note that the generalized Voronoi tessellation is not the only possible reference state. Any tessellation that is uniquely defined by a given tension triangulation is in principle a valid reference state. The Voronoi tessellation is a useful choice for the following analysis because the Voronoi cell shapes behave similar to the actual cell shapes and because it is defined purely geometrically. Other choices of the reference state might be of use depending on the particular question and when one has more detailed information about the mechanical properties of the cells.

1.6 The T1 threshold

In the main text, we have discussed the case of two identical, symmetric tension triangles, which are characterized by a single angle (denoted ϕ in Fig. 3F). We now discuss the general setting, which is characterized by four angles α and α', β, and β' (see Fig. S7A). The reference length of the central interface in the quartet, ℓ_{ref}, is given by

$$\ell_{\text{ref}} = \frac{\eta T}{2}(\cot\beta + \cot\beta'), \tag{12}$$

where T is the tension on the central interface and η is the global scale factor that converts units of tension to physical lengths. Equation (12) follows from the circumcircle construction of the Voronoi tessellation: The vertices of the Voronoi tessellation are the centers of the corresponding triangles in the Delaunay triangulation. Notably, ℓ_{ref} vanishes when $\beta + \beta' = \pi$, which is the edge flip condition for a Delaunay triangulation ensuring that the Voronoi tessellation remains free of self intersection. Such self-intersection occur when $\beta + \beta' > \pi$, which implies $\ell_{\text{ref}} < 0$. In a tissue, this can only happen if $\ell_{\text{iso}} > -\ell_{\text{ref}}$ such that the physical interface length $\ell = \ell_{\text{ref}} + \ell_{\text{iso}}$ always remains positive. In other words, the isogonal modes lead to a generalized Delaunay condition, which is controlled by ℓ_{iso} in addition to the angles.

In the main text, we have discussed the T1 threshold that follows from this generalized Delaunay condition for the maximally symmetric case of a pair of identical, isosceles tension triangles [$\alpha' = \alpha = (\pi - \beta)/2$, $\beta' = \beta$; in the main text, we used the

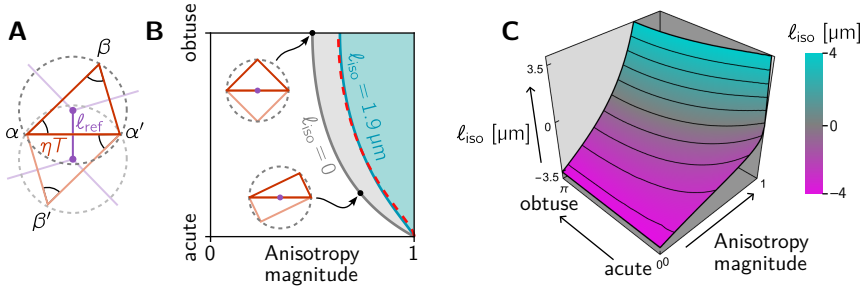

Figure S7: Generalized Delaunay condition in the triangle shape space. **A** Circumcircle construction of the Voronoi edge length (purple) from a pair of adjacent (tension) triangles (red). Circumcircles are indicated by gray dashed lines. **B** Delaunay threshold (gray) and generalized Delaunay threshold for non-zero isogonal strain (blue). The red dashed line shows an approximation of the T1 threshold in terms of a critical angle $\beta_{\rm crit}(\ell_{\rm iso})$, independent of α. **C** T1 threshold surface in the spaced spanned by the triangle shape space and the isogonal length $\ell_{\rm iso}$.

symbol ϕ instead of β for the angle opposite of the central interface]. For $\beta > \pi/3$, such triangles are obtuse corresponding to perfect tension bridges.

In the triangle shape space shown in Fig. S7 this corresponds to the top edge. If we generalize to a pair of identical, non-isoceles triangles by varying $\alpha = \alpha'$ independently of β, we can trace out the T1 threshold in the triangle shape space. The case $\alpha = \beta$ gives the maximally obtuse triangle (for a given β) which is at the bottom edge of the triangle shape space. In the absence of isogonal strain ($\ell_{\rm iso} = 0$), the T1 threshold is given by the Delaunay condition $\beta = \pi/2$, which yields the gray line in Fig. S7.

For $\ell_{\rm iso} \neq 0$, the T1 threshold is given by $\ell_{\rm ref} + \ell_{\rm iso} = 0$. To find $\ell_{\rm ref}$ as given by Eq. (12), we need the tension T in terms of the angles α, β. In other words we need to fix the scale of tension, which we do by normalizing the tension triangle area to one: $T = \sqrt{2\sin(\beta)/(\sin\alpha + \sin(\alpha+\beta))}$. This ensures that all tension-driven deformations are area preserving, such that tissue dilations or contractions are reflected by isogonal deformations. (Alternative ways to normalize the tension scale are to fix the "outer" tensions or the perimeter of the tension triangle, which effectively fixes the total tension, mimicking a limited myosin pool. The T1 threshold found in these cases do not differ significantly from the area-based tension normalization.)

Taken together, we have

$$\ell_{\rm ref}(\alpha,\beta) = \eta\sqrt{\frac{2\sin\beta}{\sin\alpha + \sin(\alpha+\beta)}}\,\cot\beta. \tag{13}$$

For a given $\ell_{\rm iso}$, the T1 condition $\ell_{\rm ref}(\alpha,\beta) + \ell_{\rm iso} = 0$ then defines a threshold line in the triangle shape space, as show Fig. S7B. Plotting $\ell_{\rm iso}$ as the third dimension gives a T1 threshold surface (see Fig. S7C). Positive isogonal strain shifts the critical tension anisotropy to higher values. Vice versa, the critical tension anisotropy drops to zero as $\ell_{\rm iso}$ approaches the value reference interface length for an equilateral triangulation $\ell_0 = 2\eta/3^{3/4} \approx 3.68\,\mu$m. This defines the critical isogonal strain for purely passive T1s.

Recall that for $\ell_{\rm iso} = 0$, the T1 threshold is given by the Delaunay condition $\beta = \pi/2$, and independent of α. For $\ell_{\rm iso} \neq 0$, we can still define a generalized critical angle $\beta_{\rm crit}$ by considering the isosceles case $\alpha = (\pi - \beta)/2$:

$$-\frac{\ell_{\rm iso}}{\eta} \stackrel{!}{=} \frac{\cot\beta_{\rm crit}}{\sqrt{\cot(\beta_{\rm crit}/2)}} \tag{14}$$

For $\eta = 4.2\,\mu$m and $\ell_{\rm iso} = 1.9\,\mu$m, this equation is solved by $\beta_{\rm crit} \approx 1.77 \approx 1.13\,\pi/2$. Notably, this critical angle provides a good approximation for the tension threshold

even for arbitrary values of α, i.e. non-isosceles triangles (see red dashed line in Fig. S7B). This approximation is attractive because it emphasizes the geometric character of the T1 threshold and because β can be read off directly in the tension triangulation.

1.7 Local tension anisotropy

From the tension vectors $\mathbf{T}_{ij}$ at a vertex, we calculate the "tension anisotropy" tensor

$$\mathbb{T} = \frac{1}{\mathcal{N}^2} \sum_{(ij)} \mathbf{T}_{ij} \otimes \mathbf{T}_{ij} \tag{15}$$

where the sum runs over pairs from the set of the three cells that meet a the vertex. The normalization factor $\mathcal{N}^2 = \sum_{(ij)} T_{ij}^2$ is chosen such that $\mathrm{Tr}\,\mathbb{T} = 1$. The difference of the eigenvalues of $\mathbb{T}$ quantifies the magnitude of tension anisotropy. When the interface angles at the vertex are all identical to 120° the tension anisotropy vanishes. For non-identical vertex angles the tension is locally anisotropic and the dominant eigenvector of $\mathbb{T}$ points along the principal axis of stress. Anisotropic tension also implies that the tension triangle is non-equilateral. The tension triangle's axis of elongation is perpendicular to the principal axis of tension because the tension triangle vectors are rotated by 90° relative to the interfaces (cf. Fig. 2B).

In passing, we note that the tension anisotropy tensor is closely related, but not exactly equal, to the stress tensor σ. Instead it has the form of a metric tensor and thus describes the local geometry of tension space. Specifically, the $\mathbb{T}$ measures the *extrinsic* anisotropy of tension and is complementary to the *intrinsic* shape tensor that we will introduce in the next section.

1.8 Local tension configuration

In the main text, we argued that local configuration of tensions at a vertex is characterized by the shape of the tension triangle. Specifically, acute triangles correspond to tension cables, while obtuse triangles correspond to tension bridges (see Fig. S8A).

Whether a triangle is obtuse or acute is an *intrinsic* property, i.e. it is independent of the position, orientation and size of the triangle in the embedding space. The intrinsic shape of a triangle is given by its angles. Since these angles sum to π, we can represent the space of triangle shapes in barycentric coordinates (see Fig. S8B). The center of the barycentric shape space corresponds to an equilateral triangle, while the edges correspond to triangles where one angle is zero and the corners to triangles where two angles are zero. Because the order of labeling the angles in the triangle is arbitrary, the shape space is invariant under permutations of the angles and a single fundamental domain (highlighted in Fig. S8B) is representative.

In the triangle shape space, we have colored each point according to how anisotropic and how acute-vs-obtuse it is. We already know that we can read off the magnitude of anisotropy from the eigenvalues of the tensor $\mathbb{T}$, defined in the previous subsection. To quantify the shape (acute vs obtuse), we define a second tensor

$$(\mathcal{S})_{IJ} = \frac{1}{\mathcal{N}^2}\, \mathbf{T}_I \cdot \mathbf{T}_J, \tag{16}$$

where the indices $I, J \in \{1, 2, 3\}$ are short hand labels for the three interfaces that meet a tri-cellular vertex. Because $\sum_I \mathbf{T}_J = 0$ (force balance), this tensor has the null vector $(1, 1, 1)^{\mathrm{T}}$. To get rid of this nullspace, we go to barycentric coordinates by defining the pair of vectors, $\boldsymbol{\tau}_{1,2}$ that we pack into a matrix

$$\mathfrak{T} = \begin{pmatrix} \boldsymbol{\tau}_1 \\ \boldsymbol{\tau}_2 \end{pmatrix} = \frac{1}{\sqrt{2}\mathcal{N}} \begin{pmatrix} \mathbf{T}_1 - \mathbf{T}_2 \\ \mathbf{T}_3 / \sqrt{3} \end{pmatrix}. \tag{17}$$

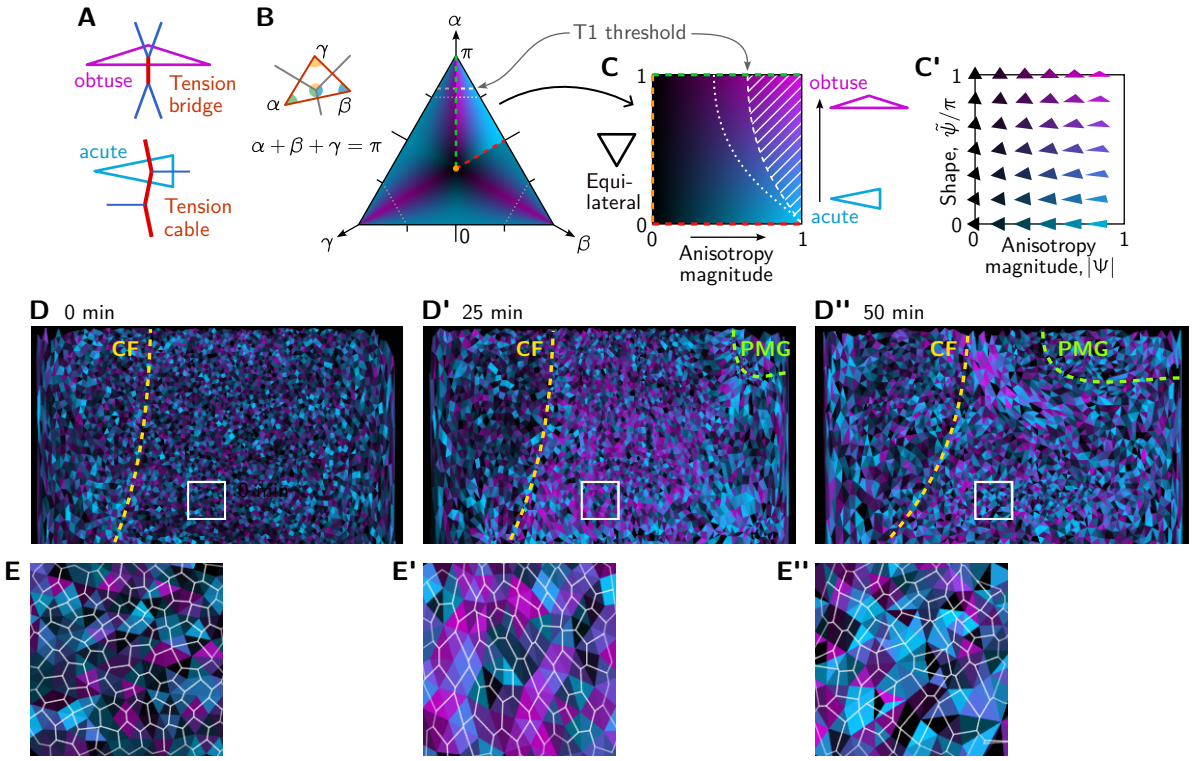

Figure S8: Quantification of local tension configurations (LTC) in terms of tension triangle shape. A Tension triangle shape characterizes the local tension configuration. **B** Space of triangles in in barycentric coordinates using the angles $\alpha + \beta + \gamma = \pi$. Color indicates the degree of acuteness vs obtuseness by hue from cyan to magenta and the magnitude of anisotropy by brightness (see text for details). A single fundamental domain is highlighted. The remaining shape space is composed of rotated and reflected copies of this fundamental domain, corresponding to permutations of the angles α, β, γ. Dashed white lines indicate the threshold for neighbor exchanges based on the (generalized) Delaunay condition for pairs of identical tension triangles (see Sec. 1.6). **C and C'** Triangle shape space spanned by the anisotropy magnitude $|\Psi|$ and acute-vs-obtuse parameter $\tilde{\psi}$ as axes. See main text for the definitions of Ψ and $\tilde{\psi}$. **D–D"** Snapshots showing the tension configuration at the onset of GBE. For each vertex, a triangles is drawn between the centroids of the adjacent cells and colored according to the tension triangle associated to the vertex. Yellow and green lines marks the cephalic furrow (CF) and the boundary of the posterior midgut (PMG), respectively. **E–E"** Blowups of the white square in (D–D").

These vectors have the defining property that they are orthogonal to one another and to the null vector $(1,1,1)^{\mathrm{T}}$ of $\mathcal{S}$. Now we we can define the shape tensor

$$\mathbb{S} = \mathfrak{T}\mathfrak{T}^{\mathrm{T}} = \begin{pmatrix} ||\boldsymbol{\tau}_1||^2 & \boldsymbol{\tau}_1 \cdot \boldsymbol{\tau}_2 \\ \boldsymbol{\tau}_1 \cdot \boldsymbol{\tau}_2 & ||\boldsymbol{\tau}_2||^2 \end{pmatrix}. \tag{18}$$

Observe that

$$\mathfrak{T}^{\mathrm{T}}\mathfrak{T} = \boldsymbol{\tau}_1 \otimes \boldsymbol{\tau}_1 + \boldsymbol{\tau}_2 \otimes \boldsymbol{\tau}_2 = \mathbb{T}, \tag{19}$$

which implies that $\mathbb{T}$ and $\mathbb{S}$ share the same eigenvalues. In fact we can perform a singular value decomposition of $\mathfrak{T}$

$$\mathfrak{T} = R(\psi/2)\boldsymbol{\Lambda}R(-\phi), \tag{20}$$

where $R(\phi)$ is the rotation matrix with angle ϕ and $\boldsymbol{\Lambda} = \mathrm{diag}\,(\lambda_1, \lambda_2)$ is a diagonal matrix of singular values whose squares λ_1^2, λ_2^2 are the eigenvalues of $\mathbb{T}$ and $\mathbb{S}$. Because we normalized the tension vectors, $\mathrm{Tr}\,\mathbb{T} = \mathrm{Tr}\,\mathbb{S} = \lambda_1^2 + \lambda_2^2 = 1$. ϕ is the angle of the dominant eigenvector in physical space, which gives the orientation of the principal axis of stress. As we will see below, the angle ψ indicates whether the triangle is obtuse or acute. The reasoning to define the rotation based on $\psi/2$ will become apparent below when we represent the shape tensor by a complex number.

The shape tensor $\mathbb{S}$ has only two degrees of freedom, the difference of eigenvalues $\lambda_1^2 - \lambda_2^2$ (which it shares with the tensor $\mathbb{T}$) and the angle ψ that sets the orientation of its two orthogonal eigenvectors. We can represent $\mathbb{S}$ by a complex number

$$\Psi = \frac{\tau_1^2 - \tau_2^2 + 2i\,\boldsymbol{\tau}_1 \cdot \boldsymbol{\tau}_2}{\tau_1^2 + \tau_2^2} = |\Psi| e^{i\psi}, \tag{21}$$

where $|\Psi| = |\lambda_1^2 - \lambda_2^2|$ is the magnitude of tension anisotropy and the phase ψ is the "shape space angle" defined by Eq. (20).

Permutations of the edge indices α correspond to sign changes and rotations of ψ by integer multiples of $2\pi/3$. To mod out these group actions (which correspond to the symmetries of the barycentric shape space Fig. S8B), we define

$$\tilde{\psi} = |(3(\pi + \psi) \bmod 2\pi) - \pi| \in [0, \pi] \tag{22}$$

This shape parameter informs how acute or obtuse a tension triangle is. For an acute isosceles triangle, $\tilde{\psi} = 0$, whereas for an obtuse isosceles triangle $\tilde{\psi} = \pi$. For non-isosceles triangles, $\tilde{\psi}$ takes values in $[0, \pi]$ quantifying the relative degree of acuteness vs obtuseness. For an equilateral triangle, $|\Psi| = 0$ and $\tilde{\psi}$ is not defined. The axes $|\Psi|$ and $\tilde{\psi}/\pi$ span the space of triangle shapes shown in Fig. S8.

As an alternative to the above mathematical derivation of the shape parameter, we briefly discuss a more intuitive parameter as follows: For a given tension triangle, label its edges in ascending order of length (i.e. T_2 and T_3 will second highest and highest tension, respectively. We can now define a the parameter

$$p = 2\frac{|T_2 - T_3|}{T_2 + T_3} \in [0, 1], \tag{23}$$

which quantifies the relative tension difference between the two largest tensions at a vertex. For a tension cable, there are two large tensions which are similar in magnitude, implying that p is small. For a tension bridge, there is one high tension edge meeting two low tension edges so p will be closer to 1. The maximal value $p = 1$ is reached for $T_1 = T_2 = T_3/2$. Remarkably, to very good approximation $p \approx |\Psi|\tilde{\psi}/\pi$.

Random Delaunay triangulation. As a reference for the triangle shape distributions, we generated random Delaunay triangulations based on the Ginibre random point process [95]. A small sample of such a random triangulation is shown in Fig. S9A. The histograms in the triangle shape space Fig. S9B shows good agreement

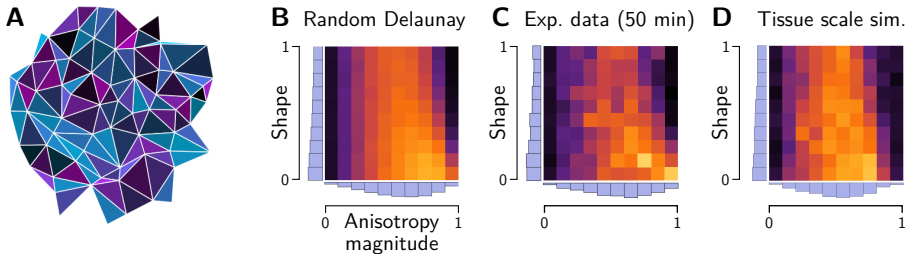

Figure S9: Random Delaunay triangulation seed by Ginibre random point process. **A** Small patch of a random triangulation. Triangles have been colored according to the shape parameters $(|\Psi|, \tilde{\psi})$ (cf. Fig. S8C). **B–D** Histograms showing the triangle shape distribution for the Ginibre-based random Delaunay triangulation (B), tension triangles from the lateral ectoderm at the end of GBE (C, cf. Fig. 5G), and tension triangles at the final timepoint of tissue-scale simulations (D).

between the Ginibre-based random Delaunay triangulation and the distribution of tension triangle shapes at the end of GBE. Moreover, the marginalized angle distribution, shown in Fig. 5L (black dashed line), closely matches the experimentally observed distribution.

These findings suggest that the local coordination of cortical tensions is lost during GBE and that the local tension configurations approach a maximally disordered state.

1.9 Hexagonal and hexatic order

We quantify order of the cell arrangement in the tissue by two measures: (i) the fraction of six-sided cells, that one might loosely call "hexagonal order" and (ii) the hexatic order parameter. Hexagonal order is a topological quantity – it depends only on the neighborhood relations between cells but not on their exact shape. In contrast, hexatic order (defined below) is a geometric measure, that is sensitive to the cell shapes. Initially, the majority of cells are hexagons (Fig. S10A, 0 min), and the density of topological defects, manifested as non-hexagonal cells, is relatively low. During VF invagination, the number of defects increases only slightly (25 min) since there are only very few intercalations (cf. Fig. 1E). During GBE, the number of defects increases significantly as a consequence of T1s. Towards the end of GBE, the distribution of cell-coordination number approaches that of a random Voronoi tessellation seeded with a Ginibre random point process (see Fig. S10B and B').

Hexatic order. The hexatic order parameter (also called "bond orientational order parameter" [97]) for a cell with n vertices is defined as

$$\psi_6 = \frac{1}{n} \sum_{k=1}^{n} \exp(6i\theta_k), \tag{24}$$

where θ_k is the angle between the DV axis and the vector pointing from the cell's centroid to vertex k. For a cell with regular hexagonal shape the magnitude of ψ_6 reaches its maximum $|\psi_6| = 1$. The phase $\arg \psi_6$ indicates the orientation of the hexagon. In contrast to the coordination number, which is a purely topological measure, the hexatic order parameter depends on the cell shape. We find that the hexatic order parameter to be low in magnitude and exhibit no long-range correlations as is apparent from Fig. S10C. Effectively, the presence of non-hexagonal cells act as obstructions to long range correlations of geometric order. We quantify the range of correlations in hexatic order by coarse graining over patches of cells with different radii (measured in the by the neighborhood degree). Before the onset of GBE, the coarse grained order parameter decays as a power law of the patch radius

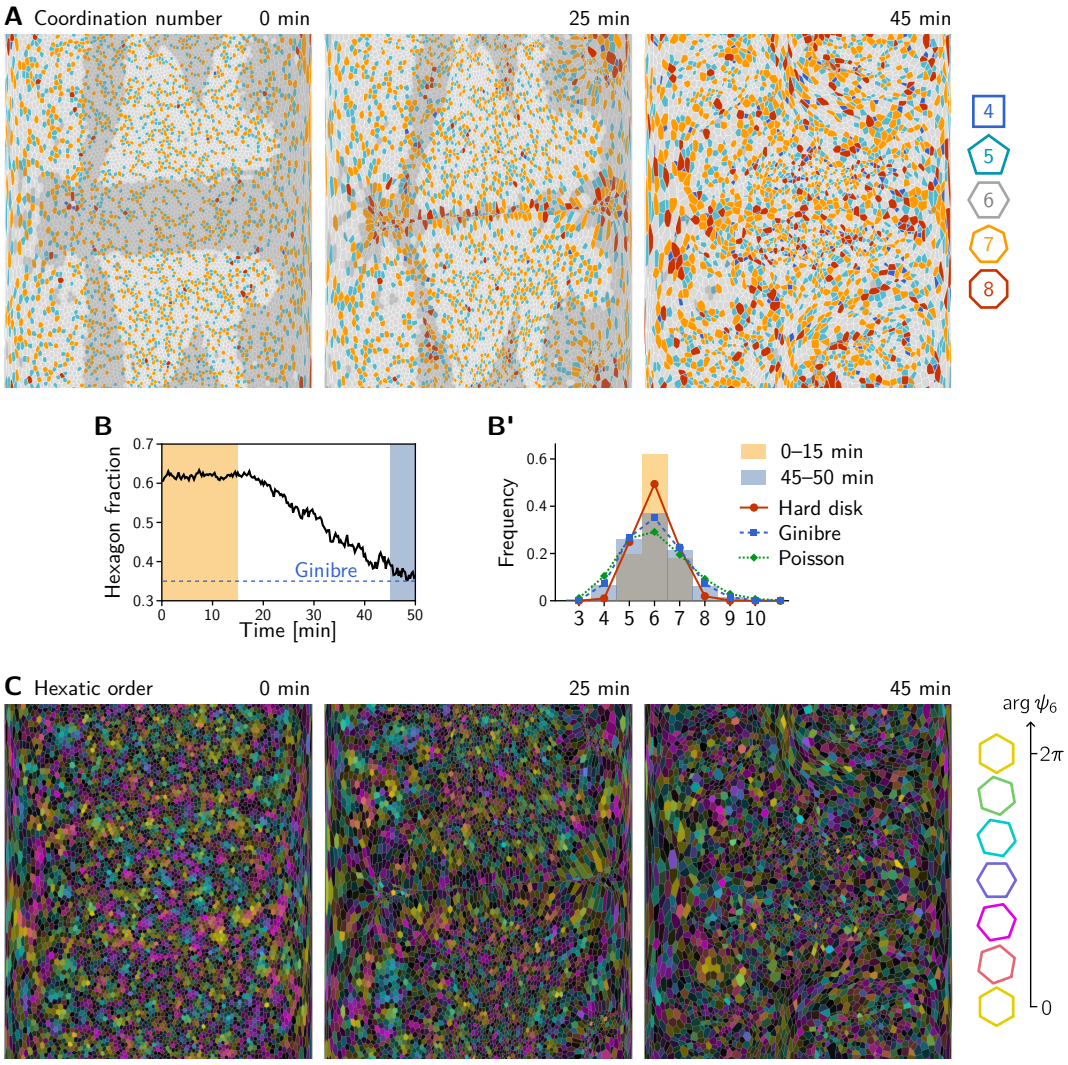

Figure S10: Coordination number and hexatic order of cells. **A** Initially (0 min), the majority of cells are hexagonal (light gray). During GBE (25–50 min), topological defects proliferate, resulting in increasing numbers of non-hexagonal cells. Semitransparent gray overlay marks cells that invaginate. **B** and **B'** Fraction of hexagonal cells as a function of time (B) and histogram of cell-coordination number (B') in the lateral ectoderm. The histograms show pooled data from the time periods 0–15 min and 45–50 min highlighted in B. Lines indicate the coordination number distributions for Voronoi tessellations generated from three different random point processes: hard disk (packing fraction 0.54 near the theoretical maximum for sequential placement [96]), Ginibre [95], and Poisson. **C** Hexatic order is low, and shows no long-range correlation. It further decreases as GBE progresses. Hue and brightness code for the phase $\arg \psi_6$ and magnitude $|\psi_6|$ of the hexatic order parameter, respectively.

law with an exponent that close to -0.75, a value found also for MDCK cells and in simulations using multiphase-field models [98]. (We find the same result using the distance-weighted hexatic order parameter introduced in Ref. [98].) At the end of GBE, the decay exponent is smaller than -1, indicating a complete lack of correlations in hexatic order between neighboring cells. This is expected from the high number of non-hexagonal cells at this stage (Fig. S10B, 50 min).

2 Additional simulation results

In this section we report additional results from the tissue scale simulations.

2.1 Shear modulus is required for tissue extension by active T1s

As argued in the main text, a non-zero cell-level shear modulus is required to extend tissue via active T1s. The tissue needs to be solid, not liquid, to extend against external resistance (such as the restoring force created by the deforming passive dorsal tissue). This can also be understood by considering a single intercalating quartet, as shown in Fig. 1B, bottom. A neighbor exchange results in a change in quartet aspect ratio, i.e. tissue extension, only if the shape of the cells remains round. To penalize deviation from roundness, a shear modulus is required. Indeed, within the scope of the symmetric lattice model presented in Fig. 4, it is possible to chose the interface lengths ℓ_1, ℓ_2 so that for any vertex angles, the cell centroids remain at fixed positions, even as the middle interface collapses.

Fig. S11 shows simulation data to support this claim. In a simulation where the cell shear modulus is zero, the tissue does not extend. Instead, cells deform and elongate along the direction of active stress. Running otherwise identical simulations with different cell-scale shear moduli shows that tissue extension decreases monotonically as the shear modulus is reduced. Recall that only the ratio of shear and bulk modulus is relevant to the simulation, so the bulk modulus is fixed to 1 by convention. Initially, the change in tissue extension is relatively weak (Fig. S11C). This also shows that the outcomes of our simulation are quite generic and only depend weakly on the elastic energy parameters. Below a certain value of shear modulus, the amount of tissue extension drops of rapidly, and vanishes approximately when the shear modulus is zero. This value is determined by the strength of the elasticity in the passive region. As discussed below in the section about simulation methods, we take the passive region to be 80% softer then the active region. If the shear modulus in the active region is greater than passive region elasticity, it is favorable to extend the germ band, preserving germ band cell isotropy, but stretching the passive region. If it is lower, it is energetically favorable to deform the cells in the germ band instead and there is little tissue extension.

2.2 Interface extension is independent of tissue extension

As argued in the main text, interface extension after active T1s is not driven by external forces (e.g. due to tissue elongation) but locally by cortical tensions. Active T1s are fundamentally asymmetric in time: the collapsing interface has high myosin levels, and the newly formed interface has very low levels. Since these low levels are insufficient to balance the tensions of the surrounding interfaces, the new interface extends.

Our simulations support the notion that interface extension does not depend on tissue extension, even though our simulations contain no additional active mechanisms to elongate new interfaces. In the main text, we showed simulations of a tissue geometry without a soft, passive region to compensate the convergence of the active tissue ("*toll[RM9]*"). Because of incompressibility, the active tissue also does not extend. Nevertheless, new interfaces elongate at rates very similar to control

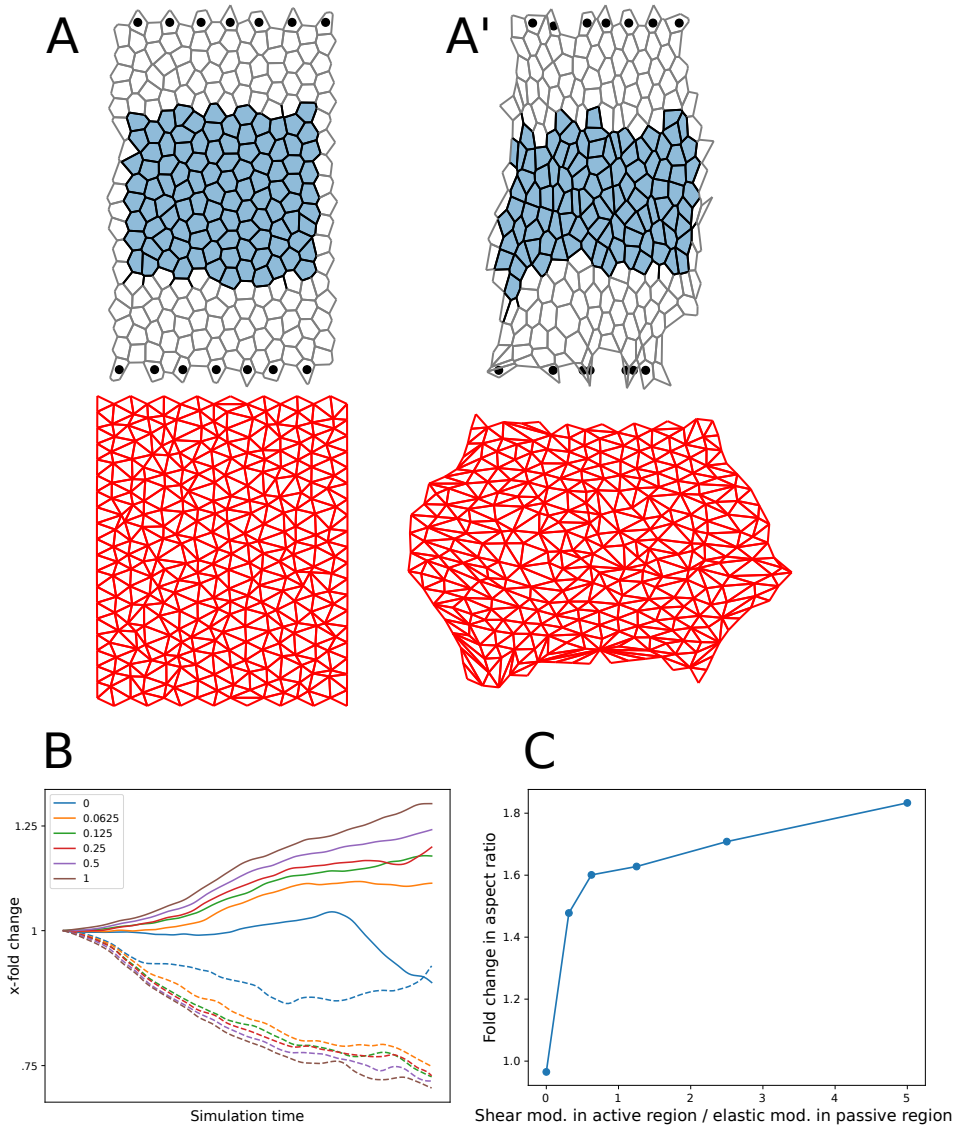

Figure S11: Cell-level shear modulus is required for tissue extension. **A and A'** Snapshots from a simulation where the cell-level shear modulus is set to 0. Tension triangulations (red) show that T1s take place and the triangulation elongates. However, no convergent extension takes place – instead, active T1s deform cells which elongate along the axis of active stress **B** x–fold change in active tissue height and length for otherwise identical simulation with varying shear moduli (shear modulus given as percentage of bulk modulus). The simulation geometry and initial condition is as depicted in A. **C** The amount of convergent extension decreases with weakening shear modulus. The tissue aspect ratio change, calculated from the final timepoint in B, vanishes if the cell level shear modulus is 0.

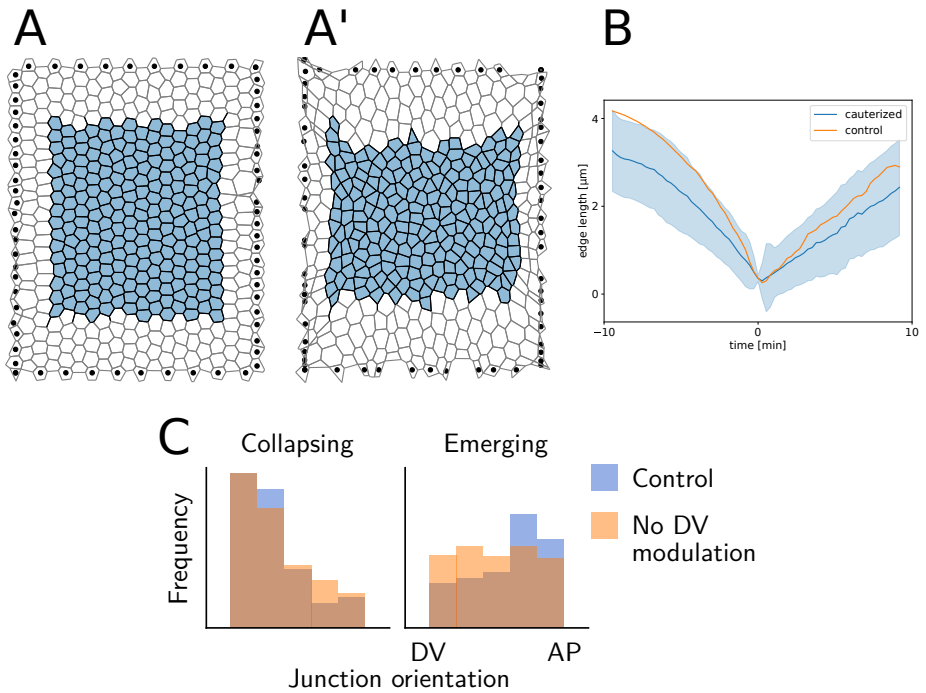

Figure S12: interfaces extend even if tissue extension is blocked. **A and A'** Snapshots from a simulation where tissue extension is blocked by slip walls along the AP boundaries of the tissue patch. This mimics experiments where the germ band is blocked from extending via cauterization of the ventral tissue close to the posterior pole, or mutations in the posterior midgut [29]. **B** Length vs time of collapsing interfaces in the simulation in A, and a control where no AP boundaries were imposed. Interface collapse and elongation are slightly slowed down, but new interfaces still successfully extend. **C** Orientation of collapsing and extending interfaces in simulations where tissue extension is blocked by abolishing DV modulation. K' The dynamics of junction length (Fig. 6J) and the orientation of contracting junctions are nearly identical between simulations with and without DV modulation of activity. The main difference between the two cases is the orientation of extending junctions which is strongly biased along AP in WT but has no bias in the absence of DV modulation.

simulations (Fig. 6). We now support this conclusion with an additional simulation. Mimicking experiments where tissue extension is blocked by a cauterization fence [29], we block tissue extension by adding slip walls along the AP boundaries of the tissue patch (Fig. S12A). For numerical reasons, we add a small passive zone in front of these additional boundaries, and enforce the slip-wall condition with a softer penalty than for the dorsal slip walls. This is done to avoid direct conflicts between the boundary conditions and the angle constraints from the triangulation. In these simulations, the active tissue does not extend, and cells deform to compensate T1s (Fig. S12A'). In a control simulation (not show), the tissue has elongated by 30% by the time shown in Fig. S12A'. However, new interfaces still successfully extend (Fig. S12B), like in the *toll[RM9]* simulations shown in Fig. 6. The overall speed of intercalations is slightly reduced because of the additional slip walls.

3 Isogonal shear and tissue shear modulus

As discussed in the main text, and shown in Fig. S11 our simulations show that a non-zero cell-level shear modulus is required for extension via active T1s. Here, we analyze the relation of cell-level and tissue-level shear modulus. Crucially, because of the dominance of cortical tensions, a tissue patch in our model will respond

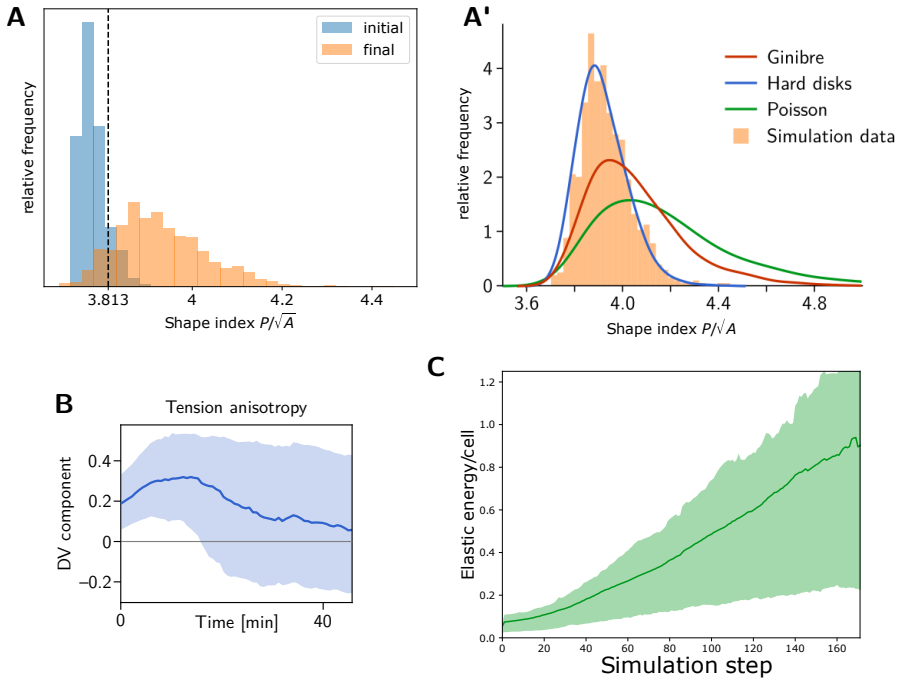

Figure S13: Additional data on tissue-scale simulations (Fig. 6). **A** Histogram of cell shape index in active region at the initial and final time points of the simulation shown in Fig. 6E-G. **A'** Random Voronoi tessellation explains asymptotic distribution of of cell shape index in simulations. The simulation data is the same shown in A. Lines show the shape index distributions for random Voronoi tessellations seeded with different random point processes: Poisson (green line), where points are independently and randomly placed in a given region; Ginibre (red line), where points repel with a Coulomb-like interaction [95]; and a hard-disk process (blue line) near the maximum packing fraction 0.547 [96]. The hard-disk process is the most physically sensible approximation of densely packed, non-intersecting cells and reproduces the distribution of cell shape indices observed in the simulation. **B** Median DV-DV component of the tension anisotropy tensor $\mathbb{T}$. Shaded bands shows quartiles. Initial anisotropy is first amplified by positive tension feedback but then decays as the cell packing becomes disordered. **C** Elastic energy of active cells in arbitrary units vs simulation iteration for the simulation shown in Fig. 6G. As tissue extension and intercalations proceed, minimizing the energy to zero becomes impossible due to disorder-induced frustration. In simulation we also observe increasingly slow convergence of elastic energy minimization as the simulation proceeds.

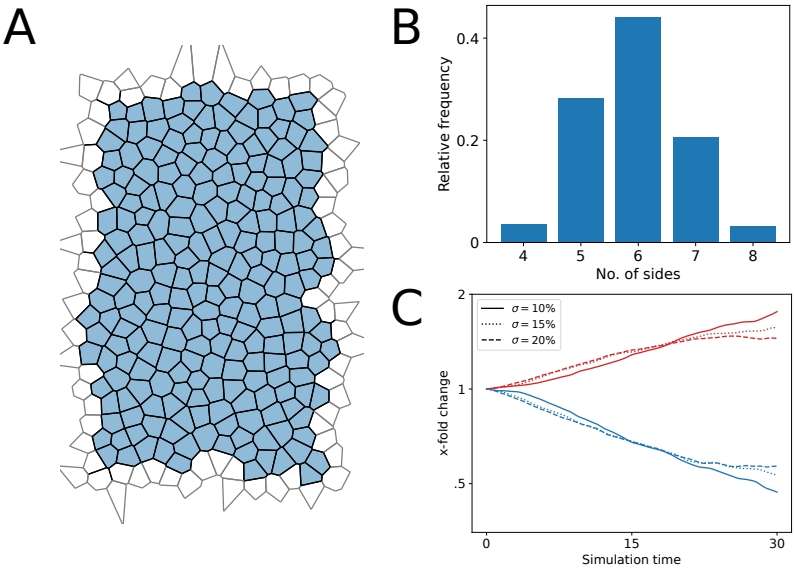

Figure S14: **A** Example of "disorderd" initial condition. We sample points using a Poisson hard-disk process at packing fraction ≈ 0.6 and compute the Delaunay triangulation to obtain the initial tension triangulation. **B** Fraction of n-sided cells in the mesh shown in (A). Compare with Fig. S10B'. **C** Noise in initial tensions has little impact on tissue extension as long as cells are six-sided. Extension vs time for simulations with free boundaries as in Fig. 6E. Initial conditions were created by taking triangular lattices in tension space (corresponding to cells forming a hexagonal lattice), and adding Gaussian noise to the vertex positions. Noise levels are expressed as $\mathrm{Std}(T_{ij})/\mathrm{Mean}(T_{ij})$ where T_{ij} are the interface lengths (all identical in the absence of noise). 20% noise is the maximum level of noise where the vast majority of cells are hexagonal ($> 90\%$).

to externally applied forces via an isogonal deformation. We first show that an isogonal deformation can create tissue-scale pure shear (on the level of cell centroid displacement – the transformation of cell vertices is necessarily non-affine to preserve angles). Then we show that these pure shear modes correspond to the response of the tissue to external force by computing the Hessian of our cell elastic energy in the subspace spanned by isogonal deformations, and measure the shear modulus.

3.1 Quadratic isogonal mode profile creates pure shear

To show that isogonal modes can create pure shear, not just dilation/contraction of cells, we make use of the isogonal mode parametrization introduced in Ref. [13]. It assigns an isogonal "potential" Θ_i to each cell, and calculates the cell displacements from the Θ_i and the edge tension vectors. In the following, we will show that a constant gradient in the isogonal potential generates a uniform translation in real space. By integration, this implies that a quadratic spatial profile of the isogonal potential creates a pure shear.

Let us identify the real space edge unit vectors by the two adjacent cells $\mathbf{e}_{ij} = -\mathbf{e}_{ji}$ and denote the corresponding tensions as T_{ij}. Then the tension vectors $\hat{\mathbf{T}}_{ij} = T_{ij}\hat{\mathbf{e}}_{ij}$ form a triangulation, where $\hat{\mathbf{a}}$ denotes the normal vector to $\mathbf{a}$, i.e. $\hat{\mathbf{a}}.\mathbf{a} = 0$ and $||\hat{\mathbf{a}}|| = ||\mathbf{a}||$.

The isogonal displacement $\mathbf{u}_{ijk}$ of the real space vertices $\mathbf{r}_{ijk}$ (identified by the three adjacent cells) is given by

$$\mathbf{r}_{ijk} \to \mathbf{r}_{ijk} + \mathbf{u}_{ijk} = \mathbf{r}_{ijk} + \frac{1}{S_{ijk}}\big[\Theta_i \mathbf{T}_{jk} + (\text{cyc.})\big] \tag{25}$$

where $S_{ijk} = \hat{\mathbf{T}}_{ij}.\mathbf{T}_{ik}$ is the area of the tension triangle (ijk).

First, observe that the uniform isogonal mode $\Theta_i = \text{const.}$ has no effect on the vertex positions because

$$\mathbf{T}_{jk} + \mathbf{T}_{ki} + \mathbf{T}_{jk} = 0 \quad \text{(force balance)}. \tag{26}$$

Now we aim to show that a constant gradient in Θ_i drives a uniform displacement of the $\mathbf{r}_{ijk}$. Specifically, by uniform gradient we mean $\Theta_i = \mathbf{t}_i.\mathbf{a}$, i.e. a linear gradient in the tension space ($\mathbf{t}_i$ is the position of the tension triangulation vertex corresponding to cell i, such that $\hat{\mathbf{T}}_{ij} = \mathbf{t}_j - \mathbf{t}_i$). To show that the displacement in real space is uniform, it is enough to show that two adjacent vertices are displaced identically. By induction, this implies that all displacements are identical. It is therefore sufficient to consider a quartet of cells ($i = 1--4$), corresponding to a "kite" in tension space (note that $\hat{\mathbf{a}}.\mathbf{b}$ is identical to the wedge product $\mathbf{a} \wedge \mathbf{b}$.)

Because a constant can be arbitrarily added to all Θ_i, we can set $\Theta_1 = 0$ and thus have $\Theta_i = \hat{\mathbf{T}}_{ij}.\mathbf{a}$ for $i = 2, 3, 4$. The displacements now read

$$\mathbf{u}_{123} = \frac{1}{S_{123}}\big(\hat{\mathbf{T}}_{12}.\mathbf{a}\ \mathbf{T}_{31} + \hat{\mathbf{T}}_{13}.\mathbf{a}\ \mathbf{T}_{12}\big) \tag{27}$$

$$\mathbf{u}_{134} = \frac{1}{S_{134}}\big(\hat{\mathbf{T}}_{13}.\mathbf{a}\ \mathbf{T}_{41} + \hat{\mathbf{T}}_{14}.\mathbf{a}\ \mathbf{T}_{13}\big) \tag{28}$$

To show that these displacements are identical, we project them onto two conveniently chosen, linearly independent vectors, namely $\hat{\mathbf{T}}_{12}$ and $\hat{\mathbf{T}}_{13}$. For the latter we find

$$\hat{\mathbf{T}}_{13}.\mathbf{u}_{123} = \frac{1}{S_{123}}\hat{\mathbf{T}}_{13}.\mathbf{a}\ \hat{\mathbf{T}}_{13}.\mathbf{T}_{12} = -\hat{\mathbf{T}}_{13}.\mathbf{a}, \tag{29}$$

$$\hat{\mathbf{T}}_{13}.\mathbf{u}_{134} = \frac{1}{S_{134}} - \hat{\mathbf{T}}_{13}.\mathbf{a}\ \hat{\mathbf{T}}_{13}.\mathbf{T}_{14} = -\hat{\mathbf{T}}_{13}.\mathbf{a}, \tag{30}$$

where we used that $\hat{\mathbf{T}}_{ij}.\mathbf{T}_{ij} = 0$ and applied the definition of S_{ijk}.

Projecting (27) and (28) onto $\hat{\mathbf{T}}_{12}$ gives

$$\hat{\mathbf{T}}_{12}.\mathbf{u}_{123} = \frac{1}{S_{123}} \hat{\mathbf{T}}_{12}.\mathbf{a}\ \hat{\mathbf{T}}_{12}.\mathbf{T}_{31} = -\hat{\mathbf{T}}_{12}.\mathbf{a} \tag{31}$$

$$\hat{\mathbf{T}}_{12}.\mathbf{u}_{134} = \frac{1}{S_{134}} \big(\hat{\mathbf{T}}_{13}.\mathbf{a}\ \hat{\mathbf{T}}_{12}.\mathbf{T}_{41} + \hat{\mathbf{T}}_{14}.\mathbf{a}\ \hat{\mathbf{T}}_{12}.\mathbf{T}_{13}\big) \tag{32}$$

To show equality of these two right-hand sides, we use that given $\hat{\mathbf{T}}_{13}.\mathbf{a}$ and $\hat{\mathbf{T}}_{14}.\mathbf{a}$ we can find $\mathbf{a}$ and substitute the result into $\hat{\mathbf{T}}_{12}.\mathbf{a}$. We start by "expanding the identity"

$$\begin{pmatrix} — \hat{\mathbf{T}}_{13} — \\ — \hat{\mathbf{T}}_{14} — \end{pmatrix} \mathbf{a} = \begin{pmatrix} \hat{\mathbf{T}}_{13}.\mathbf{a} \\ \hat{\mathbf{T}}_{14}.\mathbf{a} \end{pmatrix} \quad \Rightarrow \quad \mathbf{a} = \begin{pmatrix} — \hat{\mathbf{T}}_{13} — \\ — \hat{\mathbf{T}}_{14} — \end{pmatrix}^{-1} \begin{pmatrix} \hat{\mathbf{T}}_{13}.\mathbf{a} \\ \hat{\mathbf{T}}_{14}.\mathbf{a} \end{pmatrix} \tag{33}$$

Explicitly writing out the inverse matrix then gives

$$\mathbf{a} = \frac{1}{\hat{\mathbf{T}}_{13}.\mathbf{T}_{14}} \begin{pmatrix} | & | \\ \mathbf{T}_{14} & -\mathbf{T}_{13} \\ | & | \end{pmatrix} \begin{pmatrix} \hat{\mathbf{T}}_{13}.\mathbf{a} \\ \hat{\mathbf{T}}_{14}.\mathbf{a} \end{pmatrix} \tag{34}$$

With this, we find the relation

$$\hat{\mathbf{T}}_{12}.\mathbf{a} = -\frac{1}{S_{134}} \big(\hat{\mathbf{T}}_{12}.\mathbf{T}_{41}\ \hat{\mathbf{T}}_{13}.\mathbf{a} + \hat{\mathbf{T}}_{12}.\mathbf{T}_{13}\ \hat{\mathbf{T}}_{14}.\mathbf{a}\big) \tag{35}$$

where we used $\mathbf{T}_{ij} = -\mathbf{T}_{jk}$ to flip the indices on $\mathbf{T}_{14}$. Comparing to (31) and (32) now shows the identity of their RHSs.

Taken together, we have shown that

$$\hat{\mathbf{T}}_{12}.\mathbf{u}_{123} = \hat{\mathbf{T}}_{12}.\mathbf{u}_{134} \quad \text{and} \quad \hat{\mathbf{T}}_{13}.\mathbf{u}_{123} = \hat{\mathbf{T}}_{13}.\mathbf{u}_{134}, \tag{36}$$

Because $\hat{\mathbf{T}}_{12}$ and $\hat{\mathbf{T}}_{13}$ are linearly independent, it follows that $\mathbf{u}_{123} = \mathbf{u}_{134}$. QED.

We just showed that a constant gradient in Θ_i corresponds to a uniform displacement of the real space vertices $\mathbf{r}_{ijk}$. We can therefore think of $\Theta(\mathbf{t})$ as a "potential" for the isogonal displacement field: $\mathbf{u} \approx \nabla_{\mathbf{t}}\Theta$, where the approximation is valid for slowly varying gradients and exact for constant gradients. The gradient $\nabla_{\mathbf{t}}$ is taken in *tension space* because the function $\Theta(\mathbf{t}_i) = \Theta_i$ is defined on the vertices of the tension triangulation $\mathbf{t}_i$.

A pure shear aligned with the coordinate axes is given by a displacement field $\mathbf{u}(\mathbf{r}) = \varepsilon\ \mathrm{diag}\,(1, -1).\mathbf{r}$ and is therefore generated (approximately) by a quadratic isogonal potential $\Theta = \varepsilon\ \mathbf{t}^{\mathrm{T}}.\mathrm{diag}\,(-1, 1).\mathbf{t} = \varepsilon\,[(t^1)^2 - (t^2)^2]$.

3.2 Isogonal Hessian and tissue-scale shear modulus

Above we have shown that isogonal modes can create a pure shear (on the level of cell centroids). We now show that the tissue will respond to external forces by such an isogonal shear. To do this, we assume that the tissue is initially at the elastic energy minimum under the constraints of a given tension tension triangulation. In this case, we can approximate the energy E by a quadratic function of displacement by computing the Hessian. Since the tissue has to deform under the angle constraints defined by the triangulation, only isogonal displacements are allowed, and we will project the the Hessian onto the space of isogonal modes. The lowest eigenvectors of the isogonal Hessian will then correspond to the modes excited by external forcing.

The isogonal unit vectors convert the isogonal potentials into real-space displacement of vertices: the isogonal potential Θ_j at cell j contributes a term $\Theta_j \mathbf{I}_j^{jkl}$ to the displacement of vertex $\mathbf{r}_{jkl}$ adjacent to j. The $\mathbf{I}_j^{jkl}$ are defined above in Eq. (25). The isogonal Hessian reads:

$$\mathcal{H}_{il} = \sum_{(jk),(mn)} \mathbf{I}_i^{ijk} \frac{\partial^2 E(\{\mathbf{r}_{abc}\})}{\partial \mathbf{r}_{ijk} \partial \mathbf{r}_{lmn}} \mathbf{I}_l^{lmn} \tag{37}$$

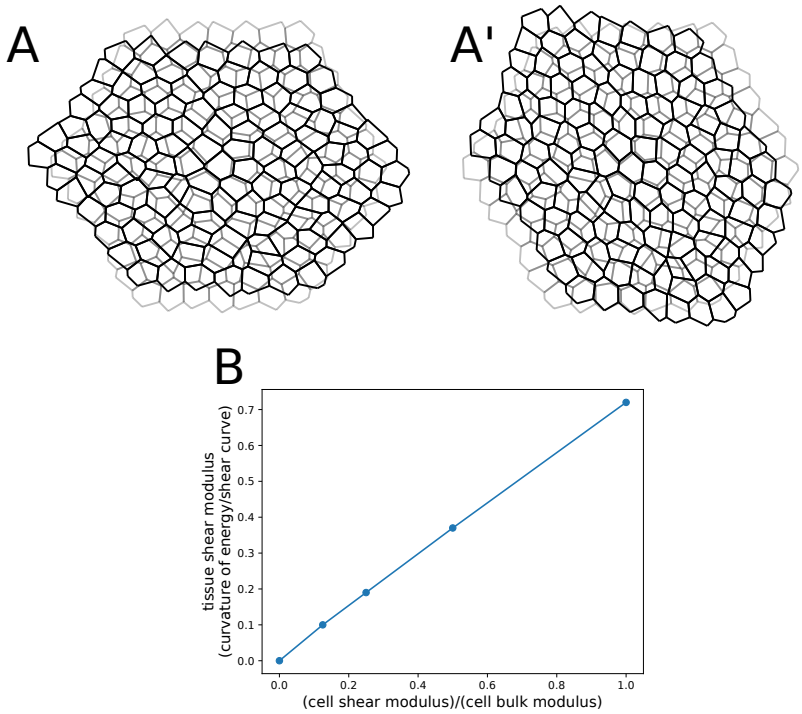

Figure S15: Isogonal Hessian sets tissue scale shear modulus. **A-A'** The two lowest non-trivial eigenmodes of the isogonal Hessian correspond to pure shear. Reference configuration (minimum energy for given tension triangulation, light grey) and configuration deformed according to the isogonal Hessian eigenvector for the two shear eigenmodes in an example mesh. **B** Tissue level is proportional to cell level shear. Tissue level shear modulus (isogonal determined by Hessian eigenvalue) vs cell-level shear modulus for the tissue patch shown in A.

With the same code used for the tissue-scale simulations, we can numerically construct and diagonalize $\mathcal{H}_{il}$. There are 3 trivial 0-modes which correspond to two real-space translations and a globally constant isogonal parameter, which creates no cell displacement. This is in accordance with the results from above and the fact that the E only depends on differences in vertex positions. We find that the two lowest non-trivial modes are pure shear modes (quadratically varying isogonal potential Θ_i). They are shown for an example lattice in Fig. S15. Finding pure shear modes is not unexpected since they minimize the variation in vertex displacement across the tissue, and the energy function E is convex (quadratic).

External forces, e.g. external shear, will excite the lowest eigenmodes of the Hessian. The energy cost is determined by the Hessian eigenvalues, which therefore define the shear modulus. In the example shown in Fig. S15 the eigenvalues of the shear modes are 2 orders of magnitude smaller than the next eigenvalues. The highest eigenvalues correspond to isogonal deformations localized to a single quartet. The shear modulus can then be read of by the change in energy by a perturbation along the lowest eigenvectors. The curvature of this parabola (determined by the eigenvalue and a conversion factor which translates isogonal parameters into real-space shear) is the tissue-scale shear modulus. We can then investigate how the tissue-scale shear modulus depends on the cell-level shear modulus in the elastic energy. As expected, we find that the two are proportional.

4 Simulation methods

In the following, we explain the simulations presented in the paper and provide the modeling and implementation details. These comprise the mean-field calculation of the dynamics of the distribution of vertex angles, the symmetric lattice of a single intercalating quartet, and the tissue-scale simulation of a disordered epithelial tissue comprising both active and passive regions. All code used to create and analyse the simulations is available on GitHub https://github.com/nikolas-claussen/CE_simulation_public.

4.1 Positive feedback tension dynamics and mean field simulation

In Figure 5G we show the dynamics of the distribution of vertex angles predicted by a positive tension feedback model. Under this model, the edge tensions T_i, $i = 1{-}3$, at a vertex evolve according to:

$$\tau_{\mathrm{T}} \dot{T}_i = T_i^n - \frac{1}{3} \sum_k T_k^n \tag{38}$$

where $n > 1$ and τ_{T} is a time scale converting simulation time into minutes (fit to the data).

We can reformulate the above dynamics of a tension triangle in terms of the its angles and circumcircle radius. The tensions at a vertex form a triangle with angles ϕ_i, which are related to the tensions by $T_i = 2R\sin(\phi_i)$, where R is the triangle circumcircle. The induced dynamics for the angles is

$$\tau_{\mathrm{T}} \dot{\phi}_i = (2R)^{n-1} \tan\phi_i \left[\sin(\phi_i)^{n-1} - \frac{\sum_j \sin(\phi_j)^{n-1} \tan\phi_j}{\sum_j \tan\phi_j} \right] \tag{39}$$

Note that the dynamics of R does not affect the trajectories of the flow Eq. (39). In the lattice model, R is defined by the constraint that the triangle perimeter P is fixed (corresponding to a finite total myosin pool)

$$R = \frac{P}{2\sum_i \sin(\phi_i)} \tag{40}$$

We integrated Eq. (39) using a 4th order Runge-Kutta method as implemented in the `SciPy` software package [99], using as initial conditions the vertex angles in the experimental data at time $t = 5$ min (the vertex angles from the data were temporally smoothed with a window of 2 min to reduce noise). From our simulation, we computed the triangle shape parameter to compare the marginals with the experimental data.

Dynamics in the triangle shape space. To find the trajectories in the triangle shape, we integrated Eq. (39). A change of variables from angles to the triangle shape space yields the flow shown in Fig. 5J'. To model the effect of intercalations, which remove highly obtuse tension triangles from the distribution, we stopped integration once the maximum relative tension increased over 1.6, approximately maximum collapse angle observed in the data. Collapsed triangles were removed from the simulation ensemble. The ~~Hill~~ exponent n was chosen to equal $n = 4$. Different values give very similar results, so no systematic optimization was performed.

4.2 Force balance and cortical tension dominance

Our models for both single quartets and whole tissues are based on two assumptions: adiabatic force balance, and dominance of cortical tensions. The first assumption means that we obtain the cell geometry by solving force-balance equations. The

second assumption means the we do so in two steps: first, we determine the interface angles from the cortical tension force balance. The remaining forces in the system are much weaker than cortical tensions and only affect the residual degrees of freedom, the isogonal modes.

This can be phrased in terms of dissipative dynamics with a certain energy function:

$$E(\{\mathbf{r}_{ijk}\}|\{T_{ij}\}) = \sum_{ij} T_{ij} r_{ij} + \epsilon E_{\mathcal{C}}(\mathbf{r}_{ijk}) \tag{41}$$

Here, $\mathbf{r}_{ijk}$ are the vertex positions, indexed by the surrounding cells ijk. The cortical tensions T_{ij} enter the energy as time-dependent parameters. The small parameter ϵ represents the separation of scales between cortical tensions and the cell elastic energy $E_{\mathcal{C}}$. Force balance implies

$$\frac{\partial E}{\partial \mathbf{r}_{ijk}} = 0 \tag{42}$$

This equations is first solved to for the vertex angles (0th order in ϵ) – this implies that the real-space and tension triangle angles have to be complementary. Then, the cell elastic energy is minimized under the constraint of fixed angles. The dynamics of the model is then entirely determined by the (slow) dynamics of the energy parameters, the tensions $T_{ij}(t)$, which represent the biological control parameters. The key element of the simulations are therefore the tension triangulations.

4.3 Cell shape elasticity and single-quartet model

In Fig. 4, we present a model of a single intercalating quartet. As explained in the main text, we calculate the dynamics a representative quartet in a regular lattice, i.e. a periodic cell array, characterized by the three angles at each vertex, ϕ_i, and the three interface lengths ℓ_i, with $i \in \{0, 1, 2\}$. The dynamics of the angles ϕ_i are obtained by integrating the excitable-tension feedback Eq. (39).

Cell shape energy. To determine the lengths ℓ_i, and thereby the isogonal modes, we use an elastic energy based on the the cell shape tensor

$$S_{\mathcal{C}} = \sum_i \frac{\mathbf{e}_i \otimes \mathbf{e}_i}{\ell_i} \tag{43}$$

where i runs over the edges of the cell $\mathcal{C}$, and $\mathbf{e}_i$ is the vector pointing from one vertex of the interface to the other. Note that in this shape tensor, each edge contributes linearly in length to the cell shape. This means that artificially subdividing an edge has no effect on the cell shape tensor. This makes sense if we assume that the elasticity we aim to model using S resides in the cell interior (incompressibility, microtubules, intermediate filaments, nucleus). The shape tensor can also be defined using vectors from the cell centroid to its vertices (in the lattice, the two definitions are equivalent). An alternative definition of the elastic energy using $\tilde{S}_{\mathcal{C}} = \sum_i \mathbf{e}_i \otimes \mathbf{e}_i$ instead gives broadly similar results (although interface collapse happens more abruptly, because of the higher order non-linearity).

We assign a reference shape S_0 and define the cell elastic energy via

$$E_{\mathcal{C}} = \lambda[\mathrm{Tr}(S_{\mathcal{C}} - S_0)]^2 + \mu \mathrm{Tr}[(S_{\mathcal{C}} - S_0)^2] \tag{44}$$

with bulk modulus λ and shear modulus μ. We used a shear/bulk ration of $\mu/\lambda = 0.1$. Because of the separation of scales between cortical tensions and elastic energy baked into the model, the absolute values of λ, μ are irrelvant. Further, for the case of active T1s, the results do not depend on μ/λ, as long as $\mu > 0$.

The edge lengths ℓ_i are then fixed by minimizing the elastic energy Eq. (44) for the angles determined by the tension dynamics. Strikingly, within the single-quartet model, the "shape strain" $S_{\mathcal{C}} - S_0$ can always be set to 0 by choice of the edge

lengths, and the energy $E_{\mathcal{C}} = 0$ throughout. This can already be seen from a degree-of-freedom count (three ℓ_i for the three independent components of $S_{\mathcal{C}} - S_0$). The elastic energy therefore acts only on the isogonal modes (i.e. $\partial_{\phi_i} E_{\mathcal{C}}|_{\ell_i=\text{minimizers}} = 0$) and there is no energy barrier for intercalations. Consequently, there is no need for noise to drive intercalations in our model. By contrast, for the widely-used area-perimeter elastic energy $E = (A-A_0)^2+(P-P_0)^2$ (where A, P are the cell area and perimeter, and A_0, P_0 their target values) [55], there exists an energy barrier, and the inner interface ℓ_0 only collapses when $\phi_0 = \pi$. This is shown in Fig. S16B. Note that the area-perimeter energy is a special case because of the geometric incompatibility of area and perimeter constraints. Combining area elasticity with shear elasticity based on the shape tensor, $E = (A-A_0)^2+\mu\text{Tr}[(S_{\mathcal{C}}-S_0)^2]$, (or perimeter elasticity with cell shape bulk elasticity) leads to similar results as Eq. (44). Note also that because of the degree-of-freedom count, the system is under-specified if the shear modulus is 0, foreshadowing the fact that without shear modulus, no convergence-extension takes place.

The reference shape S_0 therefore encodes, in a sense, the isogonal mode. An isotropic $S_0 \propto \text{Id}$ favours equilateral hexagons. We chose a slightly anisotropic reference shape S_0 (20% anisotropy) to model the isogonal stretching caused by the ventral furrow before onset of GBE. This anisotropy sets the angle at which the inner interface collapses, $\ell_0 = 0$. The experimental value of the collapse tension was therefore used to fit the S_0-anisotropy.

Myosin handover and passive tension. As shown in Fig. 4D, we propose a myosin handover mechanism to explain the extension of the new interface post intercalation. A interface with cortical tension T is comprised of the adherens-junctional actomyosin cortex of the two adjacent cells, which are coupled mechanically via adherens junctions. Under force balance, the total tension T has to be constant along the cortex, but the individual tensions on either side can be non-uniform, as the resulting traction forces are exchanged via adherens junctions. In the following, we assume as a first order approximation that the level of active tension (i.e. myosin concentration) varies linearly along an interface (similar calculations have been performed in Ref. [57] to calculate interfacial shear stress). This allows us to geometrically obtain the myosin concentration at the individual cortices that will form the two juxtaposed sides of the new interface (see Fig 4D).

Consider a vertex, where interfaces $i = 0, 1, 2$ (with tensions T_0, T_1, T_2) meet, and let 0 be the interface about to collapse. The three cells that meet at the vertex will be referred to by $(01), (12), (21)$ (where e.g. (01) is the cell abutting interfaces 0 and 1). Let m_{01}, m_{12}, m_{21} be the motor molecule concentrations (in units of tension) at the vertex in the junctional cortices of the three cells. Then, the tensions are related to the motor molecule concentrations as:

$$\begin{aligned} T_0 &= m_{21} + m_{01} \\ T_1 &= m_{01} + m_{12} \\ T_2 &= m_{12} + m_{21} \end{aligned}$$

This uses the assumption of myosin continuity at vertices, and the fact that the tension on an interface is the sum of the tensions of the two cortices that make it up. The motor molecule concentration on the cortex belonging to the new interfaces, post collapse, will be equal to m_{12}. Solving for this in terms of the tensions:

$$m_{12} = \frac{T_1 + T_2 - T_0}{2} \tag{45}$$

The new interface consists of two cortices, coming from the two vertices of the old junction. Let the tensions at the two triangles be T_0, T_1, T_2 and T_0, T_1', T_2'. Define $T_n, T_{n,a}, T_{p,a}$ to be the total, active, and passive, tensions on the new junction.

This active tension is generally not sufficient to balance the total tension on the new edge, leading to a non-zero passive tension right after intercalation:

$$T_{p,a} = T_n - T_{n,a} = T_n - (m_{12} + m'_{12}) = T_n - \left(\frac{T_1 + T_2 + T'_1 + T'_2}{2} - T_0 \right) \quad (46)$$

For example, if a perfectly symmetric quartet collapses when the vertex angle facing the collapsing edge is 90°, $T_1 = T_2 = T'_1 = T'_2 = 1$ and $T_0 = T_n = \sqrt{2}$. Therefore, $T_{a,n} = 2 - \sqrt{2} \approx 0.6$ and $T_{p,n} = \sqrt{2} - (2 - \sqrt{2}) \approx 0.8$.

Note that by the triangle inequality, for any convex quadrilateral with perimeter P and diagonals D_1, D_2, one has $P/2 \leq D_1 + D_2 \leq P$. Applying this to the quadrilateral formed by the two tension triangles at the collapsing interface, we get $T_{a,n} \geq 0$ and $T_{p,n} \geq 0$: the handover formula always results in positive active and passive tensions.

The passive tension subsequently relaxes visco-elastically with rate τ_p^{-1}: $\dot{T}_p = -\tau_p^{-1} T_p$. Combining this with the feedback equation, the evolution of the total tension is

$$\dot{T} = \tau_T^{-1} (T - T_p)^n - \tau_p^{-1} T_p \quad (47)$$

where we assumed that the positive feedback only operates on the active tension. The relaxation time scale was chosen at $\tau_p = 2\tau_T$, which fits the observed decay of tension post T1.

Simulation details. In our simulations, we triggered an intercalation event once the collapsing edge length, as determined by energy minimization, reached 0. We then initialized the passive tension as given by Eq. (46) and simulated the combined active/passive tension dynamics. The relaxation rate τ_p was fit to the measured tension decay post intercalation. The overall time- and length-scale were likewise fit to the data. The feedback exponent was $n = 4$ as in the mean-field simulation. The initial conditions were drawn from the initial vertex-angles observed in the data, as in the mean-field simulation. Numerically, energy minimization was carried out using the `scipy.optimize` package, specifically its Nelder-Mead optimizer.

Passive intercalation. Within the same framework, we can also model passive intercalations, shown in Fig. 4F. We can either specify cortical tension dynamics (in this case, tension homeostasis, $\dot{T} \sim -(T - 1)$) and then minimize an elastic energy that includes the influence of externally imposed shear. This will trivially reproduce the isogonal behavior shown in Fig. 2E. Alternatively one can reason that on the dorsal side there is very little active tension (cortical myosin), so that cortical tensions are expected to be low. Then, the passive elastic energy, together with the imposed shear, should determine the also angles. Both models are consistent with the data.

In Fig. 4F, we show simulations based on the latter option. We implement the externally imposed shear causing the passive intercalations as follows. We calculate the four cell centroids $\mathbf{c}_i$ of the cell quartets, and demand that at simulation time t

$$\mathbf{c}_i(t) = S(t).\mathbf{c}_i(t = 0) \quad (48)$$

where $S(t)$ is a diagonal matrix representing (area-preserving) shear, increasing over time with constant shear rate γ.

We then minimize the elastic energy under the constraint (numerically, this is done by adding a penalty term to the elastic energy), but this time with respect to both the lengths ℓ_i and the angles ϕ_i. As long as the shear modulus $\mu \ll \lambda$, this procedure results in approximately isogonal behavior. To obtain continuity across the intercalation, the rest shape S_0 needs to be adjusted. Otherwise, post intercalation, the cell quartet jumps back to a hexagonal lattice configuration. This can be done by introducing a viscous relaxation scale for the rest shape; for simplicity, we

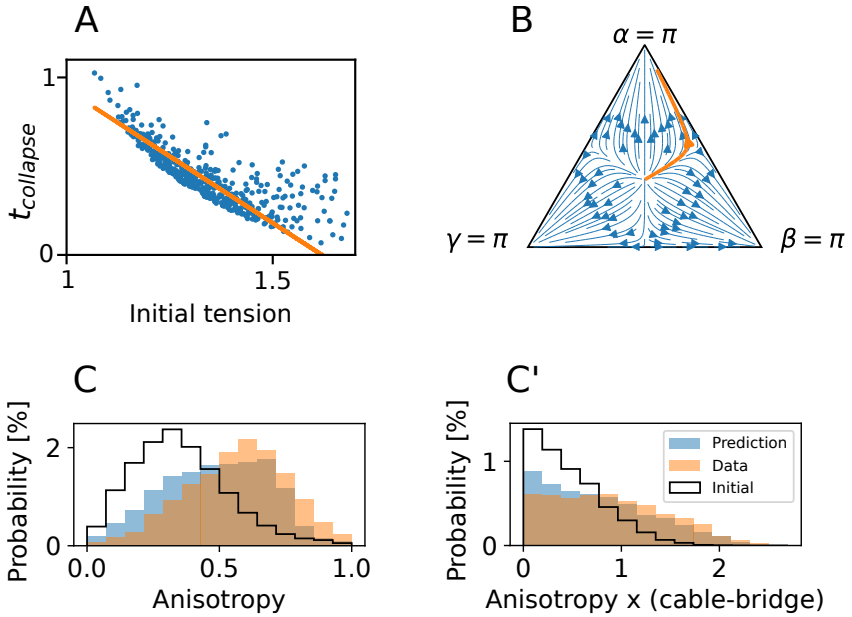

Figure S16: Additional figures on mean-field simulations. **A** Time in minutes to interface collapse vs initial relative tension in mean field model. Compare to the data shown in Fig. 2K. For this figure, we simulated positive feedback tension dynamics ($\dot{T} \sim T^4$) for individual kites. The initial kite angles were taken from the data before the onset of tissue elongation. Edge collapse was defined to occur when the relative tension of the central interface in the kite reached the experimentally determined critical tension, shown in Fig.2D. **B** Flow defined by positive feedback tension dynamics ($\dot{T} \sim T^4$) in the space of triangles parametrized by barycentric coordinates. This is an alternative representation of the flow show in Fig. 5J'. A triangle is defined by three angles α, β, γ under the constraint $\alpha+\beta+\gamma = \pi$ and $\alpha, \beta, \gamma > 0$. The figure shows the 2-simplex (equilateral triangle) defined by these constraints, which parametrizes all possible triangles. The corners correspond to degenerate triangles with angles $(\pi, 0, 0)$, and the center to the equilateral triangle. The flow leads from the equilateral fixed point to more and more obtuse triangles. **C-C'** Marginal distributions corresponding to the 2D histograms show in Fig. 5G,K. The histograms show the distributions of anisotropy (C) and the product of anisotropy and value along the cable-bridge axis (C') for the data at 0 minutes, the data at 25 min, and the prediction from the simulation of an ensemble of individual triangles starting from the experimentally observed tension triangles at 0 min.

simply set the rest shape to the current shape tensor at the time of intercalation. The initial conditions are obtained by varying the angle between the shear axis and the collapsing interface orientation from $0° - 25°$.

4.4 Tissue scale simulation

Using the components of the single-quartet simulation, we now describe a simulation of an arbitrary, disordered tissue patch. The key assumption are again adiabatic force balance and cortical tension dominance: the tissue geometry is found by solving for force balance, by first finding the angles from the cortical tensions and then the isogonal mode by minimizing cell elastic energy. The key quantity is the tension triangulation whose dynamics determines the tissue dynamics.

Conceptually, there is one main novel element: since the tension triangulation is now disordered and comprises many heterogeneous tension triangles, an additional mechanism is required to ensure the tension triangles fit together to a global triangulation. Further, the higher computational load requires different numerical methods.

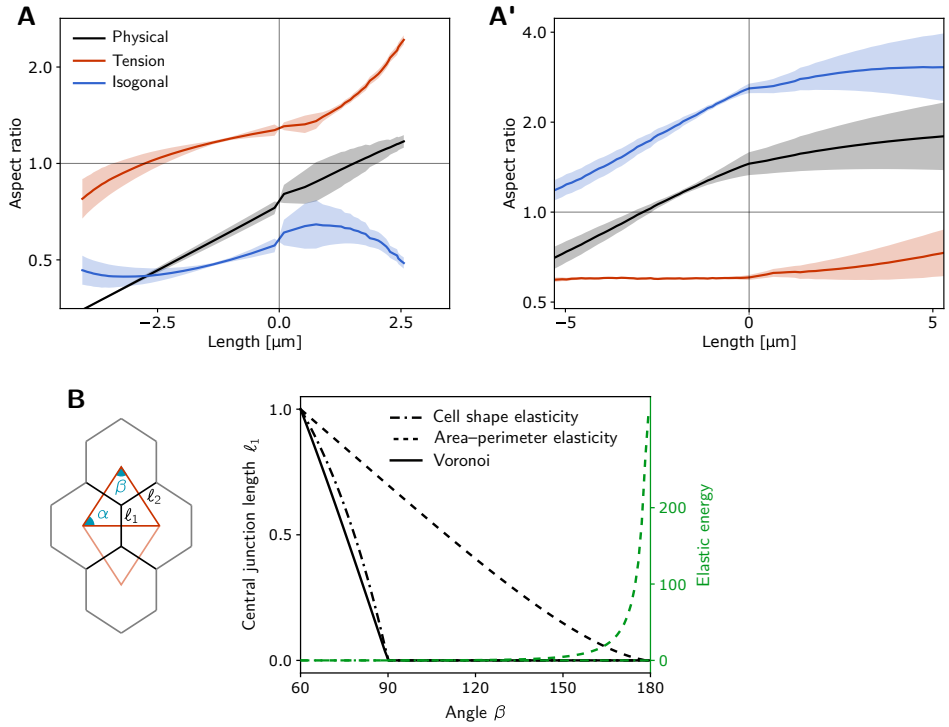

Figure S17: Additional figures on single-quartet simulations. **A and A'** Tension-isogonal decomposition of intercalations in single-quartet model. Physical, Voronoi, and isogonal aspect ratios for the single quartet simulations shown in Fig. 4E-F. Panel A shows the case of active intercalations, panel B the case of passive intercalations. **B** Length of the central interface in a quartet for a prescribed isosceles tension triangle parametrized by the angle β (the isosceles property implies $\alpha = (\pi - \beta)/2$). The solid line shows the interface length in the Voronoi tessellation ℓ_{ref} (cf. Eq. (13)). The interface length obtained by minimizing elastic energy Eq. (3) with isotropic target shape (dot-dashed line) closely follows the Voronoi length and vanishes at the same critical angle. By contrast, minimizing the "area–perimeter" energy of the vertex-model $E_{\mathrm{cell}} \sim (A - A_0)^2 + (P - P_0)^2$ gives a interface length (dashed black line) that vanishes only for $\beta \to \pi$ and the energy diverges in this limit (dashed green line).

Data structure. We model a piece of epithelial tissue by a polygonal tiling of the plane, polygons corresponding to cells. Two cells are neighbors if they are share an edge (this implies that the cell adjacency graph is a triangulation).

Following the idea of the dual tension triangulation introduced in the main text, a polygonal tiling is represented by a triangular mesh, in which cells are represented by vertices, cell edges by triangulation edges, and cell vertices by triangulation faces. Vertices, edges, and faces have the following attributes which are used for time evolution:

- Vertices: dual coordinates, the x, y coordinates of the vertex in the tension triangulation which will be denoted $\mathbf{t}_i$, and the reference shape g_0 for the shape-tensor elastic energy.
- Edges: the active and passive tensions on an edge.
- Faces: primal coordinates, the x, y coordinates of the vertex in the cell tessellation corresponding to the face, denoted $\mathbf{r}_{ijk}$.

As a reminder, given the dual coordinates of two adjacent vertices $\mathbf{t}_i, \mathbf{t}_j$, the tension on the edge connecting cells i, j is $T_{ij} = |\mathbf{t}_i - \mathbf{t}_j|$. The dual coordinates encode a configuration of balanced cortical tensions. Note that the primal (cell) and dual (tension) coordinates live in different spaces, and the overall scale of the tension coordinates is irrelevant.

The mesh is implemented in object oriented python, using a half-edge mesh data structure [100]. A half-edge mesh consists of vertices, faces, and, for each edge, two oriented half-edges. A half-edges stores a reference to the `next` half-edge on the counter-clockwise oriented face it belongs to, and a reference to its `twin`, the half-edge with opposite orientation on the adjacent face. This structure defines an orientation for every triangular face and makes mesh traversal (e.g. get all vertices of a cell) and mesh modification (e.g. intercalations) very convenient.

Overview. Due to the assumption of adiabatic force balance, the tissue geometry is determined by the instantaneous tensions. The dynamics is therefore determined by the change in the tension triangulation (due to positive feedback). In detail, the time evolution in our simulation is done in three steps:

1. Local Euler step: For each triangular face, update the active tensions according to positive tension feedback, and the passive tensions and the rest shape according to viscous relaxation.
2. Triangulation flattening: Optimize the dual vertex positions so that the lengths of each half-edge is as close as possible to its internally stored tension. This ensures global tension balance.
3. Cell shape optimization: Optimize the primal vertex positions to minimize the shape-tensor based elastic energy, while constraining the angles by the dual triangulation.
4. Topological modifications: Check if any primal edge has collapsed and carry out intercalations if necessary, re-initializing the active and passive tensions on the new edge.

The next sections describe them in detail. The most complicated and time-consuming of them is the cell shape optimization. Overall, a simulation of convergent extension of ~ 1000 cells takes approx. 15 minutes on a current-generation laptop.

Triangulation dynamics. For each mesh half-edge, we store the active and passive intrinsic tensions T_a, T_p. We collect the active and passive tensions from all

half-edges belonging to a triangular face and carry out an explicit Euler step with step size $\sim 10^{-3}$ according to the following dynamics:

$$\partial_t T = \partial T_a + \partial T_p = \Pi_A[\tau_T^{-1} T_a^n - \tau_T^{-1} k_{\text{cutoff}} T_a^{n+1} - \tau_p^{-1} T_p], \tag{49}$$

$$\partial_t T_p = -k\tau_p^{-1} T_p \tag{50}$$

The symbol Π_A in the active tension equation means projecting the tension dynamics to conserve the total triangle area A. This constraint ensures numerical stability and prevents isotropic growth of the triangulation. It can be thought of as restricting the local "pool" of myosin motors available to each edge. Different "pool" mechanisms (fixing the triangle perimeter or circumcircle) are also possible, but have a tendency to lead to pathological triangulations. The cutoff parameter k_{cutoff} stops runaway positive feedback at values $T > k_{\text{cutoff}}$. It is not strictly necessary since runaway feedback is cut short by intercalations, but helpful for long-time simulations, were rarely, run-away tension cable configurations can occur which can blow up numerically. We chose $k_{\text{cutoff}} \sim \bar{T}/5$ where $\bar{T}$ is the overall tension scale, so that it has almost no effect in normal tension configurations. We chose the feedback parameter $n = 4$ and the relaxation rate $\tau_p = 2\tau_T$, the same used in the single-quartet and mean-field (single-triangle) simulations.

So far, the time evolution of tensions is purely autonomous (i.e. each tension triangle is independent from all others) and completely analogous to the single-quartet simulation. In the single-quartet simulation, all tension triangles are equal by symmetry and periodicity, and thus tile the plane as a triangulation by construction. In the absence of periodicity (where all tension triangles are identical), this is no longer guaranteed. Even if one starts with a tension triangulation, the autonomous time evolution Eq. (50) will result in a set of tension triangles that cannot fit together to a flat triangulation. More precisely, the triangulation will develop curvature [37], i.e. "crumple" out of plane. This means that we have to add an additional projector enforcing triangulation planarity to the tension dynamics Eq. (50):

$$\partial_t T_{ij} = \Pi_{\{T_{ij}\}_{ij}\ \text{planar}}[\tau_T^{-1} T_{a,ij}^n - k_{\text{cutoff}} \tau_T^{-1} T_{a,ij}^{n+1} - \tau_p^{-1} T_{p,ij}] \tag{51}$$

The constraints enforcing planarity (one constraint per triangulation vertex) can be worked out explicitly [13].

In practice, we enforce this projection as follows. The set of all balanced tension triangulations is parameterized by the dual vertex positions $\mathbf{t}_i$. We therefore seek the balanced tension configuration that approximates the intrinsic tensions as closely as possible by minimizing the following elastic energy:

$$E_{\text{tri}} = \frac{1}{2N_{\text{edges}}} \sum_{ij} (||\mathbf{t}_i - \mathbf{t}_j|| - T_{ij})^2 + \text{Pen}(A, A_0) \tag{52}$$

The intrinsic tension T_{ij} is the sum of the active and passive tensions. Since the simulation is based on half-edges, the per-edge intrinsic tension T_{ij} is the average of the tensions of the two half-edges (which can be though of as the two cellular cortices coupled in a cell-cell interface).

The second term, $\text{Pen}(A, A_0)$ is a penalty term on the triangle areas A (calculated from the vertex positions $\mathbf{t}_i$). It fixed the overall tension scale (whch is arbitrary due to force balance). It contains two terms:

$$\text{Pen}(A, A_0) = \gamma_{\text{tri}} \left(100 \cdot (\max\{0, \frac{A_0}{4} - A\})^2 + \frac{1}{2}(A - A_0)^2 \right) \tag{53}$$

Here, A_0 is an arbitrary reference area fixing the overall tension scale. Because the triangular mesh is oriented, the area A is signed, with negative signs corresponding to un-physical "flipped" configurations. These, and degenerate triangles, are penalized by the first term. The second term is a soft potential fixing the overall tension scale and preventing isotropic growth. The penalty strength γ was chosen at 10^{-3}, so that the area penalty represents a small correction to the length-term.

In the simulation, we first carry out an explicit Euler step for the intrinsic tensions, then "flatten the triangulation", i.e. find the dual vertex positions by minimizing Eq. (52), and finally set the intrinsic active tensions to the value implied by the dual vertex positions, i.e. $T_{a,ij} \to ||\mathbf{t}_i - \mathbf{t}_j|| - T_{p,ij}$.

The triangulation-flattening prescription can be thought of as modelling, indirectly, known feedback loops which lead to a convergence to balanced tension, most importantly, strain-rate feedback [13], which has been demonstrated experimentally [28]. The direct modelling of this effect requires going beyond the separation between tension- and real-space-dynamics that is the basis of our model here and is therefore beyond the scope of this paper. Further, the triangulation-flattening prescription is the most parsimonious generalization of the local tension feedback dynamics employed in the single-quartet simulation to a disordered tissue patch.

Cell shape dynamics. Above, we have described the dynamics of the tension triangulation. As in the single-quartet simulation, we calculate the real space cell tessellation (i.e. the positions of the cell vertices) by minimizing the cell-shape elastic energy while constraining the angles by the tension triangulation. In the case of a single quartet of identical cells, we could explicitly parameterize the cell shape by interface lengths and angles, and optimize only with respect to the former. In the disordered case, it is more convenient to enforce the angle constraint via a (strong) energy penalty. It would also possible to instead directly optimize the per-cell isogonal potentials Θ_i with respect to the Voronoi reference, obviating the need for a penalty.

The elastic energy to minimize therefore has two terms – the cell elastic energy Eq. (44) calculated from cell shape tensor $g_{\mathcal{C}}$ Eq. (43) and reference shape g_0, and the angle penalty, which corresponds to the cortical tension energy term:

$$E = \frac{1}{2N_{\text{edges}}} \sum_{ij} T_{ij}(1 - \hat{n}_{ij} \cdot \hat{\mathbf{r}}_{ij}) + \frac{\epsilon}{N_{\text{cells}}} \sum_i E_{\mathcal{C},i} \tag{54}$$

If desired, one can replace or modify the cell shape elastic energy $E_{\mathcal{C}}$ in Eq. (54) by another energy, e.g. the common area-perimeter elasticity. $1/\epsilon$ is the penalization parameter (we use $\epsilon^{-1} \sim 10^3\lambda$). The angle penalty enforces that the angle between the dual tension edge and the real-space edge is 90° by using the unit normal $\hat{n}_{ij}$ of the tension edge, and the unit normal vector $\hat{\mathbf{r}}_{ij}$ of the primal edge.

To understand the particular form $\hat{n}_{ij} \cdot \hat{\mathbf{r}}_{ij}$, recall that every triangulation edge $\mathbf{t}_i, \mathbf{t}_j$ is represented twice, as two oriented half-edges belonging to the two faces which meet at the edge. Using this orientation, for a half-edge edge $i \to j$, we can compute the dual outward facing unit normal $\hat{n}_{ij}$. We then compare $\hat{n}_{ij}$ to the primal edge unit vector $\hat{\mathbf{r}}_{ij} = \hat{\mathbf{r}}_{(ij)(ji)}$ from the primal vertex of the triangle (ij) belonging to $i \to j$ to that of the apposing triangle (ji). The angle penalty ensures firstly, that the primal edges are orthogonal to the correspondingly dual edge, implementing the tension constraint on angles. Secondly, it automatically penalizes "invalid" vertex positions, e.g. "bowties" in which a primal vertex of one cell lies within the neighboring cell. Such situations correspond to $\hat{\mathbf{r}}_{(ij)(ji)}$ anti-parallel to $\hat{n}_{ij}$, which is why we chose a slightly elaborate form for the angle penalty. Note also that the first term in Eq. (54) is slightly different from the standard cortical tension energy $\sum_{ij} T_{ij} r_{ij}$. However, the two have the same force balance minima. However, in the standard form, energy can be lowered by collapsing all interfaces to length 0, and so the numerical minimization becomes ill-defined without an additional area regularization. This issue could also be avoided by using periodic boundary conditions.

After carrying out a local Euler step and updating the dual vertex positions by "triangulation flattening", we find the primal vertex positions by minimizing the elastic energy Eq. (54).

Topological modifications. After each time-step we check whether any edge has collapsed, as in the single-quartet simulation. We call an edge collapsed if its

length is $< 5\%$ of the overall length scale (mean edge length at simulation start). If an intercalation occurs, we carry out an intercalation and set the active and passive tensions on the new edge as described for the single-quartet simulation. After each individual intercalation, the vertex positions are recalculated by energy minimization.

Automatic differentiation and numerical optimization. The simulation requires solving two optimization problems, one for the triangulation Eq. (52) and one for the real-space shape Eq. (54). To solve an optimization problem efficiently, it is crucial to know the gradient of the objective function. We use the python library `JAX` [101] to automatically differentiate our energy functions, allowing easy, rapid and bug-free calculation of the Jacobians. We further use `JAX`'s just-in-time functionality to accelerate our python code. Gradient-based optimization requires the objective function to be at least once differentiable. To ensure this, we mollify functions as required; for example, the Euclidean norm $\sqrt{x^2+y^2} \to \sqrt{x^2+y^2+\epsilon^2}$, $\epsilon \sim 10^{-3}$ to ensure differentiability when computing the lengths of very short edges.

With these tools, the energies can be efficiently minimized using `scipy`'s conjugate-gradient optimizer. With a relative tolerance of 10^{-5}, a shape optimization step for ~ 1000 cells takes ~ 15s on a laptop. Using the half-edge data structure described above, and `JAX`-based automatic differentiation, we can also easily construct the isogonal Hessian $\mathcal{H}_{ij}$ analyzed in Fig. S15

Simulation geometry and parameters. Finally, we need to specify the simulation geometry: the initial conditions, the boundary conditions, and the division of the tissue into active and passive patches.

Note that because the cell vertex positions are computed from the tension triangulation, in our initial condition we specify only the tension triangulation. As initial conditions, we chose rectangular patches of a regular triangular lattice, with Gaussian noise of $\sigma \sim 15\%$ added to the vertex positions. A triangular lattice corresponds to a hexagonal lattice of cells. Indeed, locally, the Drosophila embryo at the onset of GBE looks like it is composed out of (noisy) hexagonal lattice patches: Indeed, previous work has found non-zero hexatic order in the cellularizing *Drosophila* embryo [62, 63]. This lattice is subjected to a small initial strain to create an a initial tension anisotropy, as seen in the data. We can choose two possible orientations of the lattice plane with respect to the data – one creating initially mainly tension cables, one mainly bridges. We find that which of these two initial conditions are chosen matters little for the amount of extension obtained, since positive tension feedback always creates a bridge-dominated pattern eventually. To underline this point, Fig. 6A-C uses "cable" initial conditions. In Fig. 6D, we show snapshots from a simulation with "bridge" initial condition in order to most closely resemble the experimental data shown in Fig. 1C, bottom.

To investigate the effect of disorder, we also create initial conditions using a Poisson hard disk process (implemented in `scipy.QuasiMonteCarlo`). This randomly places points (the eventual vertices in tension space) under the constraint that no two points are closer than $2r$ where r is the "hard disk" radius. We sample from the disk process at a packing fraction of $\sim 55\%$, corresponding to tightly packed vertices. To create a tension triangulation, we then compute the Delaunay triangulation of this point set (we further refine the initial condition by removing the edge of this tension triangulation, where the Delaunay algorithm can create very long tension edges). This triangulation is stretched uniformly by the same amount as in the single-quartet case to set up the initial anisotropy of tension. Cell numbers and initial aspect ratios were also chosen identically. Using a hard disk process instead of a Poisson process results in more regularly spaced tension vertices (hyperuniform distribution) and avoids unbiologically large or small cells.

We use appropriate boundary conditions to mimic the geometry of the *Drosophila* lateral ectoderm. We consider a initially rectangular tissue patch with height $>$ width. The top/bottom edges correspond to the dorsal pole, the middle to the

ventral region, and the left/right sides to the anterior/posterior edges of the lateral ectoderm. To simulate the cylindrical geometry of the *Drosophila* trunk, the top/bottom boundary are given slip-wall boundary conditions, i.e. the cells on the boundary are pinned along the y-axis and free to move along the x-axis. The left/right boundaries are free. Boundary conditions are numerically implemented by a confining potential which penalizes deviation of the x or y coordinate of the cell centroids designated to be boundary cells from the location of the slip wall. This allows for flexible implementation of various boundaries and geometries.

We can also chose different boundary conditions. To investigate the self-limitation of GBE, we use all-free boundary conditions to eliminate the effects of the passive dorsal tissue and focus on effects intrinsic to the lateral ectoderm. We can also add slip walls on the left/right boundaries to model the experiments carried out in Ref. [29], where GBE was blocked by cauterization of the ventral tissue close to the posterior pole.

Next, we designate active and passive regions in the tissue. In the active region, tensions evolve in time according to excitable tension feedback Eq. (50). In the passive regions, there is no feedback, and tensions simply relax to their isotropic equilibrium value: $\dot{T} = -\tau_p^{-1}(T - \bar{T})$, where $\bar{T}$ is the arbitrary reference tension scale. Further, to model the large deformations that passive amnioserosa cells undergo, their reference cell shape relaxes visco-elastically: $\dot{S}_0 = -\tau_S^{-1}(S_0 - S_\mathcal{C})$. Finally, and most importantly, the passive tissue is softer – we take its elasticity constants to be 80% lower than in the active region.

As in the single-quartet simulations, we can take into account the fact that the cells in the germ band are initially stretched isogonally by VF invagination. This can be encoded by stretching the tissue using the slip wall boundary conditions; instead, we set the cell reference shape S_0 to an anisotropic matrix. We chose an anisotropy of 15% for the main "wild type" simulations in Fig. 6A-D; the remaining simulations were carried out with 0 isogonal mode for simplicity. For example, non-zero isogonal stretching would affect the cell shape index 6F in addition to the increasing disorder. Therefore, the simulations in Fig. 6E-F were carried out with 0 isogonal mode. However, as pointed out in Fig. 5F, the isogonal mode has an influence on the observed LTC order (i.e. prevalence of tension bridges) by moving the T1 boundary: non-zero isogonal stretching moves this boundary "back" and thereby increases the fraction of bridges in the tissue. The supplementary movie, based on the "pure active" simulation from Table 2, therefore shows a lower fraction of bridges, corresponding to the pattern we would expect in a *twist/snail* embryo.

To simulate a wild type embryo, we chose the size of the passive patch to be approximately 40% of the embryo circumference (the exact value does not have an important influence). To mimic an embryo without modulation of activity along the DV axis (e.g. a *TollRM9* mutant), all cells along the embryo were taken to be active. The cells at the very tissue boundary are always passive for reasons of numerical stability. Otherwise edges on the boundary could undergo a T1, which leads to an invalid state.

As a summary, Table 1 lists the bio-physical and numerical parameters used in the simulations, and Table 2 gives a list of all the simulations displayed in this work.

Biophysical parameters		
Feedback exponent	n	4
Passive tension relaxation	τ_p	$2\tau_T$
Cutoff	k_{cutoff}	$\overline{T}/4$
Initial anisotropy		10%
Noise in initial tensions (standard deviation)		$0.15\,\overline{T}$
Elasticity coefficient ratio	μ/λ	1/4
Passive region softening	$\lambda_{\text{pass}}/\lambda_{\text{act}}$	0.2
Numerical parameters		
Triangulation area penalty	γ_{tri}	0.01
Angle constraint penalty	$1/\epsilon$	$1,000$
Time step	dt	$0.005\,\tau_T$
Edge length to trigger collapse		$0.075\,\ell_{\text{initial}}$

Table 1: Default parameters of tissue scale simulation. These parameters were used in all simulations except otherwise indicated. $\overline{T}$ is the overall tension scale (average edge tension at initial condition).

Name	Figure	Comments
WT 1	6A–C, 6H	Standard geometry: Simulation with active and passive regions and cylindrical boundary conditions, and a perturbed triangular lattice as initial tension triangulation
WT 2	6D	Same as WT 1, but with opposite orientation of hexagonal lattice
Pure active	6E–F	Pure active tissue patch with free boundaries
Varying noise	S14C	Pure active tissue patch with free boundaries, and varying levels of Gaussian noise in the initial tensions
No passive region	6G–K	Cylindrical boundary conditions and no passive tissue region
Varying shear modulus	6H, S11	Standard geometry with varying shear modulus, including zero shear modulus ("floppy cells")
Cauterized	S12	Slip walls on all four sides of the tissue patch, blocking convergence and extension
Disordered	6E–F, S14A–B	Simulations with disordered initial triangulation, i.e. random Delaunay instead of triangular lattice, and free boundaries

Table 2: List of tissue scale simulations.

5 Movie captions

Movie 1: Side view and flat projection of one side of the embryo surface. Ventral furrow invagination (gray cells on the dorsal side) is followed by convergence–extension of the germ band (lateral ectoderm cells colored purple, blue and green). As the germ band elongates along the AP axis, the cells move over the posterior pole. The amnioserosa (orange and red cells) undergoes convergence–extension in the opposite direction of the germ band and exhibits significant cell shape elongation while cells in the germ band remain mostly isotropic in shape. Near the end of germ band extension (ca 35 min) cell divisions start. (Corresponds to Fig. 1A; invaginating cells are colored in gray; cells in the head are colored white; cells after division events are colored in light gray.)

Movie 2: Relative tension dynamics in the lateral ectoderm. Relative junctional tensions inferred from cell geometry reveals show the emergence of an alternating pattern of high and low tensions that organizes cell intercalations (T1 transitions). Coherent intercalations drive convergent extension tissue flow which slows down significantly as cell scale order is lost.

Movie 3: Simulation of single intercalating cell quartet. Simulation of an intercalating cell quartet driven by positive tension feedback and myosin handover mechanism, corresponding to Fig. 4E. Out of the ensemble from Fig. 4E, the movie and shows a simulation for symmetric initial tensions (i.e. equal initial tensions on the two non-collapsing interfaces $T_1 = T_2$). After the edge flip, the blue parts of the inner tension triangulation edge indicate the passive tension on the newly formed interface. The passive tension rapidly relaxes while the active tension grows due to positive tension feedback.

Movie 4: Simulation of convergent extension in embryo-like geometry. Simulation of tissue scale model of convergent extension, corresponding to Fig. 6A-C. The embryo is modeled by a rectangular tissue patch with slip walls on the top and bottom edge, mimicking the embryo's cylindrical geometry, and active and passive tissue regions, corresponding to the germ band and the amnioserosa, respectively. Left: Cell tessellation with black dots indicating the cells along the slip wall (restricted to move along horizontally along the "AP axis"). Right: underlying tension triangulation. Lightly shaded edges are passive (i.e. the positive tension feedback is deactivated). The tension triangulation is initialized with the experimentally observed initial tension anisotropy which breaks rotational symmetry and aligns the tissue extension along the "AP axis".

Movie 5: Simulation of convergent extension for ordered and disordered initial cell arrays. Simulation of tissue scale model of convergent extension with ordered (left) and disordered (right) initial conditions, corresponding to Fig. 6E-F. The simulations where carried out with free boundary conditions and without passive regions to focus on the effects intrinsic to active intercalations. For the ordered case, the initial tension triangulation was taken to be a triangular lattice with Gaussian noise added to the vertex positions. For the disordered case, the tension triangulation is the Delaunay triangulation of a set of tension vertex positions sampled randomly from a Poisson hard disk process (Fig. S14). The number of cells and the initial tension anisotropy, as well as all other parameters, are the same for both simulations. Top row shows the cell arrays, bottom row the underlying tension triangulation. If the initial cell array is disordered, both the tissue and the tension triangulation extend only very little.

Movie 6: Simulation of convergent extension without cell rigidity and without DV modulation of activity. Simulation of tissue scale model of con-

vergent extension in an embryo-like geometry and choice of parameters as in Fig. 6A-B (left, "Control"), in a geometry without DV modulation of activity and cell elasticity (center, "No passive region"), and in an embryo-like geometry but with vanishing cell shear modulus (right, "No cell rigidity"), corresponding to Fig. 6G-J. All other parameters are identical across the three simulations. Top row shows the cell array, bottom row the underlying tension triangulation. Lightly shaded edges are passive (no positive tension feedback). The simulation without a passive region (center) stops early because it becomes numerically unstable as cell shapes become increasingly degenerate. In all three conditions, active T1s drive elongation of the tension triangulation, while the convergent extension of the cell array only occurs for the "control" condition.